Theoretical developments in low-dimensional magnetic systems

Zhao, Zhen

2024

Document Version:
Publisher's PDF, also known as Version of record

Theoretical developments in low-dimensional magnetic systems

ZHEN ZHAO
DEPARTMENT OF PHYSICS | FACULTY OF SCIENCE | LUND UNIVERSITY

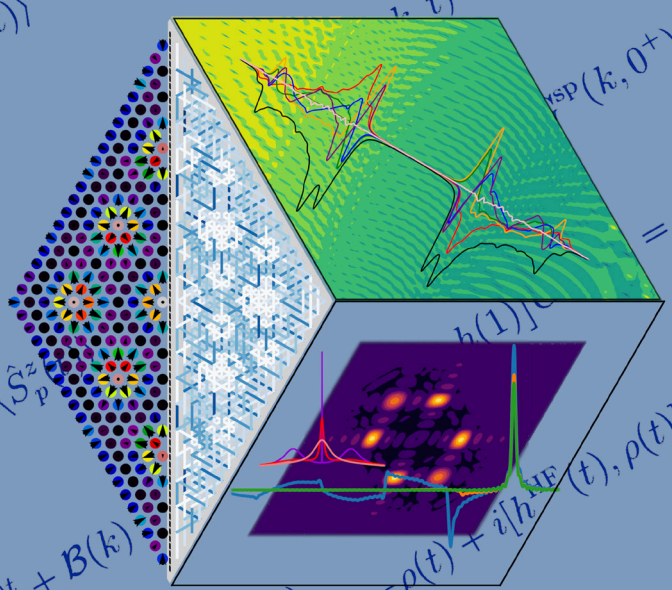

Theoretical developments in low-dimensional magnetic systems

Theoretical developments in low-dimensional magnetic systems

by Zhen Zhao

LUND
UNIVERSITY

Thesis for the degree of Doctor of Philosophy
Thesis advisors: Prof. Ferdi Aryasetiawan, Dr. Claudio Verdozzi
Faculty opponent: Prof. Dr. Stefan Blügel

To be presented, with the permission of the Faculty of Science of Lund University, for public criticism in the Rydberg lecture hall (Rydbergsalen) at the Department of Physics on Friday, the 20th of September 2024 at 9:00.

Organization	Document name
LUND UNIVERSITY Department of Physics Box 118 SE–221 00 LUND Sweden	**DOCTORAL DISSERTATION** Date of disputation 2024-09-20 Sponsoring organization
Author(s) Zhen Zhao	

Title and subtitle

Theoretical developments in low-dimensional magnetic systems

Abstract

In this thesis, we investigate low-dimensional magnetic systems from the theoretical points of view. To address situations with several and distinct magnetic interactions, we develop different frameworks, including a magnon self-energy approach, a spin dynamical exchange-correlation (xc) field formalism and a scheme combining Matrix Product States method and exact diagonalization/nonequilibrium Green's function methods (MPS + ED/NEGF). By means of effective models, we study topics including magnetic frustration, homogeneous spin chain, magnetic skyrmions, and magnetic impurities.

The thesis is based on four papers: In Paper I, we apply the magnon self-energy approach to study the ground-state properties of two-dimensional Heisenberg models with competing exchange couplings. In Papers II and IV, the dynamical xc field formalism is used to calculate the Green's function. In Paper II, we propose a spin xc field formalism to calculate dynamical spin structure factor of the one-dimensional antiferromagnetic Heisenberg model at zero-temperature. In Paper IV, we investigate the Kondo spectral function by extending the xc field formalism to finite temperatures, and apply the formalism to the single-impurity Anderson model. In Paper III, we propose a MPS + ED/NEGF scheme to calculate the ground-state and dynamical properties of quantum magnetic skyrmions with itinerant electrons explicitly included.

Key words

magnetism, Heisenberg model, magnetic skyrmion, magnetic impurity, exact diagonalization, dynamical exchange-correlation field, MPS, NEGF, Kondo spectral function

Classification system and/or index terms (if any)

Supplementary bibliographical information	Language
	English
ISSN and key title	ISBN
	978-91-8104-139-2 (print) 978-91-8104-140-8 (pdf)
Recipient's notes	Number of pages: 176 / Price
	Security classification

Theoretical developments in low-dimensional magnetic systems

by Zhen Zhao

LUND
UNIVERSITY

A doctoral thesis at a university in Sweden takes either the form of a single, cohesive research study (monograph) or a summary of research papers (compilation thesis), which the doctoral student has written alone or together with one or several other author(s).

In the latter case the thesis consists of two parts. An introductory text puts the research work into context and summarizes the main points of the papers. Then, the research publications themselves are reproduced, together with a description of the individual contributions of the authors. The research papers may either have been already published or are manuscripts at various stages (in press, submitted, or in draft).

Cover illustration front: Illustration of magnetic skyrmions, dynamical exchange-correlation fields and spectral functions (adapted from Papers II, III and IV).

Funding information: Financial support by the Swedish Research Council (VR).

Faculty of Science, Department of Physics

ISBN: 978-91-8104-139-2 (print)
ISBN: 978-91-8104-140-8 (pdf)

Printed in Sweden by Media-Tryck, Lund University, Lund 2024

Dedicated to my parents

Contents

List of publications

This thesis is based on the following publications, referred to by their Roman numerals:

I **A Green's function method for the two-dimensional frustrated spin-1/2 Heisenberg magnetic lattice**
Z. Zhao, C. Verdozzi, F. Aryasetiawan
Phys. Rev. B **106**, 184417 (2022)

We derive the magnon Hedin equations via the Schwinger functional derivative technique. We use a self-consistent Green's function method to calculate ground state spin patterns and magnetic structure factors for two-dimensional magnetic systems with frustrated spin-1/2 Heisenberg exchange coupling. We compare our magnon self-energy method with exact benchmarks in homogeneous and inhomogeneous finite systems. We find that our method performs well for scalar-product interactions. In comparison, for cross-product interactions, the accuracy is not equally good, which may suggest an inclusion of higher corrections.
Contribution: I performed all calculations, produced all figures and wrote the first draft of the article. I also contributed to the final writing.

II **Dynamical exchange-correlation potential formalism for spin-1/2 Heisenberg and Hubbard chains: the antiferromagnetic/half-filled case**
Z. Zhao, C. Verdozzi, F. Aryasetiawan
Phys. Rev. B **108**, 235132 (2023)

We present a novel exchange-correlation potential (Vxc) formalism, tailored for spin Hamiltonians. We derive the sum rule and the exact constraint for the spin exchange-correlation hole. We apply the formalism to a spin-1/2 chain with Heisenberg interactions. The Vxc in the thermodynamic limit is extrapolated from exact diagonalization results of small clusters. For a purely antiferromagnetic (AFM) interaction, comparisons with numerical benchmarks show that our approach yields a one-particle spectral function with favourable accuracy at a relatively low computational cost. We also calculate the spectral function of a one-dimensional Hubbard lattice, to illustrate that Vxc results from Hubbard and AFM Heisenberg models converge to each other at large interaction.
Contribution: I derived the sum rule for the local spin system, performed all calculations, produced all figures and wrote the first draft of the article. I also contributed to the final writing.

III **Quantum skyrmions on a Kondo lattice**

Z. Zhao, E. Östberg, F. Aryasetiawan, and C. Verdozzi
Draft

We present a quantum treatment for magnetic skyrmions in two-dimensional itinerant magnets. The Kondo exchange between local quantum spin-1/2:s and non-interacting itinerant electrons is approximated in the mean-field level, which decouples the spin and electron degrees of freedom. Correspondingly, a Tensor Network method is implemented for the spins, exact diagonalization for the isolated electrons, and a nonequilibrium Green's function method for open electron system contacted to electric leads. We show that the itinerant electrons are essential to the ground state profiles, as well as the dynamical properties of the quantum spin textures.
Contribution: I performed calculations and produced figures for the closed and the extended electron-spin system. I combined the open system codes from E. Ö with my codes. I wrote the the introduction section, a large part of the method and the result sections and the conclusion section of the first draft.

IV **Kondo spectral functions at low-temperatures: A dynamical-exchange-correlation-field perspective**
Z. Zhao
Draft

We study the Kondo peak of the spectral functions in an Anderson impurity model, using the dynamical exchange-correlation potential (Vxc) formalism for Green's functions. We calculate an exact Vxc on a nanosize cluster, and extrapolate to system with large size.
Contribution: After initial discussion with FA and CV, I decided all conceptual aspects to consider in the project and the topics to treat. I performed calculations, analyzed the effective Vxc from hybridization and interaction, and wrote the article, with suggestions for revision from FA and CV.

List of acronyms

xc	exchange-correlation
DFT	Density functional theory
HF	Hartree-Fock
LDA	Local-density approximation
LSDA	Local-spin-density approximation
TDDFT	Time-dependent density functional theory
NEGF	Nonequilibrium Green's function
QP	Quasiparticle
FM	Ferromagnetic
AFM	Antiferromagnetic
ED	Exact diagonalization
TN	Tensor Network
MPS	Matrix product state
MPO	Matrix product operator
DMRG	Density matrix renormalization group
TEBD	Time-evolving block decimation
RPA	Random phase approximation
KBE	Kadanoff-Baym equation
GKBA	Generalized Kadanoff-Baym ansatz
WBL	Wide-band limit
LDOS	Local density of states
DMI	Dzyaloshinskii-Moriya interaction
DMFT	Dynamical mean-field theory
SIAM	Single-impurity Anderson model
NRG	Numerical renormalization group

Acknowledgements

I would like to express my deepest gratitude to my supervisors, Claudio Verdozzi and Ferdi Aryasetiawan. Although you are quite different in many ways, you both have great enthusiasm for science and an astonishing wealth of knowledge. I have greatly benefited from your guidance, both academically and personally. You taught me so many things about physics and how to conduct research. And I enjoyed a lot from your jokes and stories. During the covid time, your support was especially invaluable.

I want to thank my co-supervisor Pascale Deen for the inspirations from the experimental side. Thanks to Erik van Loon for the good experience as a teaching assistant in your course, for organizing the magnetism conference in Lund, and for other discussions. My thanks extend to Krister Karlsson for discussions. A special thanks to Andrea Idini for the journal club and your extra assistance with IT issues.

I would also like to thank the members in our groups, Emil Viñas Boström, Fredrik Nilsson, Tor Sjöstrand, Megha Gopalakrishna, Ayan Pal and Emil Östberg, for the discussions we had and the fun time during the schools or conferences we attended together.

The division of mathematical physics has been an excellent place to work at. Thanks to everyone for creating such great atmosphere. A special thanks to Peter Samuelsson, Katarina Lindqvist and Therese Stridh for the help in so many practical issues. Thanks to my office mates: Gunnar Eriksson, Asimina Papoulia, Saulo Moreira, Felipe Zapata, Edvin Olofsson, Rezvan Tahouri, Nicola d'Alessandro and Carles Roch i Carceller. I would also like to thank Andreas Wacker and Gillis Carlsson for the help during my teaching duties. My thanks extend to Tomas Brage, Marcus Dahlström, Stephanie Reimann, Armin Tavakoli, Patrick Potts, Gunnar Ohlén, Ingemar Ragnarsson and Sven Åberg for the chats during lunch/goose dinner time, and for the knowledge in courses and seminars.

I would like to thank Cecilia Jarlskog for your stories about science and scientists. I enjoyed every moment when I talked to you in the kitchen or during the weekends.

Thanks to Lila for naming my cat roommates. Thanks to Philipp for helping me build their toy. Thanks to Yijie and Yingjie for bringing them foods. Thanks to Alex, Martin, Mattias, Björn, Jennifer, Akshat, Ekin, Sara, Morten, Gabriele, Shishir, Stefanos, Drilon, Pharnam, Jimmy, Axel, Kalle and Koushik for the

fun time in and outside our division. My thanks extend to Yupan, Miaoxin, Hongliang, Zheshen, Mengli, Wenzhe, Qianqian and Yanfang for the fun and good memories. A special thanks to Hanjing and Qian for sharing interesting moments in your life.

Last but not least, I would like to thank my parents. Thank you for always supporting me.

Popular summary in English

Magnetism is a ubiquitous phenomenon in everyday existence. The study of magnetism has spanned thousands of years. As a branch of natural science, it has developed with discoveries of new phenomena, empirical or theoretical descriptions, and applications. Early recognition of magnetism included the observation that magnets could attract ferrous metals from a distance, and interact with each other either attractively or repulsively. In later centuries, people realized that Earth itself is a huge magnet, and that artificial magnets could be created. This primitive knowledge led to the invention of compass, a great progress in navigation. Around the 1800s, a significant step in the fundamental description of magnetism occurred when it was discovered that magnetism and electricity are connected. These connections were demonstrated by phenomena such as electromagnetic induction and the Faraday effect, and were summarized by Maxwell's equations, a cornerstone of modern classical electromagnetism. A revolutionary application of classical electromagnetism is the electric generator. In the early 1900s, with the development of quantum mechanics, the investigation on magnetism continued at a more fundamental and microscopic level. The concept of spin was proposed to explain the magnetic moment of electrons. Along with progress in theories for solids, magnetic orders were understood on a quantum mechanical basis. Improved understanding of magnetism led to various applications, including radio-wave-based communications, magnetic storage, magnetic resonance imaging and advanced probing techniques of magnetic properties. In turn, novel phenomena were observed, including quantum spin liquids, where ordinary magnetic order is absent, and magnetic skyrmions, where the noncollinear spin alignments are related to topological properties. As a fact, not all of these new discoveries are fully understood theoretically.

In this thesis, we focus on aspects related to our theoretical understanding of magnetism. A natural difficulty encountered in theoretical treatments is that magnetic materials consist of an enormous number of atoms and electrons. First-principles calculations partially solve this problem and succeed in many materials. However, there remains systems where current treatments perform less satisfactorily. Therefore, we work with effective models in one- and two-dimensions, which have lower complexity than real materials, but still capture the essential physics, and even exhibit unique properties of surface/interface systems. Using these models, we propose theoretical frameworks and calculate some quantities which can be compared with experiments. Our long-term goal is to utilize the model results to develop new methods for systems which are beyond the scope of current treatments.

Theoretical developments in low-dimensional magnetic systems

Chapter 1

Introduction

The study of magnetism can be traced back to ancient history, and has continued into contemporary times [1]. Despite the extensive history of research in this field, magnetism still maintains an air of mystery. Moreover, the field of low-dimensional (low-D) magnetism has attracted significant research interest for several reasons: i) Several models of low-D magnetism, in contrast to their 3D counterparts, are exactly solvable. These models provide theoretical insights into phase transitions and the interplay of quantum and thermal fluctuations. ii) There are real materials relevant to low-D models. Magnetic materials that display similar properties in their bulk form may exhibit distinct magnetic behaviors when approaching the monolayer limit [2, 3]. This indicates that low-D magnetism is not merely a theoretical playground but a compelling subject in its own right. iii) High-temperature superconductors with coherence lengths smaller than the interplanar distance have been discovered. The superconductivity in these materials is related to the strong magnetic fluctuations which exist in low-D systems [4, 5]. Consequently, low-D magnetism offers connections to other profound fields of science and cutting-edge technologies.

In this thesis, we will discuss our theoretical studies concerning magnetic systems in low dimensions. An important theorem from the 1960s about low-D magnetism, the Mermin-Wagner theorem [6], states that no one-dimensional or two-dimensional (1D/2D) isotropic Heisenberg spin system can exhibit magnetic order at any non-zero temperature. However, magnetic anisotropy and other mechanisms beyond the isotropic Heisenberg model can lift this restriction. According to the Bohr–van Leeuwen theorem, magnetism is a purely quantum mechanical effect [7]. Therefore, we focus on studying the quantum fluctuations in low-D magnetic systems. In the investigation of magnetism in solid materials,

one approach involves solving the many-body Schrödinger equation

$$i\frac{\partial}{\partial t}|\Psi(t)\rangle = \hat{H}|\Psi(t)\rangle, \tag{1.1}$$

where $|\Psi(t)\rangle$ is the many-body wavefunction and atomic units (a.u.) are used such that $m_e = e = \hbar = 4\pi\epsilon_0 = 1$. We will use atomic units through this thesis. The SI values of other observables can be derived, e.g., length $x = 1$ a.u. $= \hbar^2(4\pi\epsilon_0)/(m_e e^2) = 5.292 \times 10^{-11}$ m and time $t = 1$ a.u. $= (4\pi\epsilon_0)^2\hbar^3/(m_e e^4) = 2.419 \times 10^{-17}$ s. The Hamiltonian contains in principle both ionic and electronic degrees of freedom. However, in this thesis we focus on the electron properties. Therefore, we apply the Born-Oppenheimer approximation such that the following simplified Hamiltonian can be used:

$$\hat{H} = -\frac{1}{2}\sum_i \nabla_i^2 + \frac{1}{2}\sum_{i\neq j}\frac{1}{|\mathbf{r}_i - \mathbf{r}_j|} + \sum_i V^{\text{ext}}(r_i) \tag{1.2}$$

where $r_i = (\sigma_i, \mathbf{r}_i)$ are the spin-position variables of the electrons, and V^{ext} is the external potential experienced by each electron. The other two terms contained in $\hat{H}$ represent the electron kinetic energy and the Coulomb interaction, respectively.

Solving the Schrödinger equation to obtain the wavefunctions $\Psi(r_1, r_2, \cdots, r_N)$, which depend on the positions and spins of all N electrons, is generally a very difficult task due to the large number of the electrons, their fermionic nature, and the Coulomb interaction. The challenge is particularly pronounced for magnetic materials, especially where the electrons of $3d$ transition metals or $4f$ rare-earth elements are highly correlated or where time-dependent electromagnetic fields drive the system out of equilibrium. For low-D magnetic systems, the usual perturbative approaches work in only limited cases. Extensive theoretical methods have been developed in order to overcome these difficulties. Some of them map the real system onto models with lower complexity that still capture the physical essence, while others are based on first-principles. In this thesis, we follow the former path and discuss several model-based developments, some of which are motivated by the goal of improving first-principles calculations of real materials. Our research primarily investigates low-D systems at zero temperature, utilizing both isotropic and anisotropic models. Although we do not perform first-principles calculations with real materials, we anticipate that our work will provide insights into the physics of low-D magnetism and contribute to the improvement of the current theoretical framework. In the sections below, we will first give a brief review of density functional theory, a standard tool for first-principles calculations in condensed matter physics and chemistry [8, 9]. Here, our purpose is to review some fundamental ideas which are connected to

our model-based approaches. Then we will discuss the Green's function, a basic building block in many-body theory [10], and its relation to several experimental techniques which measure magnetic properties. Also, we will introduce the concepts of quasiparticles and magnetic impurities, which are of high relevance to the papers on which this thesis is based.

1 Density functional theory

Hohenberg and Kohn [11] derived theorems which state that the ground state total density of electrons

$$\rho(\mathbf{r}) = N \int dr_2 \cdots dr_N |\Psi(r, r_2, \cdots, r_N)|^2 \tag{1.3}$$

determines the external potential $V^{\text{ext}}(\mathbf{r})$ up to a constant. Such one-to-one relationship between $V^{\text{ext}}(\mathbf{r})$ and $\rho(\mathbf{r})$ means that given $\rho(\mathbf{r})$, one can in principle determine all the ground state magnetic properties and even excited state ones. Using the electron density instead of the full wavefunction as the central quantity reduces the difficulty in calculating solid state properties. Furthermore, by building an auxiliary noninteracting system which produces the exact real system electron density [12], one can map the many-body problem to a set of single-particle equations, namely the Kohn-Sham equation

$$\Big[-\frac{1}{2}\nabla^2_{\mathbf{r}} + V^{\text{ext}}(\mathbf{r}) + V^{\text{H}}(\mathbf{r}) + V^{\text{xc}}(\mathbf{r}) \Big] \psi_i(\mathbf{r}) = \varepsilon_i \psi_i(\mathbf{r}) \tag{1.4}$$

where $\psi_i(\mathbf{r})$ produces the same electron density as that of the original system. The exchange-correlation (xc) potential V^{xc} in the Kohn-Sham scheme is the functional derivative of the xc energy E^{xc} with respective to the electron density

$$V^{\text{xc}}(\mathbf{r}) = \frac{\delta E^{\text{xc}}[\rho]}{\delta \rho(\mathbf{r})}. \tag{1.5}$$

E^{xc} can be formally expressed in terms of the xc hole ρ^{xc}:

$$\begin{aligned} E^{\text{xc}}[\rho] &= \frac{1}{2} \int dr dr' \rho(r) v(r - r') \rho^{\text{xc}}(r, r') \\ &= \frac{1}{2} \int dr \rho(r) \int_0^\infty dR R \bar{\rho}^{\text{xc}}(r, R) \end{aligned} \tag{1.6}$$

where $\bar{\rho}^{\text{xc}}(r, R) = \int d\Omega_R \rho^{\text{xc}}_\sigma(\mathbf{r}, \mathbf{r} + \mathbf{R})$ is the spherical average of ρ^{xc}. Note that $r = (\sigma, \mathbf{r})$ is the spin-position variable but $R = |\mathbf{R}|$. The definition of

ρ^{xc} involves density operators, which can be found in e.g. Ref. [13]. Here, we focus on the physical picture. ρ^{xc} can be interpreted as a depletion of electron distribution around a given electron at $\mathbf{r}$ due to the Pauli principle. This electron depletion fulfills a sum rule in that it integrates to -1 (hence a hole). In practice, the Kohn-Sham V^{xc} is unknown but can be approximated by the local-density approximation (LDA), where the xc energy is calculated from the homogeneous electron gas. Despite its simplicity, the LDA yields rather accurate results for many materials when used to calculate the electronic structure [14]. This success can be attributed to several factors: i) LDA fulfills the sum rule of the xc hole; ii) LDA yields a good approximation of the spherical average of ρ^{xc}, which is the relevant quantity, as shown in Eq. (1.6).

The LDA is generalized to spin-polarized systems as the local-spin-density approximation (LSDA) [15, 13]. Furthermore, DFT has been extended to study dynamical properties through time-dependent density functional theory (TDDFT) [16, 17, 18, 19]. The foundation of TDDFT is the Runge-Gross theorem [20], which proves a one-to-one correspondence between the time-dependent external potential $V^{\mathrm{ext}}(r,t)$ and the time-dependent electronic density $\rho(r,t)$ for many-body systems evolving from an initial state. As in ground-state DFT, a time-dependent Kohn-Sham scheme can be constructed for TDDFT, where the time-dependent xc potential needs to be approximated.

Here, we focus on ground-state DFT. Despite its success in very many situations, L(S)DA does not perform well in strongly correlated systems. One approach to improving the performance of DFT on model lattice systems is through the xc term. Recently, a framework has been proposed, based on a dynamical xc field which is the Coulomb potential of its corresponding dynamical xc hole $\rho^{\mathrm{xc}}(t)$ [21]. The dynamical xc field, distinct from the time-dependent xc potential in TDDFT, couples to the Green's function locally in space and time. We will expand the detailed discussion of the formalism in magnetic systems with derivations in chapter 2 and some results in chapters 3 and 4.

2 Green's function and probing the magnetic structure

Apart from the electron density, the Green's function is another key quantity in many-body frameworks. The single-particle Green's function is an expectation value of field operators. The ground-state energy, the ground-state expectation values of single-particle operators, and the excitation spectrum of the system can be calculated given the single-particle Green's function. For system out of

equilibrium, the nonequilibrium Green's function (NEGF) framework is the tool of choice for quantum transport problems. We will introduce several theoretical approaches based on the Green's function in chapter 2. Here we discuss the relation between the Green's function and a widely used experimental techniques in probing the magnetic structure, namely magnetic neutron scattering.

The neutron, which carries zero charge and nonzero magnetic dipole moment, is an ideal probe for studying magnetic structures [22]. Spin-polarized neutron beams can penetrate into the material and interact with unpaired electrons of the atoms which form a lattice. Effectively, the magnetic scattering process is determined by the intrinsic magnetic properties of the material. Measuring the neutron scattering cross-section gives the dynamical magnetic structure factor $S(\mathbf{Q}, \omega)$, where $\mathbf{Q}$ is the momentum transfer and ω is the energy transfer. Essentially, $S(\mathbf{Q}, \omega)$ is related to the spin-polarized Green's function.

The Green's function also provides a theoretical basis for other experimental techniques, such as the spin-resolved angle-resolved photoemission spectroscopy [23]. The relationship between the Green's function and probing techniques provides part of the motivations of this thesis: by developing approaches that calculate the Green's function with better accuracy and that improve DFT, we aim at explaining experimental results (e.g. from the European Spallation Source [24] when its construction is completed).

3 Quasiparticles

For interacting many-body systems at low temperature, despite the enormous number of degrees of freedom, the physical properties are greatly determined by collective excitations [25], as if the many-body problem could be treated as a one-particle problem. Such excitations are called quasiparticles (QPs). We note that there exist conventions that restrict QPs to be fermionic and refer to the bosonic excitations as "collective excitations" [26]. However, in this thesis, we use QP for all those particle-like excitations.

The categories of QPs are very broad, from the widely-studied ones, such as the QP in solids which may be thought of a screened particle and phonons which are associated with lattice vibration, to new species such as composite fermions and magnetic solitons. Different kinds of QPs may interact with each other and thus create new QPs. Here we introduce the QPs that are related to this thesis.

3.1 Magnons

The local spins in a ferromagnetic (FM) material align parallel to each other (this direction is chosen as the z-axis) in the ground state. An elementary excitation will lead to a decrease in the total z-component spin S^z_{total} of the system, which is distributed collectively among all the spins, namely the spin waves. Magnons are the units of quantization of spin waves. A single magnon carries spin one, corresponding to the deviation of S^z_{total}. The energy cost of creating a single magnon is much lower than the cost of flipping a spin on a site. In absence of external field, thermal energy is sufficient to excite magnons. Magnons and their interaction with other QPs are of high importance in many magnetic phenomena [27, 28]. We will introduce a magnon self-energy-based approach in chapter 2.

3.2 Spinons

Spinons are the low-lying excitations in spin-$\frac{1}{2}$ antiferromagnetic (AFM) chain [29]. Spinons, each of them carrying spin-$\frac{1}{2}$, are excited in pairs and correspond to magnetic domain walls. We will study the two-spinon excitation spectrum of an AFM spin-$\frac{1}{2}$ chain with the xc field-based formalism, with the results presented in chapter 3.

3.3 Magnetic skyrmions

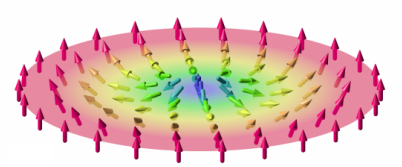

Figure 1.1: A sketch of a skyrmion, adapted from [30].

Magnetic skyrmions (referred to as skyrmions in the text below) are topologically protected spin textures, where the spin moments form non-collinear and vortex-like structure [31, 32, 33, 34, 35, 36] (see a sketch of a Neel type skyrmion in Fig. 1.1). Skyrmions can be found in 2D materials, and they are QPs with long life-time and can be manipulated by ultralow currents. Recently, considerable research interests have been devoted to quantum skyrmions [37, 38, 39] and itinerant-electron-skyrmion systems [40, 41, 42]. We will study quantum

skyrmions in contact to itinerant electrons by combining Tensor Networks and NEGF methods.

4 Magnetic impurities

The study of magnetic impurities can be traced back to the observation that the resistance of gold as a function of temperature (T) exhibited a minimum. This non-monotonic behavior of resistance was later explained by the Kondo model [43], where the conducting electrons are coupled to the localized spin on the impurity via an AFM spin-exchange interaction. During the scattering process of a conducting electron by the impurity, both the electrons and the impurity can undergo a spin flip. The scattering rate given by perturbation theory scales logarithmically with inverse temperature, and thus resistance can increase with decreasing T. However, the divergence of the scattering rate as T approaches zero suggests that the Kondo model requires a nonperturbative treatment [44, 45]. It is now known, from methods such as the numerical renormalization group [46], that the localized spin is screened by conducting electrons at temperatures below the so-called Kondo temperature [47]. A spin-singlet is formed which scatters electrons as a nonmagnetic impurity [48]. Consequently, the scattering process is changed and the scattering rate converges to a constant in the limit $T \to 0$.

Although the Kondo model has been extensively studied, quantum impurity models receive extended research interest due to their connections to quantum transport in nanoscale devices [49, 50, 51], many-body entanglement [52], and dynamical mean-field theory [53, 54, 55]. We will investigate magnetic impurities using models where localized spins are coupled to itinerant electrons via the Kondo exchange. In chapter 4, we present the results for i) a skyrmion-itinerant-electron system as mentioned in section 3.3, and ii) a calculation of the Anderson model [56] spectral function within a dynamical xc field scheme.

5 Plan of the thesis

The thesis is organized as follows: In chapter 2, we give an introduction to the theoretical methods used in the papers, including our new developments. The physical systems concerned in the papers, which involves only localized spins or spins + itinerant electrons, are discussed in chapter 3 and 4, respectively. In

chapter 5 we summarize the results and give an outlook of the possible future studies.

Chapter 2

Methods

We start this chapter with a brief review of the theoretical frameworks which are used in the papers. In 1.1 and 1.2, we discuss two wavefunction-based methods, namely exact diagonalization and Tensor Networks. In 1.3 and 1.4, we introduce Green's function methods in and out of equilibrium. The theoretical developments during this thesis work are delineated in the following sections. In section 2, we explain in detail the self-energy approach for magnon systems in equilibrium. In section 3, we present a novel exchange-correlation field formalism for a spin Hamiltonian. In section 4, we provide the key equation of the exchange-correlation field formalism applied to the single-impurity Anderson model. We hope this chapter serves as a general description of our developments, and provides the theoretical background for the numerical results in chapters 3 and 4.

1 Review

1.1 Exact diagonalization

For a many-body problem, we expand the Hamiltonian in the basis written in the occupation number representation. Considering a N-electron system described by L single-particle orbitals, a basis vector takes the form

$$|n_{1\uparrow}, n_{1\downarrow}, \cdots, n_{L\uparrow}, n_{L\downarrow}\rangle \tag{2.1}$$

where $n_{i\sigma}$ can be one or zero. N of the $2L$ $n_{i\sigma}$ numbers are equal to one and the rest are zero. The possible ways of arranging such series of $n_{i\sigma}$ give the

configuration number

$$N_{\text{config}} = \begin{pmatrix} 2L \\ N \end{pmatrix}, \tag{2.2}$$

where the parentheses denote the binomial coefficient. If we fix the number of electrons with spin up $N_\uparrow$ (and $N_\downarrow = N - N_\uparrow$), the configuration number becomes $N_{\text{config}} = \begin{pmatrix} L \\ N_\uparrow \end{pmatrix} \begin{pmatrix} L \\ N_\downarrow \end{pmatrix}$. For the nonmagnetic half-filled case, $N_\uparrow = N_\downarrow = L/2$, and $N_{\text{config}} \sim 4^L/L$ when L is large [57].

For local spin models, e.g. the Heisenberg model, we assume $n_{i\uparrow} + n_{i\downarrow} = 1$, such that each orbital accommodates one electron. The complete Hilbert space thus has a dimension of $N_{\text{config}} = 2^L$ and has a tensor product structure

$$\mathcal{H} = \prod_i^{\otimes} \mathcal{H}_i, \tag{2.3}$$

where $\mathcal{H}_i$ is spanned by the local spin basis $\{|\uparrow\rangle_i, |\downarrow\rangle_i\}$.

The Hamiltonian $\hat{H}$ expressed in the many-body basis is a Hermitian matrix, which can be diagonalized to provide the solutions to the Schrödinger equation. For the time-dependent case, within the infinitesimal time interval $[t, t+\tau]$, we approximate $\hat{H}$ with its middle time value $\bar{H}(t) = \hat{H}(t+\tau/2)$, and the evolution from t to $t+\tau$ is

$$|\Psi(t+\tau)\rangle = \mathcal{T} e^{-i\int_t^{t+\tau} \hat{H}(\bar{t})d\bar{t}} |\Psi(t)\rangle \approx e^{-i\bar{H}(t)\tau}|\Psi(t)\rangle = \sum_\lambda e^{-iE_\lambda \tau}|\lambda\rangle\langle\lambda|\Psi(t)\rangle, \tag{2.4}$$

where the complete set of eigenstates $\bar{H}(t)|\lambda\rangle = E_\lambda|\lambda\rangle$ is required.

In the numerical implementation, the memory required for storing a single wave function has the order $\mathcal{O}(N_{\text{config}})$ and a direct diagonalization takes $\mathcal{O}(N_{\text{config}}^2)$ memory to store the matrix [58]. For $L > 20$ at half-filling, $\mathcal{O}(N_{\text{config}})$ corresponds to a memory exceeding hundreds of GB. Such rapid increase of the computational resource is referred to as the "exponential wall" [59]. Moreover, for the time-dependent case, one needs to diagonalize $\bar{H}(t)$ many times to evolve the system with the time-dependent $|\lambda\rangle$. As a result, the direct application of exact diagonalization is restricted to system with small size.

Lanczos method

The Hamiltonian matrix size can be reduced by considering symmetry and conversation laws. For instance, to calculate the ground state of a one-dimensional isotropic Heisenberg model, one can exploit the inversion symmetry of the system and the conservation of the z-component spin. However, if the same model is time-evolved with an inhomogeneous external magnetic field, one has to apply a distinct treatment because of the changes in the symmetry. To circumvent this, we introduce a more general approach to improve the efficiency of diagonalization, namely the Lanczos method [60]. The Lanczos algorithm was initially an iterative method to find the extreme eigenvalues and corresponding eigenstates of a sparse Hermitian matrix. We deal with many-body problems where the interactions are usually short-range and between two particles. Hence the Hamiltonian matrix is sparse and the Lanczos method can be used.

Below we outline the Lanczos algorithm. Starting from a chosen state $|\Phi_0\rangle$, a series of states $|\Phi_k\rangle = \hat{H}^k|\Phi_0\rangle$ can be constructed by applying the Hamiltonian iteratively. The Gram-Schmidt orthogonalization of $|\Phi_k\rangle$ gives a orthonormal set $\{|\varphi_k\rangle\}, k = 0, 1, \cdots, d_{\mathcal{K}}$, such that

$$\hat{H}|\varphi_k\rangle = \beta_k|\varphi_{k-1}\rangle + \alpha_k|\varphi_k\rangle + \beta_{k+1}|\varphi_{k+1}\rangle \tag{2.5}$$

$\{|\varphi_k\rangle\}$ span the so-called Krylov space [61] with a dimension $(d_{\mathcal{K}} + 1)$. The Hamiltonian on this $(d_{\mathcal{K}} + 1)$-dimensional space is tridiagonal. $d_{\mathcal{K}}$ is a convergence parameter and is usually much smaller than the size of the original Hilbert space. Thus the memory required to store and diagonalize the matrix is greatly reduced. The Lanczos method can be used for the ground state and the spectral function calculation, and for the time-evolution [57, 58].

1.2 Tensor Networks

As shown in the previous subsection, for a many-body problem, the Hilbert space has a tensor product structure. Accordingly, the size of the Hilbert space grows exponentially with the system size. However, not all of the exponentially large Hilbert space is necessary, e.g., for obtaining a reasonably approximate ground state. Consider a system with non-interacting fermions, we know the many-body system can be expressed by Slater determinants. The class of Slater determinants can be seen a variational class of wave functions, which has a much lower dimension than the actual many-body wave function. In the weak interaction regime, the Hartree-Fock method, as a variational approach, can be applied such that one tries to find an optimal Slater determinant $|\Phi\rangle$ which minimizes

$\langle\Phi|\hat{H}|\Phi\rangle$. The Tensor Networks (TNs) method is based on a similar concept: In strongly correlated systems, a low-dimensional manifold in the Hilbert space is used as a variational class of wavefunctions to approximate the actual state of interest [62]. TNs method is now among the standard numerical methods in the study of strongly correlated systems in low dimensions [63]. TNs method can deal with much larger system compared with ED and does not have the sign problem which restricts the quantum Monte Carlo method. Hence there are plenty of successful applications of TNs in quantum information and condensed matter physics [64]. Here we focus on discrete quantum spin systems in one- and two-dimensions, and introduce methods based on the simplest form of TN states, the matrix-product state (MPS). We list Ref.[65, 62, 63] for the historical developments of TNs and more advanced TN methods.

The fundamental objects of MPS are tensors, which are multidimensional arrays of complex numbers. A tensor $T^{s_1 s_2 \cdots s_R}$ has many indices s_i. Within our usage of MPS, the raising and lowering of indices are trivial , i.e., $T^{s_1 s_2} = T^{s_1}{}_{s_2} = T_{s_1 s_2}$. For each index, $s_i = 1, 2, \cdots, d_i$ with d_i the dimension of the index. The number of indices R is the rank of the tensor. A general wavefunction of a discrete spin-1/2 system can be written in the many-body basis,

$$|\psi\rangle = \sum_{\sigma_1 \sigma_2 \cdots \sigma_L} c(\sigma_1, \sigma_2, \cdots, \sigma_L) |\sigma_1, \sigma_2, \cdots, \sigma_L\rangle \tag{2.6}$$

where L is the site number and σ_i stands for the spin orientation on the i-th orbital. In the MPS context, $|\psi\rangle$ can be written as a product of L tensors,

$$|\psi\rangle = \sum_{\substack{\sigma_1 \sigma_2 \cdots \sigma_L \\ b_1 b_2 \cdots b_{L-1}}} [T_1]^{\sigma_1}_{b_1} [T_2]^{\sigma_2}_{b_1, b_2} \cdots [T_{L-1}]^{\sigma_{L-1}}_{b_{L-2}, b_{L-1}} [T_L]^{\sigma_L}_{b_{L-1}} |\sigma_1, \sigma_2, \cdots, \sigma_L\rangle, \tag{2.7}$$

where tensors on the "boundary" of the MPS "chain" (T_1 and T_L) have rank 2, and other tensors have rank 3, as shown schematically in Fig. 2.1. MPSs have a one-dimensional structure: each tensor, with a physical index and two internal indices, represents a spatial site of the physical system, and neighboring tensors along the MPS chain are contracted by a summation over an internal index. The dimensions of the internal indices are commonly referred to as bond dimensions. With large bond dimensions, the product of tensors completely reproduces $|\psi\rangle$. In practice, a MPS $|\psi'\rangle$ with small bond dimensions is desired which has large overlap with $|\psi\rangle$. Similar to wave functions, an operator

$$\hat{O} = \sum_{\substack{\sigma_1 \sigma_2 \cdots \sigma_L \\ \sigma'_1 \sigma'_2 \cdots \sigma'_L}} c(\sigma_1, \sigma_2, \cdots, \sigma_L; \sigma'_1, \sigma'_2, \cdots, \sigma'_L) |\sigma_1, \sigma_2, \cdots, \sigma_L\rangle \langle \sigma'_1, \sigma'_2, \cdots, \sigma'_L| \tag{2.8}$$

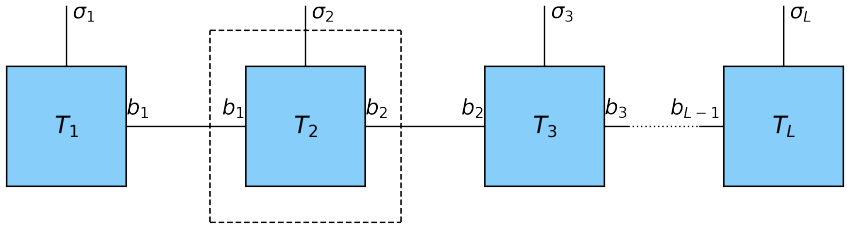

Figure 2.1: A sketch of a matrix-product state. The tensor in the dashed box has three indices: a physical index σ_2 represented by a vertical line, two internal indices b_1, b_2 which are horizontal lines.

can be expressed by a product of rank-4 (or 3) tensors. The structure of such a matrix-product operator (MPO) is shown in Fig. 2.2. Each tensor $[M_i]^{\sigma_i \sigma_i'}_{b_{i-1} b_i}$ acts on the local Hilbert space at site i.

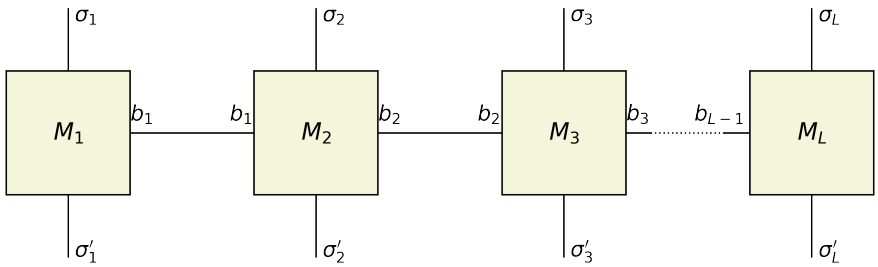

Figure 2.2: A sketch of a matrix-product operator. Each tensor not on the boundaries has two physical indices and two internal indices.

Ground state algorithm: Density matrix renormalization group

With a set of MPSs $|\psi_D\rangle$ with maximal bond dimension D, the variational method can be used to find an optimal MPS

$$|\Phi_D\rangle = \text{argmin}_{|\psi_D\rangle} \frac{\langle\psi_D|\hat{H}|\psi_D\rangle}{\langle\psi_D|\psi_D\rangle}, \tag{2.9}$$

which is an approximation to the ground state. A successful example of such variational method is the density matrix renormalization group (DMRG) algorithm [66, 67, 68, 69, 70]. The algorithm flow is as follows. One makes one tensor at site i as variable and keeps all others constant. One extremizes $\langle\psi_D|\hat{H}|\psi_D\rangle - \lambda\langle\psi_D|\psi_D\rangle$ where λ is the Langrangian multiplier, by solving an eigenvalue problem. Then one moves to another site i' and thus $|\psi_D\rangle$ and λ are updated iteratively. When λ does not change larger than a convergence parameter, the corresponding $|\psi_D\rangle$ is seen as the ground state. The computational

cost of the algorithm depends on many details such as the order in updating the tensors [70], and here we focus on why DMRG can work from the perspective of entanglement. For the quantum spin systems without long-range interactions, the Hamiltonians are local and strong quantum correlations happen between neighboring sites. If we consider a bipartite system with parts A and B, the entanglement between A and B is proportional to the surface between them, as stated by the area law [71, 72, 73, 74, 75]. In one dimension, the entanglement is finite for a gapped system [76] and scales with the system size as $\mathcal{O}(\log(L))$ for a gapless system. Accordingly, the low-energy eigenstates are restricted in a limited region of the Hilbert space. For a MPS, the bipartition is done on a bond along the MPS chain, and the bond dimension D is related to the entanglement between A and B. In this respect, MPS is also called the entanglement representation of quantum states [65]. Consequently, it is possible to find a good approximation of the ground state $|\Phi_0\rangle$, which actually contains limited entanglement and occupies a small portion of the Hilbert space, with a MPS with affordable bond dimensions. Moreover, if one time-evolves an initial state $|\Phi_0\rangle$ with a local Hamiltonian to a time $\mathcal{O}(\text{poly}(L))$, the reachable states are also restricted and cannot fully occupy the Hilbert space [77, 78]. In other words, the evolved state $|\Phi(t)\rangle$ can still be approximated by a MPS with not too large bond dimensions.

Time-evolution algorithm: Time-evolving block decimation

There are many time-evolution methods for MPSs and here we introduce one which is suitable for short-ranged Hamiltonians, namely the time-evolving block decimation (TEBD) algorithm. TEBD uses a Trotter-Suzuki decomposition [79, 80] of the evolution operator $\hat{U}(t+\tau,t) = e^{-i\bar{H}\tau}$, where τ is the time step and $\bar{H} = \hat{H}(t+\tau/2)$. Assuming that the Hamiltonian contains interactions only between neighboring sites along the MPS chain,

$$\hat{H} = \sum_{i}^{L-1} h_{i,i+1}, \tag{2.10}$$

the evolution operator can be written with the second order Trotter decomposition

$$\hat{U}(t+\tau,t) = e^{-i\bar{h}_{1,2}\tau/2} e^{-i\bar{h}_{2,3}\tau/2} \cdots e^{-i\bar{h}_{L-1,L}\tau/2} e^{-i\bar{h}_{L-1,L}\tau/2} \cdots e^{-i\bar{h}_{1,2}\tau/2} + \mathcal{O}(\tau^3). \tag{2.11}$$

Given the evolution interval $[t_0, t_f]$, the number of time steps is $(t_f - t_0)/\tau$, thus the accumulated error is of order $\mathcal{O}(\tau^3)(t_f - t_0)/\tau = \mathcal{O}(\tau^2)$. For each time step,

applying the evolution operator on the MPS will increase the bond dimensions, which is consistent with the growth of entanglement as the system is driven out of equilibrium. However, to fully capture the increase of entanglement after a long time-evolution, the required computational source should increase exponentially [70, 81, 82].

We summarize the features and limitations of MPS method. For ground state calculations, DMRG performs well with 1D systems with short-range interactions and open-end boundary conditions. DMRG can be applied to 2D systems by mapping the 2D sites to a MPS chain. However, for large 2D system which may contain long-range entanglement, the accuracy of DMRG decreases. For the time-evolution, both the error from the Trotter decomposition and the increase of the required computational resource restrict the application of TEBD to moderate system size and evolution-time. Finally we mention the extension of MPS to 1D infinite-size system, namely iDMRG and iTEBD [83, 84, 85] algorithms, and continuous MPS methods [86, 87]. They can be used to study systems in the thermodynamic limit or in the continuum limit.

1.3 Equilibrium Green's function

As introduced in section 2 of chapter 1, the one-particle Green's function can be the key factor for solving many-body problems. The Green's function, obtained by solving its equation of motion, can be used to provide the expectation values of observables corresponding to one-particle operators and the spectral function of the system. Due to the interaction term, the equation of motion of the one-particle Green's function involves a two-particle Green's function, which gives rise to a hierarchy problem. To solve the hierarchy problem, there are two approaches based on two different core dynamical quantities: the self-energy and the exchange-correlation field (Vxc). The former is widely used, and the latter was recently developed. Below we consider a system at equilibrium and briefly introduce the forms of the two approaches at zero temperature, followed by a comparison. The general equilibrium Green's function theory can be found in Ref. [88].

For a system with a one-body term $h^0(r) = -\frac{1}{2}\nabla^2 + V^{\text{ext}}(r)$ and two-body interactions $v(r, r')$, the Hamiltonian can be written as

$$\hat{H} = \int dr \hat{\psi}^\dagger(r) h^0(r) \hat{\psi}(r) + \tfrac{1}{2} \int dr dr' \hat{\psi}^\dagger(r) \hat{\psi}^\dagger(r') v(r, r') \hat{\psi}(r') \hat{\psi}(r), \quad (2.12)$$

where $\hat{\psi}(r)$ is the fermion field operator and $r = (\mathbf{r}, \sigma)$ is a combined space and spin variable. The time-ordered Green's function is defined in the Heisenberg

picture as

$$iG(1,2) := \langle \mathcal{T}\hat{\psi}(1)\hat{\psi}^{\dagger}(2)\rangle, \tag{2.13}$$

where the argument numbers label the space-time $1 := (r_1, t_1)$, $\langle . \rangle$ denotes the zero-temperature ground-state expectation value, and $\mathcal{T}$ is the time-ordering symbol. The equation of motion reads

$$[i\partial_{t_1} - h(1)]G(1,2) + iF(1,2) = \delta(1-2), \tag{2.14}$$

where the single-particle term $h(r) = h^0(r) + V^{\mathrm{H}}(r)$ contains the Hartree potential $V^{\mathrm{H}}(r) = \int dr' v(r,r')\rho(r')$, with $\rho(r)$ the ground-state electron density, and F is the interaction term,

$$F(1,2) := \int dr' v(r_1, r') \langle \mathcal{T}\hat{\rho}(r't_1)\hat{\psi}(r_1t_1)\hat{\psi}^{\dagger}(r_2t_2)\rangle - V^{\mathrm{H}}(r_1)iG(1,2), \tag{2.15}$$

and with $\hat{\rho}(rt) = \hat{\psi}^{\dagger}(rt)\hat{\psi}(rt)$ the density operator.

Self-energy and Hedin equations

In the self-energy approach, F is written as a spacetime convolution between the self-energy Σ and G,

$$F(1,2) = i \int d3\Sigma(1,3)G(3,2). \tag{2.16}$$

This form also follows naturally from many-body perturbation theory based on Wick's theorem [89]. For non-interacting case, $F = 0$, and the solution of the equation of motion is a non-interacting Green's function G_0,

$$[i\partial_{t_1} - h(1)]G_0(1,2) = \delta(1-2). \tag{2.17}$$

It follows from Eqs. (2.14) and (2.17) that G fulfills the following Dyson equation:

$$G(1,2) = G_0(1,2) + \int d3d4 G_0(1,3)\Sigma(3,4)G(4,2), \tag{2.18}$$

Eq. (2.18) can be written in an iterative form and in the Feynman diagram representation [88]. Eq. (2.18) has the same convolution structure as Eq. (2.16), which leads to a simple form in the frequency domain

$$G(\omega) = G_0(\omega) + G_0(\omega)\Sigma(\omega)G(\omega). \tag{2.19}$$

In numerical implementations, the self-energy needs to be approximated by, e.g., expanding F using Wick's theorem, or using the Schwinger functional derivative

technique [90, 91]. For the latter one, Σ can be expressed as a functional of G, which means Eq. (2.18) can be solved self-consistently. There is a set of self-consistent equations, known as Hedin equations, which couple G, Σ and three quantities, the screening W, the polarisation Π and vertex function Γ [92, 93]. We start with the screening effect.

In the linear response regime, an arbitrary external perturbative potential $V^{\text{ext}}(1)$ leads to an induced charge density

$$\rho^{\text{ind}}(1) = -\int d2R(1,2)V^{\text{ext}}(2), \tag{2.20}$$

where $R(1,2)$ is the response function. The induced charge density generates a potential via the Coulomb interaction

$$V^{\text{ind}}(1) = \int d2v(1-2)\rho^{\text{ind}}(2), \tag{2.21}$$

and effectively screens the original perturbation,

$$\begin{aligned}\tilde{V}^{\text{ext}}(1) &= V^{\text{ext}}(1) + V^{\text{ind}}(1) \\ &= V^{\text{ext}}(1) - \int d2d3v(1-2)R(2,3)V^{\text{ext}}(3).\end{aligned} \tag{2.22}$$

The screening plays an important role for a many-body system and lies behind the success of the GW approximation [94, 95, 96]. In the same spirit as Eq. (2.22), the screened Coulomb interaction is

$$W(1,2) = v(1-2) - \int d3d4v(1-3)R(3,4)v(4-2), \tag{2.23}$$

where the response is defined as the variation of the density with respective to a probing field ϕ,

$$R(1,2) := \frac{\delta\rho(1)}{\delta\phi(2)}, \tag{2.24}$$

where $\rho(1) = -iG(1,1^+)$. ϕ leads to a time-dependent term on top of the original Hamiltonian (Eq. (2.12)). Hence one can formulate G and its equation of motion in the interaction picture and use the Schwinger functional derivative to get exact relations between quantities like G, Σ and W. In section 2.1, we apply the functional derivative approach to a magnon system. To make comparison, here we outline the original Hedin equations. The derivation can be found in e.g. Refs. [97, 94]. With the probing field, the total field is

$$V(1) = V^{\text{H}}(1) + \phi(1). \tag{2.25}$$

The polarisation is defined as

$$\Pi(1,2) := \frac{\delta\rho(1)}{\delta V(2)}. \tag{2.26}$$

The vertex function is defined as

$$\Gamma(1,2,3) := -\frac{\delta G^{-1}(1,2)}{\delta V(3)} \tag{2.27}$$

where G^{-1} is the inverse Green's function. With the Dyson equation of G (Eq. (2.18)) being the first Hedin equation, other four equations are

$$\Sigma(1,2) = i\int d3d4W(4,1)G(1,3)\Gamma(3,2,4) \tag{2.28}$$

$$W(1,2) = v(1-2) + \int d3d4v(1-3)\Pi(3,4)W(4,2) \tag{2.29}$$

$$\Pi(1,2) = -i\int d3d4G(1,3)\Gamma(3,4,2)G(4,1^+) \tag{2.30}$$

$$\Gamma(1,2,3) = \delta(1-2)\delta(1-3) + \int d4d5d6d7\frac{\delta\Sigma(1,2)}{\delta G(4,5)}G(4,6)\Gamma(6,7,3)G(7,5). \tag{2.31}$$

Dynamical exchange-correlation field formalism

In comparison to the self-energy approach, the interaction term F (Eq. (2.15)) is interpreted as a direct coupling between the dynamical exchange-correlation field V^{xc} and G [21],

$$F(1,2) = V^{\mathrm{xc}}(1,2)iG(1,2). \tag{2.32}$$

An advantage of such form is that with the Vxc given, the Green's function can be solved by a time integral

$$\begin{aligned} G(r_1r_2,t) =& \theta(t)G(r_1r_2,0^+)e^{-i\left[V^{\mathrm{ext}}(r_1)+V^{\mathrm{H}}(r_1)\right]t}e^{-i\int_0^t\left[T(r_1r_2,\bar{t})+V^{\mathrm{xc}}(r_1r_2,\bar{t})\right]d\bar{t}} \\ &- \theta(-t)G(r_1r_2,0^-)e^{i\left[V^{\mathrm{ext}}(r_1)+V^{\mathrm{H}}(r_1)\right]t}e^{i\int_t^0\left[T(r_1r_2,\bar{t})+V^{\mathrm{xc}}(r_1r_2,\bar{t})\right]d\bar{t}}. \end{aligned} \tag{2.33}$$

Here, we consider the equilibrium case and thus set $t_2 = 0$ and $t = t_1 - t_2$. $T(r_1r_2,t) := \frac{-\frac{1}{2}\nabla^2 G(r_1r_2,t)}{G(r_1r_2,t)}$ stands for the kinetic energy. The Vxc can be interpreted as the Coulomb potential of the exchange-correlation hole

$$V^{\mathrm{xc}}(r_1r_2,t) = \int dr''v(r_1-r'')\rho^{\mathrm{xc}}(r_1,r_2,r'';t). \tag{2.34}$$

Considering a photoemission experiment, for instance, the added hole or electron disturbs the many-body system which is initially in the ground state and induces a temporal density fluctuation ρ^{xc}. Such fluctuation is spread via the Coulomb interaction and consequently the Vxc determines the Green's function. ρ^{xc} fulfills a sum rule

$$\int d\mathbf{r}''\rho^{\mathrm{xc}}(r,r',r'';t) = -\theta(-t)\delta_{\sigma\sigma''}, \tag{2.35}$$

and an exact constraint

$$\rho^{\mathrm{xc}}(r,r',r''=r;t) = -\rho(r), \tag{2.36}$$

where $\rho(r)$ is the electron density. Moreover, as shown in Eq. (2.34), due to the fact that the Coulomb interaction only depends on the inter-charge distance, the Vxc is the first radial moment of the spherical average of the exchange-correlation hole [98]. In other words, one can use a correct estimation of the first radial moment, instead of the complete knowledge of $\rho^{\mathrm{xc}}(r,r',r'';t)$, to obtain the exact Green's function. As mentioned in chapter 1, the local density approximation in density functional theory provides a good estimate of the first radial moment of the xc hole, which is relevant in determining the xc potential. In the dynamical xc field formalism, a dynamical xc hole exists. If we can find a good approximation of the spherical average of $\rho^{\mathrm{xc}}(r,r',r'';t)$, the xc field, and thus the Green's function, can be calculated. We expect $\rho^{\mathrm{xc}}(r,r',r'';t)$ from solvable systems can be used to provide such approximations. In section 3, we will extend the xc field formalism to spin systems and derive the sum rule for the spin dynamical xc hole.

1.4 Nonequilibrium Green's function

The nonequilibrium Green's function (NEGF) method is a very general, powerful and versatile approach to deal with systems in and out of equilibrium [99]. In this thesis, we focus on the fermionic one-particle NEGF at zero temperature. The general NEGF approach, including bosonic NEGF and finite temperature formalism, can be found in, e.g., Refs. [99, 100, 101, 102, 103, 104, 105].

To give an idea of how the method works, we consider a time-dependent problem, the Heisenberg picture field operators are

$$\hat{\psi}_{\mathrm{H}}(rt) = \hat{U}^{\dagger}(t,t_0)\hat{\psi}(r)\hat{U}(t,t_0), \tag{2.37}$$

where $\hat{U}(t,t_0)$ is the time-evolution operator

$$\hat{U}(t,t_0) = \mathcal{T}e^{-i\int_{t_0}^{t}\hat{H}(\bar{t})d\bar{t}}, \tag{2.38}$$

and $\hat{U}^\dagger(t,t_0) = \hat{U}(t,t_0)$. The expectation value of an operator $\hat{A}$ is time-dependent

$$A(t) = \langle\Psi(t_0)|\hat{U}(t_0,t)\hat{A}\hat{U}(t,t_0)|\Psi(t_0)\rangle. \tag{2.39}$$

One can define the time arguments on the Schwinger-Keldysh contour γ [106, 107] which is oriented and consists of a forward path $\gamma_- : t_0 \to t_1$ and a backward path $\gamma_+ : t_1 \to t_0$, $\gamma = \gamma_- \oplus \gamma_+$ as illustrated in Fig. 2.3. A time-ordering on

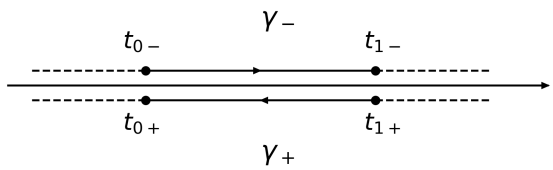

Figure 2.3: The Schwinger-Keldysh contour, figure adapted from Ref. [100]. For any real time t, t_- is on the forward branch γ_- and t_+ is on the backward branch γ_+. The dashed lines represent that the contour can be extended from minus infinity to t_0 corresponding to an adiabatic switch-on, and from t_1 to infinity, since $\hat{U}(t_0,t)\hat{A}\hat{U}(t,t_0) = \hat{U}(t_0,\infty)\hat{U}(\infty,t)\hat{A}\hat{U}(t,t_0)$. On the contour, $t_{0+} > t_{1+} > t_{1-} > t_{0-}$.

the contour, $\mathcal{T}_\gamma$, can be defined to put operators with earlier time arguments on γ to the right. Accordingly, the operator expectation value can be written as

$$A(t) = \langle\Psi(t_0)|\mathcal{T}_\gamma\big[e^{-i\int_\gamma \hat{H}(\bar{t})d\bar{t}}\hat{A}\big]|\Psi(t_0)\rangle. \tag{2.40}$$

The fermionic one-particle NEGF is defined with time arguments on the contour,

$$G(1,2) := \theta_\gamma(t_1 - t_2)G^>(1,2) + \theta_\gamma(t_2 - t_1)G^<(1,2), \tag{2.41}$$

where θ_γ is the contour step function and $G^>$, $G^<$ are the greater and lesser components with real time arguments (i.e., not on the contour)

$$G^>(1,2) = \frac{1}{i}\langle\hat{\psi}_{\rm H}(1)\hat{\psi}^\dagger_{\rm H}(2)\rangle, \tag{2.42}$$

$$G^<(1,2) = \frac{-1}{i}\langle\hat{\psi}^\dagger_{\rm H}(2)\hat{\psi}_{\rm H}(1)\rangle. \tag{2.43}$$

The retarded (R) and advanced (A) components are defined as

$$G^{\rm R}(1,2) = \theta_\gamma(t_1 - t_2)\big[G^>(1,2) - G^<(1,2)\big], \tag{2.44}$$

$$G^{\rm A}(1,2) = -\theta_\gamma(t_2 - t_1)\big[G^>(1,2) - G^<(1,2)\big]. \tag{2.45}$$

With those components, the NEGF can be written in matrix form

$$\mathbf{G} = \begin{pmatrix} G^{\mathrm{R}} & G^{<} \\ 0 & G^{\mathrm{A}} \end{pmatrix}, \tag{2.46}$$

where the arguments are implicit. The equation of motion of the one-particle NEGF is not closed since a two-particle NEGF

$$G_2(1,2;3,4) = (-i)^2 \langle \mathcal{T}_\gamma \hat{\psi}_{\mathrm{H}}(1)\hat{\psi}_{\mathrm{H}}(2)\hat{\psi}^\dagger_{\mathrm{H}}(4)\hat{\psi}^\dagger_{\mathrm{H}}(3)\rangle \tag{2.47}$$

is involved. The self-energy Σ is defined as

$$\int_\gamma d3\Sigma(1,3)G(3,2) = -i\int_\gamma d3v(1,3)G_2(1,2;3,3^+), \tag{2.48}$$

such that the equation of motion becomes closed,

$$\big[i\frac{\partial}{\partial t_1} - h(1)\big]G(1,2) = \delta(1-2) + \int_\gamma d3\Sigma(1,3)G(3,2). \tag{2.49}$$

On the RHS of Eq. (2.49), there is a convolution of two contour-ordered functions, which is called the collision integral

$$C(t,t') = \int_\gamma d\bar{t}A(t,\bar{t})B(\bar{t},t'). \tag{2.50}$$

The components of C are determined by the components of A and B, following the so-called Langreth rules [108, 99, 100, 101], which translate the propagators from Keldysh-contour time arguments to real time. Eq. (2.49) can be converted into a set of component equations, which are known as the Kadanoff-Baym equations (KBEs) [109]. The KBEs can be written in the form of a Dyson's equation, which reads in the matrix form

$$\mathbf{G} = \mathbf{G}_0 + \mathbf{G}_0\mathbf{\Sigma}\mathbf{G}, \tag{2.51}$$

where the non-interacting NEGF matrix $\mathbf{G}_0$ and the self-energy matrix $\mathbf{\Sigma}$ have the same components as $\mathbf{G}$.

The NEGF formalism can be applied for transport problems. We consider a general Hamiltonian which describes a small central region connected to several electronic reservoirs,

$$\hat{H} = \hat{H}_{\mathrm{c}} + \hat{H}_{\mathrm{r}} + \hat{H}_{\mathrm{t}} \tag{2.52}$$

where $\hat{H}_{\mathrm{c}}$ describes the central region with one-electron term h_{ij} and Coulomb interaction v_{ijmn},

$$\hat{H}_{\mathrm{c}} = \sum_{ij,\sigma} h_{ij}\hat{c}^{\dagger}_{i\sigma}\hat{c}_{j\sigma} + \frac{1}{2}\sum_{\substack{ijmn \\ \sigma\sigma'}} v_{ijmn}\hat{c}^{\dagger}_{i\sigma}\hat{c}^{\dagger}_{j\sigma'}\hat{c}_{m\sigma'}\hat{c}_{n\sigma}, \tag{2.53}$$

$\hat{H}_{\mathrm{r}}$ represents the non-interacting reservoirs where the α-th reservoir has eigenstates $\epsilon_{\alpha k}$,

$$\hat{H}_{\mathrm{r}} = \sum_{\alpha k\sigma} \epsilon_{\alpha k}\hat{d}^{\dagger}_{\alpha k\sigma}\hat{d}_{\alpha k\sigma}, \tag{2.54}$$

and $\hat{H}_{\mathrm{t}}$ stands for the tunneling between the central region and the reservoirs,

$$\hat{H}_{\mathrm{t}} = \sum_{\alpha k;i\sigma} (T_{\alpha k,i}\hat{d}^{\dagger}_{\alpha k\sigma}\hat{c}_{i\sigma} + \mathrm{h.c.}) \tag{2.55}$$

where the tunneling amplitude between the central region state i and the α-th reservoir state k is given by $T_{\alpha k,i}$. The KBEs of NEGF defined in the central region take the same form as Eq. (2.49) and the total self-energy is the sum of the correlation self-energy Σ^{c}, which results from the Coulomb interaction, and the embedding self-energy Σ^{emb}, which is due to the contact to the reservoirs,

$$\Sigma_{ij}(t,t') = \Sigma^{c}_{ij}(t,t') + \Sigma^{\mathrm{emb}}_{ij}(t,t'). \tag{2.56}$$

Σ^{emb} brings the degree of freedom of the reservoirs to the central region NEGF. The reservoirs are non-interacting, thus Σ^{emb} can be calculated analytically, and the equations closed. However, Σ^{c} needs to be approximated with e.g., many-body perturbation theory, and popular approximation methods are Hartree-Fock, second-Born, and GW. With the self-energy given and the Langreth rules applied, the real-time equation of motion of $G^{<}$ reads (orbital indices omitted)

$$\big[i\frac{\partial}{\partial t} - h^{\mathrm{HF}}(t)\big]G^{<}(t,t') = \int d\bar{t}\big[\Sigma^{<}(t,\bar{t})G^{\mathrm{A}}(\bar{t},t') + \Sigma^{\mathrm{R}}(t,\bar{t})G^{<}(\bar{t},t')\big], \tag{2.57}$$

where h^{HF} combines h_{ij} with the Hartree-Fock term of the Coulomb interaction. The self-energy can be seen as a kernel in the integro-differential Eq. (2.57) and represents the memory effect. As a result, the numerical effort of solving Eq. (2.57) scales as $\mathcal{O}(N_t^3)$ with N_t the number of time steps [110]. To reduce the computational time, an approximation scheme called the generalized Kadanoff-Baym ansatz (GKBA) was proposed [111]. The basic idea is to solve the density

matrix $\rho(t) = -iG^<(t,t)$ since it can be used to calculate the expectation values of one-body observables. The equation of motion of $\rho(t)$,

$$\frac{\partial}{\partial t}\rho(t) + i[h^{\mathrm{HF}}(t), \rho(t)] = -\int d\bar{t}\Big\{\big[\Sigma^<(t,\bar{t})G^{\mathrm{A}}(\bar{t},t) + \Sigma^{\mathrm{R}}(t,\bar{t})G^<(\bar{t},t)\big] + \mathrm{h.c.}\Big\}. \tag{2.58}$$

is not closed because of $G^<(t,t')$ and $G^{\mathrm{R}}(t,t') = \big[G^{\mathrm{A}}(t',t)\big]^\dagger$. $G^<$ can be written in terms of ρ and G^{R} as a Dyson's equation, and the GKBA is the lowest order expansion of $G^<$,

$$G^<(t,t') = -G^{\mathrm{R}}(t,t')\rho(t') + \rho(t)G^{\mathrm{A}}(t,t'). \tag{2.59}$$

Finally with a choice of G^{R}, Eq. (2.58) can be closed. For electronic system, the GKBA reduces the time scale to $\mathcal{O}(N_t^2)$ and preserves the causal structure and conservation laws [112]. The performance of the GKBA depends on, e.g., the quality of the choice of G^{R}. Also, we mention further approximations such as the G1-G2 scheme and the time-linear approach based on the GKBA which reduce the time scale to $\mathcal{O}(N_t)$ for quantum transport simulations [112].

In this section, we surveyed NEGF methods and the GKBA with an open fermonic system where electrons are exchanged between the central region and the electric reservoirs. This is the type of methods needed to study the systems in this thesis. The applications of NEGFs have been extended to include bosonic degrees of freedom [102, 113], and together with dynamical mean-field theory. For a recent review of NEGF methods, see Ref. [114].

2 Magnon self-energy

We study magnons with the spin-$\frac{1}{2}$ Heisenberg model [115], an effective model defined on a discrete lattice with local spin-$\frac{1}{2}$:s. The lattice contains in total N sites, which are labeled with $p = 1, 2, 3, \cdots, N$. At each site, a localized electron orbital gives rise to a local spin. Our focus here is the derivation of the magnon self-energy formalism using the model. The numerical results and a brief justification of the model will be provided in chapter 3. The time-independent model Hamiltonian is

$$\hat{H} = -\sum_{p<q} J_{pq}\hat{\mathbf{S}}_p \cdot \hat{\mathbf{S}}_q - \sum_p \mathbf{B}_p \cdot \hat{\mathbf{S}}_p, \tag{2.60}$$

where J is the symmetric exchange interaction and $\mathbf{B}$ is the external magnetic field. The spin field operators are

$$\hat{S}_p^\alpha = \sum_{\xi\xi'} \hat{c}_{p,\xi}^\dagger \boldsymbol{\sigma}_{\xi\xi'}^\alpha \hat{c}_{p,\xi'}, \tag{2.61}$$

where the superscripts in Greek letters $\alpha = x, y, z$ refer to the spin orientation, $\hat{c}_{p,\xi}^\dagger, \hat{c}_{p,\xi}$ are the creation (annihilation) operators of an electron with spin $\xi = \uparrow, \downarrow$ at site p, and $\boldsymbol{\sigma}^{x,y,z}$ denote for the Pauli spin matrices. The creation and annihilation of a magnon can be related to the spin ladder operators: $\hat{S}_p^\pm := \hat{S}_p^x \pm i\hat{S}_p^y$. Following the general formalism (2.12)-(2.15), the spin Green's function is defined as

$$iG_{pq}^{\alpha\beta}(t,t') = \theta(t-t')\langle \hat{S}_p^\alpha(t)\hat{S}_q^\beta(t')\rangle + \theta(t'-t)\langle \hat{S}_q^\beta(t')\hat{S}_p^\alpha(t)\rangle, \tag{2.62}$$

where θ is the Heaviside step function and $\hat{S}_p^\alpha(t) = e^{i\hat{H}t}\hat{S}_p^\alpha e^{-i\hat{H}t}$ is the Heisenberg picture spin field operator. The equation of motion of the magnon Green's function is

$$i\partial_t G_{pq}^{\alpha\beta}(t,t') = \langle \mathcal{T}\big[i[\hat{H}, \hat{S}_p^\alpha(t)]\hat{S}_q^\beta(t')\big]\rangle + \delta(t-t')\delta_{pq}\langle[\hat{S}_p^\alpha, \hat{S}_q^\beta]\rangle \tag{2.63}$$

where the first commutator is

$$[\hat{H}, \hat{S}_p^\alpha(t)] = e^{i\hat{H}t}[\hat{H}, \hat{S}_p^\alpha]e^{-i\hat{H}t}. \tag{2.64}$$

For different spin channels α and β, the equation of motion of $G^{\alpha\beta}$ can be derived using the commutation relation of spin operators. In general, a different spin channel $G^{\alpha'\beta}$ can be included and the equation of motion is therefore not closed. In that case, all related G:s can be treated as matrix element, and the equation of motion in matrix form is closed. Now we consider the external field in the z-direction, $\mathbf{B}_p = B_p^z\hat{\mathbf{z}}$. The total z-component spin is thus conserved. We focus on one matrix element G^{+-}, which can be related to the spin structure factor. It has a closed equation of motion,

$$\Big[i\partial_t - B_p^z\Big]G_{pq}^{+-}(t,t') + i\sum_l J_{pl}\big[\langle lp,t;q,t'\rangle - \langle pl,t;q,t'\rangle\big] = 2\delta(t-t')\delta_{pq}\langle \hat{S}_p^z(t)\rangle, \tag{2.65}$$

where the three-site correlation

$$\langle lp,t;q,t'\rangle := \langle \mathcal{T}[\hat{S}_l^z(t^+)\hat{S}_p^+(t)\hat{S}_q^-(t')]\rangle \tag{2.66}$$

can be seen as a higher order Green's function. We define the core part as the three-site correlation minus its approximate factorization,

$$\langle lp,t;q,t'\rangle^{\mathrm{c}} := \langle \mathcal{T}[\hat{S}_l^z(t^+)\hat{S}_p^+(t)\hat{S}_q^-(t')]\rangle - \langle \hat{S}_l^z(t)\rangle iG_{pq}^{+-}(t,t'). \tag{2.67}$$

The magnon self-energy Σ is defined such that the core interaction is represented by a convolution between Σ and G:

$$\sum_l \int dt'' \Sigma_{pl}(t,t'') i G^{+-}_{lq}(t'',t') = \sum_l J_{pl} \big[\langle lp,t;q,t' \rangle^{\mathrm{c}} - \langle pl,t;q,t' \rangle^{\mathrm{c}} \big]. \tag{2.68}$$

Accordingly, the equation of motion Eq. (2.65) is rewritten as

$$\begin{aligned} \big[i\partial_t - B^z_p - V^{\mathrm{H}}_p \big] G^{+-}_{pq}(t,t') = & \sum_l \int dt'' \Sigma_{pl}(t,t'') G^{+-}_{lq}(t'',t') \\ & + \sum_l V^{\mathrm{F}}_{pl} G^{+-}_{lq}(t,t') + 2\delta(t-t')\delta_{pq} \langle \hat{S}^z_p(t) \rangle, \end{aligned} \tag{2.69}$$

where

$$V^{\mathrm{H}}_p := \sum_l J_{pl} \langle \hat{S}^z_l(t) \rangle \tag{2.70}$$

$$V^{\mathrm{F}}_{pl} := -J_{pl} \langle \hat{S}^z_p(t) \rangle \tag{2.71}$$

can be understood as the time-independent Hartree- and Fock-like terms, respectively, since the system is at equilibrium. Next we show that Σ can be expressed as the response of G to a variation in $\mathbf{B}$.

2.1 Schwinger functional derivative technique

Following Hedin's derivation of his well-known equations [92], we consider a time-dependent local probing field $\mathbf{w}$, such that the total Hamiltonian $\hat{H}(t)$ contains the time-independent term $\hat{H}_0$ (Eq. (2.60)) and the probing term $\hat{H}_1 = -\sum_p \mathbf{w}_p(t) \cdot \mathbf{S}_p$. Below we derive the response of G to $\mathbf{w}$ and show that the magnon self-energy Σ can be written as a functional of G when $\mathbf{w}$ is set to zero, such that the equation of motion of G can be solved self-consistently. In the interaction picture,

$$|\Psi_I(t)\rangle = e^{i\hat{H}_0 t} |\Psi(t)\rangle \tag{2.72}$$

where $i\partial_t |\Psi(t)\rangle = \hat{H}(t)|\Psi(t)\rangle$. We use a simplified notation $1 \equiv (p_1, t_1)$, which carries lattice site label and time variable. $\int d1$ refers to an integration over time and a summation over sites. The one-particle Green's function can be expressed as a functional of $\mathbf{w}$ in the interaction picture as

$$iG^{\alpha\beta}(1,2) := \frac{\langle \Psi_0 | \mathcal{T}[\hat{U} \hat{S}^{\alpha}_I(1) \hat{S}^{\beta}_I(2)] | \Psi_0 \rangle}{\langle \Psi_0 | \hat{U} | \Psi_0 \rangle}, \tag{2.73}$$

where the interaction picture ground state $|\Psi_0\rangle := |\Psi_I(0)\rangle$ is the same as the Heisenberg picture ground state in Eq. (2.13) and (2.62), the operators, with subscripts I denoting the interaction picture, are also independent of $\mathbf{w}$, and $\hat{U}$ is the evolution operator,

$$\hat{U} = \mathcal{T}\exp\Big[i\int_{-\infty}^{\infty} d1 \sum_{\gamma} w^{\gamma}(1)\hat{S}_I^{\gamma}(1)\Big]. \tag{2.74}$$

A variation in the probing field affects G only through $\hat{U}$, which gives

$$\frac{\delta G^{\alpha\beta}(1,2)}{\delta w^{\gamma}(3)} = \frac{\langle\Psi_0|\mathcal{T}\hat{U}\hat{S}_I^{\gamma}(3)\hat{S}_I^{\alpha}(1)\hat{S}_I^{\beta}(2)|\Psi_0\rangle}{\langle\Psi_0|\hat{U}|\Psi_0\rangle} - iG^{\alpha\beta}(1,2)\frac{\langle\Psi_0|\mathcal{T}\hat{U}\hat{S}_I^{\gamma}(3)|\Psi_0\rangle}{\langle\Psi_0|\hat{U}|\Psi_0\rangle}. \tag{2.75}$$

When $\mathbf{w}$ is set to zero, the RHS of Eq. (2.75) returns to the core three-site correlation (Eq. (2.67)). We then relate the self-energy defined in Eq. (2.68) to the functional derivative $\delta G^{+-}/\delta w^z$,

$$\int d3\Sigma(1,3)G^{+-}(3,2) = -i\int d3J(1-3)\Big[\frac{\delta G^{+-}(1,2)}{\delta w^z(3)} - \frac{\delta G^{+-}(3,2)}{\delta w^z(1)}\Big]_{\mathbf{w}\to 0}, \tag{2.76}$$

where $J(1-3) = J_{p_1p_3}\delta(t_1-t_3)$ returns to the exchange coupling on lattice. We stress that the self-energy coupled to other spin channels $\alpha\beta$ can in general be expressed as a different functional derivative $\delta G^{\alpha'\beta}/\delta w^{\gamma}$, which makes the matrix form for the equation of motion necessary. Again, we consider the closed equation of G^{+-} by setting $\mathbf{w}$ and $\mathbf{B}$ in z-direction. Below we keep spin label $^{+-}$ implicit, and the equation of motion with the probing field reads

$$\big[i\partial_{t_1} - \tilde{B}(1) - V^{\mathrm{H}}(1)\big]G(1,2) = \int d3\big[V^{\mathrm{F}}(1,3) + \Sigma(1,3)\big]G(3,2) + 2\delta(1-2)\langle\hat{S}^z(1)\rangle, \tag{2.77}$$

where $\tilde{B}$ contains the probing field,

$$\tilde{B}(1) = B^z(1) + w^z(1), \tag{2.78}$$

and $V^{\mathrm{H}}(1) = \int d2J(1-2)\langle\hat{S}^z(2)\rangle$, $V^{\mathrm{F}}(1,2) = -J(1-2)\langle\hat{S}^z(1)\rangle$ can go back to lattice case when $\mathbf{w}$ is switched off. The equation of motion can be written with G and $\delta G/\delta w^z$:

$$\big[i\partial_{t_1} - \tilde{B}(1) - V^{\mathrm{H}}(1)\big]G(1,2) = \int d3V^{\mathrm{F}}(1,3)G(3,2) + 2\delta(1-2)\langle\hat{S}^z(1)\rangle - i\int d3J(1-3)\Big[\frac{\delta G(1,2)}{\delta w^z(3)} - \frac{\delta G(3,2)}{\delta w^z(1)}\Big], \tag{2.79}$$

since $\langle \hat{S}^z(1) \rangle$ can be written as

$$\langle \hat{S}^z(1) \rangle = \frac{1}{2}\big[iG(1^+,1) - iG(1,1^+)\big], \tag{2.80}$$

where the superscript + refers to an infinitesimal increment in time variable. The inverse of G is defined as

$$\int d3G(1,3)G^{-1}(3,2) = \int d3G^{-1}(1,3)G(3,2) = \delta(1-2). \tag{2.81}$$

The explicit form of G^{-1} can be obtained by multiplying G^{-1} from right on both sides of Eq. (2.77) and integrating over spacetime,

$$\boxed{G^{-1}(1,2) = \frac{1}{2\langle \hat{S}^z(1) \rangle}\Big\{\big[i\partial_{t_1} - V^{\mathrm{H}}(1) - \tilde{B}(1)\big]\delta(1-2) - \Sigma(1,2)\Big\} + \frac{1}{2}J(1-2)}, \tag{2.82}$$

where $V^{\mathrm{F}}(1,2)/\langle \hat{S}^z(1) \rangle = -J(1,2)$ is used. Here and below, we highlight the key equations of this chapter in boxes. They are related to our numerical results in the next two chapters. With the identity $\frac{\delta G}{\delta w^z}G^{-1} + G\frac{\delta G^{-1}}{\delta w^z} = 0$, the self-energy can be re-cast from Eq. (2.76) as

$$\boxed{\Sigma(1,2) = i\int d3d4J(1-3)\Big[G(1,4)\frac{\delta G^{-1}(4,2)}{\delta w^z(3)} - G(3,4)\frac{\delta G^{-1}(4,2)}{\delta w^z(1)}\Big]_{\mathbf{w}\to 0}}. \tag{2.83}$$

We define a "non-interacting" Green's function G_0 which is the solution to

$$\big[i\partial_{t_1} - \tilde{B}(1) - V^{\mathrm{H}}(1)\big]G_0(1,2) = \int d3V^{\mathrm{F}}(1,3)G_0(3,2) + 2\delta(1-2)\langle \hat{S}^z(1) \rangle, \tag{2.84}$$

and has an inverse similar to Eq. (2.81). Then the inverse of G_0 can be written as

$$G_0^{-1}(1,2) = \frac{1}{2\langle \hat{S}^z(1) \rangle}\Big\{\big[i\partial_{t_1} - V^{\mathrm{H}}(1) - \tilde{B}(1)\big]\delta(1-2)\Big\} + \frac{1}{2}J(1-2). \tag{2.85}$$

Accordingly, Eq. (2.82) can be expressed with G_0^{-1}:

$$G^{-1}(1,2) = G_0^{-1}(1,2) - \frac{\Sigma(1,2)}{2\langle \hat{S}^z(1) \rangle}, \tag{2.86}$$

and a Dyson-like equation for G reads

$$G(1,2) = G_0(1,2) + \int d3d4G_0(1,3)\frac{\Sigma(3,4)}{2\langle \hat{S}^z(3) \rangle}G(4,2) \tag{2.87}$$

which takes the same form as the original Hedin equation

$$G(1,2) = G_0(1,2) + \int d3d4 G_0(1,3)\tilde{\Sigma}(3,4)G(4,2) \tag{2.88}$$

with

$$\tilde{\Sigma}(3,4) := \frac{\Sigma(3,4)}{2\langle \hat{S}^z(3)\rangle}. \tag{2.89}$$

In principle, one can follow Hedin's original approach and define a total field as the sum of the Hartree term and the probing field,

$$V(1) = V^{\mathrm{H}}(1) + w^z(1) \tag{2.90}$$

and try to construct quantities with $\delta/\delta V$. With the polarisation

$$\Pi(1,2) := \frac{\delta\langle \hat{S}^z(1)\rangle}{\delta V(2)}, \tag{2.91}$$

the vertex function is

$$\begin{aligned}\Gamma(1,2,3) &:= \frac{\delta G^{-1}(1,2)}{\delta V(3)} \\ &= \frac{-\delta(1-3)\delta(1-2)}{2\langle \hat{S}^z(1)\rangle} - \big[G_0^{-1}(1,2) - \frac{1}{2}J(1-2)\big]\frac{\Pi(1,3)}{\langle \hat{S}^z(1)\rangle} - \frac{\delta\tilde{\Sigma}(1,2)}{\delta V(3)}.\end{aligned} \tag{2.92}$$

And $\tilde{\Sigma}$ can be written as

$$\begin{aligned}\tilde{\Sigma}(1,2) = \frac{i}{2\langle \hat{S}^z(1)\rangle}\int d3d4d5 J(1-3)\Big[&G(1,4)\Gamma(4,2,5)\frac{\delta V(5)}{\delta w^z(3)} \\ &- G(3,4)\Gamma(4,2,5)\frac{\delta V(5)}{\delta w^z(1)}\Big].\end{aligned} \tag{2.93}$$

The first term on the RHS of Eq. (2.93) allows a natural definition of magnon screening

$$\tilde{W}(1,5) := \frac{1}{2\langle \hat{S}^z(1)\rangle}\int d3 J(1-3)\frac{\delta V(5)}{\delta w^z(3)}, \tag{2.94}$$

however, the second term is Fock-like and suggests a term

$$\tilde{W}^{\mathrm{F}}(1,3,5) := \frac{1}{2\langle \hat{S}^z(1)\rangle} J(1-3)\frac{\delta V(5)}{\delta w^z(1)}. \tag{2.95}$$

Hence we can express $\tilde{\Sigma}$ with G, Γ, $\tilde{W}$ and $\tilde{W}^{\mathrm{F}}$,

$$\tilde{\Sigma}(1,2) = i\int d4d5\Big[\tilde{W}(1,5)G(1,4) - \int d3\tilde{W}^{\mathrm{F}}(1,3,5)G(3,4)\Big]\Gamma(4,2,5). \quad (2.96)$$

From Eq. (2.92) and Eq. (2.96) we notice that the total field formalism produces rather complicated relations between quantities as $\tilde{\Sigma}$ and Γ. The reason may be the Fock-like term and $\langle\hat{S}^z\rangle$ in the equation of motion, which come from the fact that G is defined with spin field operators. We continue to derive the equations for $\tilde{W}$:

$$\begin{aligned}\tilde{W}(1,5) &= \frac{1}{2\langle\hat{S}^z(1)\rangle}\int d3J(1-3)\big[\delta(5-3) + \frac{\delta V^{\mathrm{H}}(5)}{\delta w^z(3)}\big] \\ &= \frac{J(1-5)}{2\langle\hat{S}^z(1)\rangle} + \frac{1}{2\langle\hat{S}^z(1)\rangle}\int d2d3d4J(1-3)J(5-2)\frac{\delta\langle\hat{S}^z(2)\rangle}{\delta V(4)}\frac{\delta V(4)}{\delta w^z(3)} \\ &= \frac{J(1-5)}{2\langle\hat{S}^z(1)\rangle} + \int d2J(5-2)\Pi(2,4)\tilde{W}(1,4). \end{aligned} \quad (2.97)$$

Similarly,

$$\begin{aligned}\tilde{W}^{\mathrm{F}}(1,3,5) &= \frac{J(1-3)\delta(1-5)}{2\langle\hat{S}^z(1)\rangle} + \frac{J(1-3)}{2\langle\hat{S}^z(1)\rangle}\int d2d4J(5-2)\frac{\delta\langle\hat{S}^z(2)\rangle}{\delta V(4)}\frac{\delta V(4)}{\delta w^z(1)} \\ &= \frac{J(1-3)\delta(1-5)}{2\langle\hat{S}^z(1)\rangle} + \int d2J(5-2)\Pi(2,4)\tilde{W}^{\mathrm{F}}(1,3,4). \end{aligned} \quad (2.98)$$

And Π is given by

$$\begin{aligned}\Pi(1,2) &= \frac{1}{2}\frac{\delta[iG(1^+,1) - iG(1,1^+)]}{\delta V(2)} \\ &= -\frac{i}{2}\int d3d4\Big[G(1^+,3)\Gamma(3,4,2)G(4,1) - G(1,3)\Gamma(3,4,2)G(4,1^+)\Big], \end{aligned} \quad (2.99)$$

Finally we close the equations by an approximation of the vertex function

$$\begin{aligned}\Gamma(1,2,3) &\approx \frac{-\delta(1-3)\delta(1-2)}{2\langle\hat{S}^z(1)\rangle} - \frac{\delta\tilde{\Sigma}(1,2)}{\delta V(3)} \\ &= \frac{-\delta(1-3)\delta(1-2)}{2\langle\hat{S}^z(1)\rangle} - \int d4d5\frac{\delta\tilde{\Sigma}(1,2)}{\delta G(4,5)}\frac{\delta G(4,5)}{\delta V(3)} \\ &= \frac{-\delta(1-3)\delta(1-2)}{2\langle\hat{S}^z(1)\rangle} + \int d4d5d6d7\frac{\delta\tilde{\Sigma}(1,2)}{\delta G(4,5)}G(4,6)\Gamma(6,7,3)G(7,5) \end{aligned} \quad (2.100)$$

which is based on the assumption that $\Pi(1,3)/\langle\hat{S}^z(1)\rangle$, the relative change of $\langle\hat{S}^z(1)\rangle$ due to the variation at another space time, is small. We compare the original Hedin equations and magnon Hedin equations schematically in Fig. 2.4. Alternatively, we can define the vertex function with the probing field

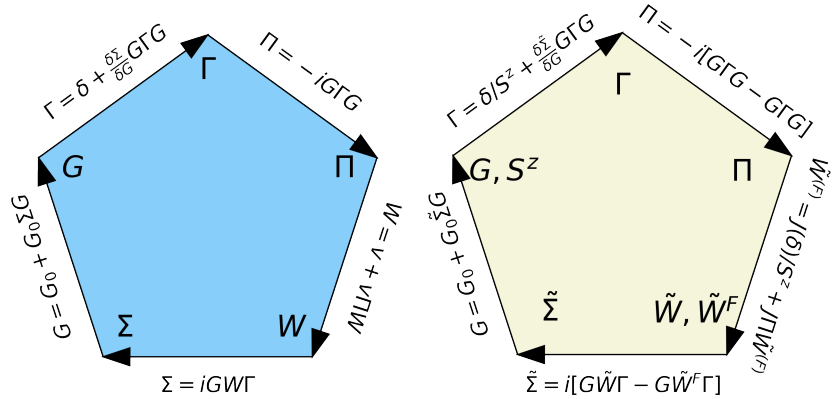

Figure 2.4: A comparison between origin Hedin equations (left) and magnon Hedin equations (right). For the magnon case, the Green's function is defined with spin field operators. Consequently, Fock-like terms are involved in the equations. An approximation is made to simplify the vertex function.

$$\Lambda(1,2,3) := \frac{\delta G^{-1}(1,2)}{\delta w^z(3)} \tag{2.101}$$

To obtain Λ, we take functional derivative $\delta/\delta w^z(3)$ to Eq. (2.82), and get

$$\begin{aligned}\Lambda(1,2,3) = \frac{1}{2\langle\hat{S}^z(1)\rangle}\Big\{ &-\big[\frac{\delta V^{\mathrm{H}}(1)}{\delta w^z(3)} + \delta(1-3)\big]\delta(1-2) \\ &-\frac{\delta V^{\mathrm{F}}(1,2)}{\delta w^z(3)} - \frac{\delta\Sigma(1,2)}{\delta w^z(3)} - 2R(1,3)G^{-1}(1,2)\Big\}\end{aligned} \tag{2.102}$$

where the response function

$$R(1,2) := \frac{\delta\langle\hat{S}^z(1)\rangle}{\delta w^z(2)} \tag{2.103}$$

is also contained in $\delta V^{\mathrm{H}}/\delta w^z$ and $\delta V^{\mathrm{F}}/\delta w^z$. The vertex function Λ and the variation of G are related, following the definition of G^{-1},

$$\frac{\delta G(1,2)}{\delta w^z(3)} = -\int d4d5G(1,4)\Lambda(4,5,3)G(5,2). \tag{2.104}$$

Finally we express R in terms of G to close the equations. In the functional derivative form,

$$R(1,2) = i\frac{\langle\Psi_0|\mathcal{T}\hat{U}\hat{S}^z_I(1)\hat{S}^z_I(2)|\Psi_0\rangle}{\langle\Psi_0|\hat{U}|\Psi_0\rangle} - i\frac{\langle\Psi_0|\mathcal{T}\hat{U}\hat{S}^z_I(1)|\Psi_0\rangle}{\langle\Psi_0|\hat{U}|\Psi_0\rangle}\frac{\langle\Psi_0|\mathcal{T}\hat{U}\hat{S}^z_I(2)|\Psi_0\rangle}{\langle\Psi_0|\hat{U}|\Psi_0\rangle}. \tag{2.105}$$

The equation of motion for $\langle\hat{S}^z(1)\rangle$ can be written with G:

$$\partial_{t_1}\langle\hat{S}^z(1)\rangle = -\int d3J(1-3)\Big[G(1,3) - G(3,1)\Big]. \tag{2.106}$$

Applying functional derivative with Eq. (2.106) gives

$$\begin{aligned}\partial_{t_1}R(1,2) &= -\int d3J(1-3)\frac{\delta}{\delta w^z(2)}[G(1,3) - G(3,1)] \\ &= \int d3d4d5J(1-3)\Big[G(1,4)\Lambda(4,5,2)G(5,3) - G(3,4)\Lambda(4,5,2)G(5,1)\Big].\end{aligned} \tag{2.107}$$

Eq. (2.82), (2.83), give a set of exact equations which can be solved by iteration. Next we perform approximations to get more explicit forms. Λ can be estimated by considering only the first term on the RHS of Eq. (2.102)

$$\Lambda^0(1,2,3) = -\frac{1}{2\langle\hat{S}^z(1)\rangle}[J(1-\underline{4})*R(\underline{4},3) + \delta(1-3)]\delta(1-2) \tag{2.108}$$

where $*$ denotes an integral over the underlined spacetime variable. $\delta G/\delta w^z$ can be approximated by taking functional derivative of Eq. (2.77) and neglecting the second derivative term $\delta^2 G/\delta w^2$,

$$\begin{aligned}i\partial_{t_1}\frac{\delta G(1,2)}{\delta w^z(3)} = \quad & G(1,2)\delta(1-3) + 2R(1,3)\delta(1-2) \\ & + J(1-\underline{4})*\Big\{R(\underline{4},3)G(1,2) + \langle\hat{S}^z(\underline{4})\rangle\frac{\delta G(1,2)}{\delta w^z(3)} \\ & - R(1,3)G(\underline{4},2) - \langle\hat{S}^z(1)\rangle\frac{\delta G(\underline{4},2)}{\delta w^z(3)}\Big\}.\end{aligned} \tag{2.109}$$

Starting with g computed at the mean-field level, we can get corresponding $\langle\hat{S}^z\rangle, V^{\rm H}, V^{\rm F}$ (the constants and spacetime variables are not shown for simplicity of the text)

$$\langle\hat{S}^z\rangle = (g-g), \tag{2.110}$$

$$V^{\rm H} = J*(g-g), \tag{2.111}$$

$$V^{\rm F} = -J(g-g), \tag{2.112}$$

and Λ^0, R,

$$\Lambda^0 = -(J * R + \delta)\delta / \langle \hat{S}^z \rangle, \tag{2.113}$$

$$\partial_t R = J * (g * \Lambda^0 * g - g * \Lambda^0 * g), \tag{2.114}$$

and thus $\delta G / \delta w^z, \Sigma, G$

$$\partial_t \frac{\delta G}{\delta w^z} = g\delta + R\delta + J * Rg + J * \langle \hat{S}^z \rangle \frac{\delta G}{\delta w^z} - RJ * g - \langle \hat{S}^z \rangle J * \frac{\delta G}{\delta w^z}, \tag{2.115}$$

$$\Sigma = J * (g * \Lambda^0 - g * \Lambda^0), \tag{2.116}$$

$$G = g + g * \Sigma * g. \tag{2.117}$$

In conclusion, we get a set of approximate magnon Hedin equations which can be solved self-consistently.

3 Spin exchange-correlation field formalism

The Vxc formalism introduced in section 1.3 can be extended to local spin systems. In the charge case, the Vxc couples to Green's functions defined with fermionic field operators. For local spin systems, Green's function is naturally defined with local spin operators, and the interaction term effectively originates from spin-spin interactions (e.g. the Heisenberg exchange). The spin exchange-correlation hole can be defined accordingly. Here, we derive the sum rule and the exact constraint for the spin exchange-correlation hole with the isotropic Heisenberg model with spin-1/2. Some essential terms and definitions introduced in section 2 are repeated here to ensure readability. The equation of motion of the Green's function $G_{pq}(t) := \langle \mathcal{T} \hat{S}_p^+(t) \hat{S}_q^-(0) \rangle$ reads

$$i\partial_t G_{pq}(t) + iF_{pq}(t) = 2\delta_{pq}\delta(t)\langle \hat{S}_p^z \rangle, \tag{2.118}$$

where we set $t' = 0$ as the system is at equilibrium and the interaction term is

$$F_{pq}(t) = -J \sum_l [\langle pl, t; q \rangle - \langle lp, t; q \rangle], \tag{2.119}$$

where for each site p the Heisenberg exchange is nonzero only for its nearest neighbor sites l and

$$\langle lp, t; q \rangle \quad := \quad \langle \mathcal{T} \hat{S}_l^z(t^+) \hat{S}_p^+(t) \hat{S}_q^-(0) \rangle \tag{2.120}$$

is the three-site correlation. The correlator $g_{lpq}(t)$ and the spin exchange-correlation hole $\rho^{\rm xc}_{lpq}(t)$ are defined to fulfill:

$$\begin{aligned}
\langle lp,t;q\rangle &= iG_{pq}(t)g_{lpq}(t)\langle\hat{S}^z_l(t)\rangle & (2.121)\\
\rho^{\rm xc}_{lpq}(t)iG_{pq}(t) &= -\langle lp,t;q\rangle + \langle\hat{S}^z_l\rangle iG_{pq}(t) & (2.122)\\
\rho^{\rm xc}_{lpq}(t) &= -\big[g_{lpq}(t)-1\big]\langle\hat{S}^z_l\rangle. & (2.123)
\end{aligned}$$

Note that both $g_{lpq}(t)$ and $\rho^{\rm xc}_{lpq}(t)$ can be fully determined given G. Next, we derive a sum rule and an exact constraint of $\rho^{\rm xc}_{lpq}(t)$ for system with conserved total z-spin. The sum rule and the exact constraint hold for arbitrary G. For $t>0$,

$$\sum_l\langle lp,t;q\rangle = \langle e^{i\hat{H}t}\sum_l\hat{S}^z_l\hat{S}^+_p e^{-i\hat{H}t}\hat{S}^-_q\rangle = S^z iG_{pq}(t), \tag{2.124}$$

where we consider that the total z-spin operator $\sum_l\hat{S}^z_l$ commutes with the Heisenberg Hamiltonian and thus $\sum_l\hat{S}^z_l|\Psi_0\rangle = S^z|\Psi_0\rangle$. For $t<0$,

$$\begin{aligned}
\sum_l\langle lp,t;q\rangle &= \sum_l\Big[\langle\hat{S}^-_q(0)\hat{S}^+_p(t)\hat{S}^z_l(t)\rangle + \langle\hat{S}^-_q(0)\hat{S}^+_p(t)\rangle\delta_{pl}\Big]\\
&= (1+S^z)iG_{pq}(t). & (2.125)
\end{aligned}$$

Eqs. (2.124) and (2.125) can be written in a compact form as

$$\sum_l\langle lp,t;q\rangle = \big[\theta(-t)+S^z\big]iG_{pq}(t). \tag{2.126}$$

Therefore the correlator fulfills

$$\begin{aligned}
\sum_l iG_{pq}(t)\big[g_{lpq}(t)-1\big]\langle\hat{S}^z_l\rangle &= \sum_l\langle lp,t;q\rangle - \sum_l\langle\hat{S}^z_l\rangle\\
&= \theta(-t)iG_{pq}(t), & (2.127)
\end{aligned}$$

from which the sum rule can be retrieved:

$$\boxed{\sum_l\rho^{\rm xc}_{lpq}(t) = -\theta(-t).} \tag{2.128}$$

Consider a special case $l=p$ and for local spins,

$$\hat{S}^z_p\hat{S}^+_p = \frac{1}{2}\hat{S}^+_p, \tag{2.129}$$

the three-site correlation reduces to

$$\langle pp,t;q\rangle = \langle \mathcal{T}\hat{S}_p^z(t^+)\hat{S}_p^+(t)\hat{S}_q^-(0)\rangle = \frac{1}{2}\langle \mathcal{T}\hat{S}_p^+(t)\hat{S}_q^-(0)\rangle \tag{2.130}$$

and from the definition of the spin exchange-correlation hole we get the exact constraint

$$\boxed{\rho^{\rm xc}_{ppq}(t) = -\frac{1}{2} + \langle \hat{S}_p^z\rangle.} \tag{2.131}$$

Next, we derive the low-order approximation of the spin Vxc. We define the vertex function as the core part of the three-site correlation

$$\Lambda_{lpq}(t) \;\; := \;\; \langle \mathcal{T}\hat{S}_l^z(t^+)\hat{S}_p^+(t)\hat{S}_q^-(0)\rangle - \langle \hat{S}_l^z\rangle iG_{pq}(t). \tag{2.132}$$

According to the definition of the Vxc, we have:

$$V^{\rm xc}_{pp,qq}(t)iG_{pq}(t) = -J\Big[\Lambda_{p\bar{p}q}(t) - \Lambda_{\bar{p}pq}(t)\Big]. \tag{2.133}$$

where for simplicity, we write $\bar{p} = p + \delta$ as the neighboring sites of p and drop the summation symbol $\sum_\delta$. Using the fact that for local spins, $\hat{S}_p^z = \hat{S}_p^+\hat{S}_p^- - \frac{1}{2}$, we rewrite the vertex function as

$$\Lambda_{lpq}(t) \;\; = \;\; \langle \mathcal{T}\hat{S}_l^+(t^+)\hat{S}_l^-(t^+)\hat{S}_p^+(t)\hat{S}_q^-(0)\rangle - [\frac{1}{2} + \langle \hat{S}_l^z(t^+)\rangle]iG_{pq}(t) \tag{2.134}$$

and approximate the correlation with four spin operators as

$$\begin{aligned} & \langle \mathcal{T}\hat{S}_l^+(t^+)\hat{S}_l^-(t^+)\hat{S}_p^+(t)\hat{S}_q^-(0)\rangle \\ \approx \;\; & \langle \hat{S}_l^+(t^+)\hat{S}_l^-(t^+)\rangle\langle \mathcal{T}\hat{S}_p^+(t)\hat{S}_q^-(0)\rangle \\ & + \langle \hat{S}_p^+(t^+)\hat{S}_l^-(t^+)\rangle\langle \mathcal{T}\hat{S}_l^+(t)\hat{S}_q^-(0)\rangle, \end{aligned} \tag{2.135}$$

which is a factorization with an exchange of the site indices.

We call such approximation the exchange term of the vertex function, which is labeled as $\Lambda^{\rm x}$:

$$\Lambda^{\rm x}_{lpq}(t) \;\; := \;\; -G_{pl}(0^+)G_{lq}(t). \tag{2.136}$$

The derivation above is not restricted to the dimensionality of the model or the sign of the exchange coupling. Next we consider specifically a one-dimensional

antiferromagnetic Heisenberg lattice. We note that $\langle \hat{S}^z_p \rangle = 0$, and thus the exchange part of the interaction term takes the explicit form

$$\begin{aligned} F^{\mathrm{x}}_{pq}(t) &= -J\Big[\Lambda^{\mathrm{x}}_{p\bar{p}q}(t) - \Lambda^{\mathrm{x}}_{\bar{p}pq}(t)\Big] \\ &= -J\Big[G_{p,p+1}(0^+)G_{p+1,q}(t) + G_{p,p-1}(0^+)G_{p-1,q}(t) \\ &\quad -G_{p+1,p}(0^+)G_{pq}(t) - G_{p-1,p}(0^+)G_{pq}(t)\Big]. \end{aligned} \tag{2.137}$$

This reads in the momentum domain as

$$\begin{aligned} F^{\mathrm{x}}(k,t) &= \frac{-J}{N}\sum_{k'} G(k',0^+)G(k,t)\Big[e^{-ik'}e^{ik} + e^{ik'}e^{-ik} - e^{ik'} - e^{-ik}\Big] \\ &= \frac{-2J}{N}\sum_{k'} G(k',0^+)G(k,t)\Big[\cos(k-k') - \cos(k')\Big] \\ &= \frac{-4J}{N}\sum_{k'} iG(k',0^+)iG(k,t)\sin\frac{k}{2}\sin(\frac{k}{2}-k'). \end{aligned} \tag{2.138}$$

One can notice that the exchange part of the Vxc is time-independent:

$$\begin{aligned} V^{\mathrm{s}}(k) &:= \frac{F^{\mathrm{x}}(k,t)}{iG(k,t)} \\ &= \frac{-4J}{N}\sum_{k'} iG(k',0^+)\sin\frac{k}{2}\sin(\frac{k}{2}-k'), \end{aligned} \tag{2.139}$$

which is of even parity for $k \in [-\pi,\pi]$, and with $iG(k,0^+) = \langle S^+_k S^-_{-k}\rangle$ the ground state correlation.

We want to obtain a reference Vxc with F^{x}. Therefore, we do not calculate the analytic form of $iG(k,0^+)$ via the Bethe Ansatz, but use the symmetry of $iG(k,0^+)$ to get an approximate result. We write $iG(k,0^+)$ as an expansion of even order polynomials

$$iG(k,0^+) = \sum_{\xi=0} g_\xi k^{2\xi}. \tag{2.140}$$

For the infinite lattice, the finite sum can be replaced with an integral:

$$\frac{1}{N}\sum_{k'} iG(k',0^+)\sin(\frac{k}{2}-k') \to \frac{1}{2\pi}\sum_{\xi} g_\xi \int_{-\pi}^{\pi} dk'(k')^{2\xi}\sin(\frac{k}{2}-k'). \tag{2.141}$$

In turn, the integral

$$I_\xi(k) := \int_{-\pi}^{\pi} dk'(k')^{2\xi}\sin(\frac{k}{2}-k') \tag{2.142}$$

can be written as $\sin(\frac{k}{2})$ multiplied with a factor only depending on ξ. Absorbing all the $k-$independent factors in the expansion coefficient g_ξ, we get

$$\boxed{V^{\rm s}(k) = -J\sin^2\frac{k}{2}[\frac{1}{\pi}\sum_\xi g_\xi].} \tag{2.143}$$

4 Anderson model at low temperatures within the dynamical exchange-correlation field formalism

In this section, we apply the dynamical xc field formalism to the single-impurity Anderson model (SIAM) [56] at finite temperatures. Our purpose is to provide some analytic insights into the dynamical xc potential (referred to as Vxc) of a system with hybridization effect and thermal fluctuations. Some equations in this section will be related to the numerical results in chapter 4.

We first extend the Vxc formalism to finite-temperature systems where the number of electrons is conserved. Compared with the zero-temperature case, the Green's function is defined with thermal ensemble averages [88]:

$$i\bar{G}(rt,r't';\beta) := \langle\langle\hat{\psi}(rt);\hat{\psi}^\dagger(r't')\rangle\rangle = {\rm Tr}\{\hat{\rho}_G\mathcal{T}[\hat{\psi}(rt)\hat{\psi}^\dagger(r't')]\}. \tag{2.144}$$

Here, the $\langle\langle..\rangle\rangle$ symbol denotes the thermal ensemble average of the time-ordered operators, $\hat{\rho}_G = Z^{-1}e^{-\beta\hat{H}}$ the statistical operator, $\beta = 1/T$ the reverse temperature, and $Z = {\rm Tr}[e^{-\beta\hat{H}}]$ the canonical partition function. The equation of motion of this finite-temperature Green's function can be written with the finite-temperature Vxc, which has the same form as the $T = 0$ case, except that all ground-state expectation values are replaced by thermal averages. The Vxc can still be interpreted as the Coulomb potential of the dynamical xc hole $\rho^{\rm xc}$. The sum rule and the exact constraint fulfilled by $\rho^{\rm xc}$ also take the same form (see Eqs. (2.35) and (2.36)).

Next, we consider the SIAM. The Hamiltonian can be written as

$$\hat{H}_{SIAM} = \epsilon_f(\hat{n}_{f\uparrow}+\hat{n}_{f\downarrow})+U\hat{n}_{f\uparrow}\hat{n}_{f\downarrow}+\sum_{k\sigma}\Big[\epsilon_k\hat{c}^\dagger_{k\sigma}\hat{c}_{k\sigma}+(v_k\hat{f}^\dagger_\sigma\hat{c}_{k\sigma}+{\rm H.c.})\Big]. \tag{2.145}$$

Here $\hat{f}^\dagger_\sigma$ ($\hat{f}_\sigma$) creates (annihilates) an electron with spin σ on the impurity site, $\hat{n}_\sigma = \hat{f}^\dagger_\sigma\hat{f}_\sigma$ is the corresponding number operator, $\hat{c}^\dagger_{k\sigma}$ ($\hat{c}_{k\sigma}$) creates (annihilates) a bath electron with energy ϵ_k. v_k is the hybridization amplitude between the impurity and the bath modes, and ϵ_f and U are the impurity on-site energy

and Coulomb interaction, respectively. We use a 1D tight-binding system to model the SIAM (see a sketch in Fig. 2.5). The impurity site is coupled to one noninteracting (bath) site with hybridization V, and the hopping strength between the N_c noninteracting sites is t_h. When periodic boundary conditions are used for the noninteracting sites, we have the effective SIAM parameters $\epsilon_k = 2t_h \cos(k)$ and $v_k = \frac{V}{\sqrt{N_c}}$, where $k = \frac{2\pi}{N_c} \times 0, 1, 2, \cdots, N_c - 1$.

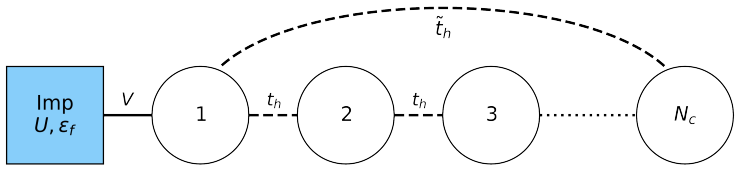

Figure 2.5: A sketch of the 1D tight-binding system used to model an impurity coupled to a continuous bath. When periodic boundary conditions are used for the N_c noninteracting sites ($\tilde{t}_h = t_h$), we have the effective SIAM parameters $\epsilon_k = 2t_h \cos(k)$ and $v_k = \frac{V}{\sqrt{N_c}}$. When $U = 0$, we have the noninteracting case. The dimer case corresponds to $N_c = 1$.

Note that we work at finite temperatures but fix the SIAM at half-filling. For the equilibrium SIAM local Green's function

$$i\bar{G}_{ff,\sigma}(t,\beta) = \langle\langle \hat{f}_\sigma(t); \hat{f}^\dagger_\sigma(0)\rangle\rangle, \tag{2.146}$$

the equation of motion reads

$$\big[i\partial_t - \epsilon_f - V^{\mathrm{H}} - V^{\mathrm{xc}}_\sigma(t,\beta)\big]\bar{G}_{ff,\sigma}(t,\beta) = \delta(t), \tag{2.147}$$

where the Hartree term $V^{\mathrm{H}} = Un_{f\bar{\sigma}} = U\mathrm{Tr}\{\hat{\rho}_G \hat{n}_{f\bar{\sigma}}\}$ is proportional to the density of impurity electron with opposite spin $\bar{\sigma} \neq \sigma$. Moreover, we consider $U + 2\epsilon_f = 0$ and the number of fermionic sites (impurity + bath) $L = N_c + 1$ even in order to have the particle-hole symmetry. Consequently, the thermal average $n_{f\sigma} = 0.5$ and $\epsilon_f + V^{\mathrm{H}} = 0$. Here, we emphasis that similar to the zero-temperature case, the finite-temperature Vxc is the Coulomb potential of the dynamical xc hole. However, for the SIAM, the hybridization between the impurity and the bath should be considered. A dynamical hybridization field, also directly coupled to the Green's function in the equation of motion, can be defined within the Vxc-Framework. We incorporate the hybridization field into the Vxc so that the equation of motion has a simpler form, and with the given Vxc, the Green's function can be directly solved.

Since we choose model parameters to ensure the particle-hole symmetry, we can focus on the Green's function and the Vxc with positive time, namely the particle part. The hole part ($t < 0$) can be obtained using the particle-hole symmetry.

From the equation of motion, the particle part of Vxc can be written as

$$V^{\mathrm{xc}}_{p,\sigma}(t,\beta) = \frac{i\partial_t \bar{G}^{p}_{ff,\sigma}(t,\beta)}{\bar{G}^{p}_{ff,\sigma}(t,\beta)}. \tag{2.148}$$

Here, the particle part Green's function can be expressed with eigenstates of the Hamiltonian as

$$i\bar{G}^{p}_{ff,\sigma}(t,\beta) = \theta(t)\frac{\sum_{mn_+} e^{-\beta E_m} e^{-i(E_{n_+}-E_m)t}\left|\langle n_+|\hat{f}^{\dagger}_{\sigma}|m\rangle\right|^2}{\sum_m e^{-\beta E_m}}, \tag{2.149}$$

where θ is the Heaviside step function, m, n_+ label eigenstates with $L, L+1$ electrons, respectively, and we set L-electron ground-state energy $E_{m=1} = 0$. At low temperatures, the factor $e^{-\beta E_m}$ is negligible except for the lowest two eigenstates $m = 1, 2$. Thus, the Vxc can be expanded to the order of $e^{\beta(E_2-E_1)}$:

$$\boxed{V^{\mathrm{xc}}_{p,\sigma}(t,\beta) = V^{\mathrm{xc}}_{p,\sigma}(t,T=0) + \tilde{V}(t)e^{-\beta(E_2-E_1)},} \tag{2.150}$$

which is the zero temperature $V^{\mathrm{xc}}_{p,\sigma}(t, T = 0)$ plus a correction from a time-oscillating term $\tilde{V}_{p,\sigma}(t)$ and an exponentially small factor.

By now, we have introduced the key equations of the Vxc formalism applied to the symmetric SIAM at low temperatures. The definition of finite-temperature Vxc is a natural extension from the zero-temperature formalism, with ground-state expectation values replaced by thermal ensemble averages. The sum rule and the exact constraint which the dynamical xc hole fulfills take the same form as in the $T = 0$ case. For the SIAM, the Vxc also incorporates the hybridization effect. To calculate the Green's function, however, we must find a good approximation of the Vxc (Eq. (2.150)). This can be achieved by using a noninteracting case ($U = 0$) and a dimer case ($N_c = 1$) as references. From these two reference systems, we propose an ansatz of the SIAM Vxc. In chapter 4, we will interpret the physical meanings of the ansatz parameters using the analytic results from the reference systems, and present the Kondo spectral function calculated using the ansatz.

5 Summary of this chapter

In this chapter, we reviewed several widely used theoretical methods and introduced the approaches developed during this thesis work. In the next two chapters, we apply these methods to low-dimensional magnetic systems and present the numerical results. The purpose of chapters 3 and 4 is to provide

a concise description of the magnetic systems studied in the papers, our theoretical treatments and their corresponding outcomes. For further details, we refer to the actual papers. In chapter 3, we study a frustrated 2D system and a homogeneous 1D system using localized spin models. For the former, the magnon self-energy approach is applied, and for the latter, we calculate the dynamical spin structure factor using the spin dynamical xc potential formalism. In chapter 4, we consider models with localized spin and itinerant electrons. We employ an approach combining MPS and NEGF methods to study the dynamics of quantum skyrmions in presence of electric currents, and investigate the low-temperature Kondo spectral functions from the perspective of the dynamical xc field.

Developing a single theoretical method which is universally suitable for distinct magnetic systems is challenging, due to the various and competing magnetic mechanisms. Therefore, we expect that our diverse frameworks may effectively improve the current theoretical descriptions and provide new insights into the physics of different magnetic systems.

Chapter 3

Pure spin exchange: Frustrated and isotropic Heisenberg system

In this chapter we apply the magnon self-energy approach and the spin Vxc approach to localized spin systems. Local spin models correspond to materials where the unpaired d or f shell electrons are localized in real space. Examples include magnetic insulators and some rare-earth metals where magnetism and conduction originate from different groups of electrons [27, 116]. We use the Heisenberg model [115], which is defined on a discrete lattice with the Hamiltonian:

$$\hat{H} = -\sum_{ij} J_{ij} \hat{\mathbf{S}}_i \cdot \hat{\mathbf{S}}_i \tag{3.1}$$

where i, j are lattice site labels. The exchange interaction strength J is typically short-ranged, meaning J_{ij} is nonzero only between nearest neighbours (NN) and next nearest neighbours (NNN):

$$J_{ij} = \begin{cases} J_1, & \text{NN}, \\ J_2, & \text{NNN}. \end{cases} \tag{3.2}$$

We study a 2D system with J_1-J_2 couplings which may lead to so-called magnetic frustration and a 1D AFM system with only J_1. The results are from Paper I and II. The purpose of this chapter is to present our theoretical developments for localized spin system. We highlight key equations in boxes.

1 Ground state of frustrated 2D Heisenberg clusters via the magnon self-energy approach

Magnetic frustration originates from different and competing magnetic couplings or from specific spin lattice geometries [117, 118, 119]. To study magnetic frustration in a system with quantum fluctuations, the quantum Heisenberg model, which has a simple form and is exactly solvable in 1D, is a suitable testground. When the Heisenberg model is defined on a triangular lattice with $J_1 < 0, J_2 = 0$, the spins in the ground state can align in a way which is neither FM nor AFM, and thus frustrated. Magnetic frustration can also occur when the model is defined on a square lattice, e.g., with $J_1 < 0, J_2 < 0$. The 2D Heisenberg model is generally unsolved, although quantum Monte Carlo and DMRG algorithms perform well on finite clusters. Hence, we develop a Green's function technique, which is beyond Tyablikov's [120] and Kondo's [121] decoupling methods within the random phase approximation (RPA), to investigate the ground-state properties of the 2D Heisenberg model on finite clusters.

In this section, the magnon self-energy approach introduced in chapter 2 is applied to 2D Heisenberg systems with square and hexagonal lattices, and with different types of exchange coupling. Compared with the RPA approach, the magnon self-energy approach includes the response of the self-energy to the probing field, $\delta\Sigma/\delta w^z$. Note that we use some notations in this section differently from that in Paper I to ensure consistent notations through this thesis. To assess the performance of the method, the Green's function results are compared with numerical benchmarks from the ED method.

1.1 2D square-lattice cluster

We begin by examining a 5×5 square lattice with open boundary conditions. We discuss both FM and AFM regimes in few selected subspaces with total spin projection S^z_{total}. In comparison to the FM limit $(25\uparrow, 0\downarrow)$ or the AFM limit $(13\uparrow, 12\downarrow)$, an intermediate value of S^z_{total} shows most clearly the competition of NN and NNN exchange couplings. Therefore, we start the discussion with the subspace $S^z_{\text{total}} = 17/2$ $(21\uparrow, 4\downarrow)$ (our finite system is not fully compensated in this case). We use the parameters $J_1 = 1, J_2 = -0.5$. The results, shown in Fig. 3.1, compare RPA, ED and self-energy results. The color palette is used to represent the expectation value of the z-component spin $\langle S^z_i \rangle$, and the numbers show the z-z spin correlation between lattice sites $\langle S^z_i S^z_j \rangle$.

Compared to the RPA decoupling method, including the self-energy improves

the accuracy for both $\langle S_i^z \rangle$ and $\langle S_i^z S_{\bar{i}}^z \rangle$, where site $\bar{i}$ is the symmetric site of i under space inversion. The reason behind the improvement is that the direct response $\delta G/\delta w^z$, which is treated as a constant (possibly with value 0) in the RPA method, gives a nonzero dynamical contribution to the self-energy. We emphasis that the magnon Hedin equations are the key step forward compared to the bare decoupling. Including higher-order responses $\delta^n G/\delta(w^z)^n$ can in principle improve the accuracy, but at the cost of increased converging difficulties and heavier computational burden.

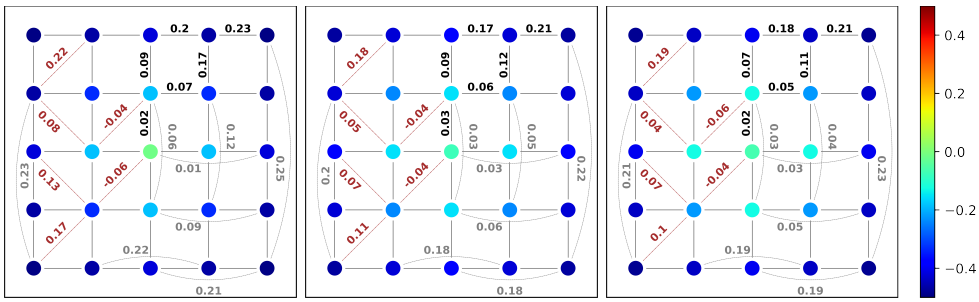

Figure 3.1: Adapted from Paper I. Comparison of $\langle S_i^z \rangle$ (denoted by color) and $\langle S_i^z S_j^z \rangle$ (denoted by numbers) between RPA (left panel), ED (middle panel) and magnon self-energy (right panel) results for a 5×5 lattice with open boundary conditions. The results are for the $S^z_{\text{total}} = 17/2$ subspace, with FM exchange parameters: $J_1 = 1, J_2 = -0.5$. The color coding in the vertical bar applies to all panels.

The self-energy approach shows good accuracy also for $J_1 = -1, J_2 = 0.5$, $S^z_{\text{total}} = 17/2$. Such parameters lead to pure AFM interaction (i.e. no frustration) on the square lattice. In the $S^z_{\text{total}} = 17/2$ subspace, where the majority of the configurations is with spin up, the ground state due to the AFM couplings is relatively homogeneous. This is detailed in Fig. 3.2, where $-0.45 \leq \langle S_i^z \rangle \leq -0.27$ and $\langle S_i^z S_j^z \rangle > 0$ for all lattice sites.

With the same couplings, but for the $S^z_{\text{total}} = 1/2$ subspace, the self-energy method describes well the Neel-type ground state: the distribution of $\langle S_i^z \rangle$ is bipartite, sites on the same/different sublattices are positively/negatively correlated.

Remaining in the $S^z_{\text{total}} = 1/2$ subspace, but with $J_1 = 1, J_2 = -0.5$, we observe that the ground state obtained via the magnon self-energy method exhibits a small total spin value. The magnitudes of $\langle S_i^z \rangle$ are close to zero, and the NN correlations are weak compared to the case with $S^z_{\text{total}} = 1/2, J_1 = -1, J_2 = 0.5$. This behavior is reminiscent of what occurs for systems with an even number of sites, where Lieb's theorem states that $S_{\text{total}} = 0$ in the ground state. In the three cases discussed, the ground states are either relatively homogeneous (the signs of the exchange couplings and the net value of S^z_{total} in the given subspace

are chosen so that they impose conflicting constraints on the spin alignment) or bipartite. This suggests that, for these cases, quantum fluctuations introduced by higher-order response terms have a minor influence in the determination of the Green's function.

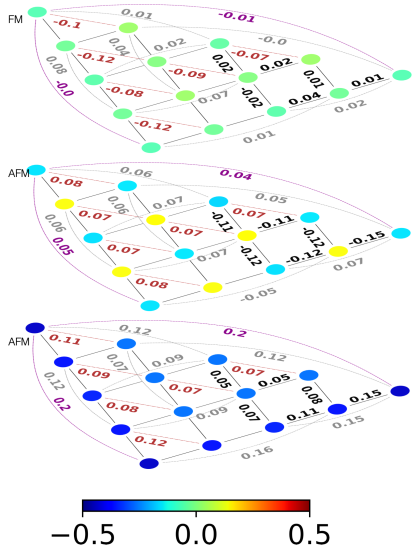

Figure 3.2: Adapted from Paper I. $\langle S_i^z \rangle$ (denoted by color) and $\langle S_i^z S_j^z \rangle$ (denoted by numbers) for a 5×5 square lattice system with open boundary conditions. The color coding in the vertical bar applies to all cases, and results in each panel fulfill the C_{4v} square symmetry. Bottom panel: AFM, $S^z_{\text{total}} = 17/2$; Middle panel: AFM, $S^z_{\text{total}} = 1/2$; Top panel: FM, $S^z_{\text{total}} = 1/2$. The AFM coupling parameters are $J_1 = -1, J_2 = 0.5$ and the FM ones are $J_1 = 1, J_2 = -0.5$.

1.2 Single- and double-impurity configurations

In realistic cases, one often encounters impurities in the system under investigation. Here, we incorporate impurity atoms by introducing an additional term in the Hamiltonian,

$$H_{\text{imp}} = -\sum_{ij} \Delta J_{ij} \hat{\mathbf{S}}_i \cdot \hat{\mathbf{S}}_j. \tag{3.3}$$

where either i or j denote the impurity site(s). We focus on the cases of single and double impurities in a 19-site hexagonal lattice, working within the subspace $S^z_{\text{total}} = 9/2$, which, as for the square lattice illustrate the interplay of FM and AFM couplings. In the no-impurity case, the coupling parameters are $J_1 = 1, J_2 = -0.5$; in the presence of impurities, we have the additional coupling strengths $\Delta J_{ij,NN} = 0.5 J_1, \Delta J_{ij,NNN} = 0.5 J_2$. The magnon self-energy result is shown in Fig. 3.3. It is convenient for the discussion to organize the lattice

sites in shells, where sites in a given shell are equally distant from central site, and different shells correspond to different distances (Fig. 3.3).

For the non-impurity case (Fig. 3.3a), due to the FM NN couplings and the C_{6v} lattice symmetry, the central spin assumes the spin-down $\downarrow$ configuration. With $\langle S_i^z \rangle < 0$ and $\langle S_i^z S_j^z \rangle > 0$ at all sites, we conclude that the non-impurity system is dominated by FM interactions.

Introducing an impurity in the system amplifies both NN and NNN couplings. Locating the impurity at the center (Fig. 3.3b) effectively increases the FM strength around the impurity, which can be seen from the increased correlation between the impurity site and its NN. When the impurity moves away from the cluster center, the C_{6v} symmetry is broken. If the impurity is in shell 1 (Fig. 3.3c), the number of its FM NN sites remains 6, while the number of its AFM NNN sites decreases. Accordingly, the couplings between the impurity and its NN are FM dominated, and thus the spins maintain the $\downarrow$ configuration. However, when the impurity atom moves to the boundary of the lattice (Fig. 3.3d,e), the value of spin-z projection at the impurity, $\langle S_I^z \rangle$, approaches to zero. This change in $\langle S_I^z \rangle$ as the impurity moves from the center towards the cluster boundary (where there are fewer NN and NNN sites), can be ascribed to the finite size effect and the cluster geometry. Finally, we also show results for one geometry with two impurities, where the latter are both located in shell 1 and NN to each other (Fig. 3.3f). In this case, the impurities and their NN spins are strongly FM coupled, and form a small FM sub-cluster.

As an overall remark to this section, the magnon self-energy approach appears to be able to capture all the effects due to the J_1-J_2 competition, also in the presence of significant finite size effects. However, it should also be noted that the type of spin-spin interactions considered in this section are symmetric (i.e, expressed in terms of scalar products between spins). In many materials, the spin-orbit interaction can mediate anti-symmetric exchange couplings among spins. For these systems, the magnon self-energy approach is less successful (we refer to Paper I for more results and discussions). Moreover, although the magnon self-energy approach produces satisfactory ground-state expectation values and spin correlations, its application to dynamical properties is quite limited. We believe that the spin dynamical xc potential formalism performs better in calculating the dynamical structure factor of the Heisenberg model, as shown by the results in the next section.

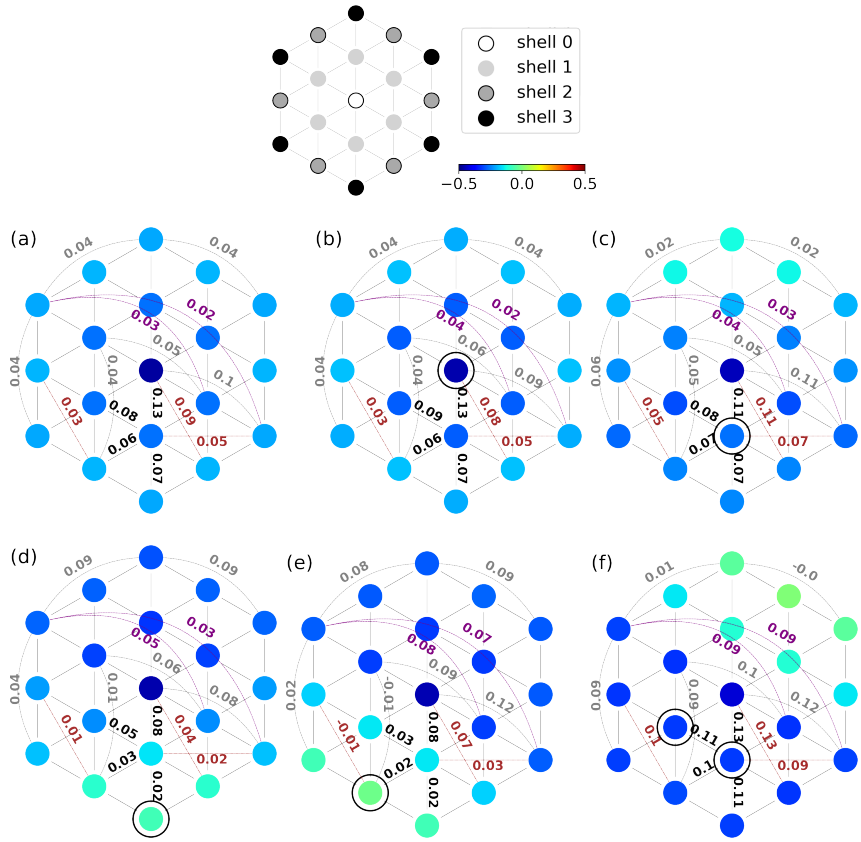

Figure 3.3: Adapted from Paper I. $\langle S_i^z \rangle$ (denoted by color) and $\langle S_i^z S_j^z \rangle$ (denoted by numbers) in an open-boundary 19-site hexagonal lattice system with and without impurity. The non-impurity coupling parameters are $J_1 = 1, J_2 = -0.5$. The additional impurity coupling strengths are $\Delta J_{NN} = 0.5J_1, \Delta J_{NNN} = 0.5J_2$. $S^z_{\text{total}} = 9/2$ $(14 \uparrow 5 \downarrow)$. The top panel illustrates different shells of atoms (see main text). The color coding in the horizontal bar applies to all cases. (a) No impurity case. (b)-(f) The circles with a black outline are impurity sites.

2 Spin dynamical structure factor of the 1D spin-1/2 AFM Heisenberg lattice via the spin Vxc approach

As mentioned in chapter 1, the spin dynamical structure factor,

$$S^{\alpha\beta}(\mathbf{k},\omega) = \frac{1}{N}\int e^{i\omega t}\sum_{pq} e^{-i\mathbf{k}\cdot(\mathbf{r}_p-\mathbf{r}_q)}\langle \hat{S}_p^{\alpha}(t)\hat{S}_q^{\beta}\rangle \tag{3.4}$$

can be seen as the Fourier transform of the spin Green's function $G^{\alpha\beta}(t)$ (Eq. (2.62)). Here, we present the results of the spin xc field scheme, which has been derived in chapter 2, on the 1D AFM spin-1/2 Heisenberg model. The key quantity

in the xc field formalism is the dynamical xc field (henceforth referred to as Vxc). Given the Vxc, the corresponding Green's function can be solved by a time-integral. We will first calculate the exact Vxc on small clusters. Based on the features of cluster Vxc, we propose an ansatz for the infinite lattice Vxc, with which $G^{+-}(t)$ and thus $S^{+-}(\mathbf{k},\omega)$ can be obtained. Finally, we compare the ground-state energy of the 1D AFM Heisenberg model with that calculated from the half-filled 1D Hubbard model [122, 123, 124] and show that, the xc field formalism accounts a clear and transparent way for the well-known equivalence between the two models in the large interaction limit. In this section, we keep the spin flipping indices implicit: $G = G^{+-}$. Also, since the AFM ground state is symmetric over spin flipping, we always consider positive time $t > 0$ unless otherwise stated.

2.1 The exact spin Vxc of small clusters

As shown in chapter 2, for the homogeneous Heisenberg lattice, the low-order term of the dynamical Vxc in momentum domain is independent of time. To make use of this property, we consider a) periodic boundary conditions where the Bloch basis can be used; or b) open end boundary conditions with a basis similar to the bonding/anti-bonding basis for a dimer (transformed from the orbital site basis with a real symmetric transformation matrix M). For the latter (namely the bonding basis), an analogy can be established to the Bloch basis for periodic cases (see details in Paper II).

We start from a four-site chain. Our aim is to obtain a compact analytic solution to illustrate several features of the Vxc which are present also in larger clusters. Here, we do not repeat the algebra which can be found in Paper II. Instead, we list several equations which are necessary to understand the results. For $t > 0$, the equation of motion of the Green's function reads

$$[i\partial_t - V^{\rm xc}_{\mu\mu,\mu\mu}]G_{\mu\mu}(t) - \sum_{\gamma\neq\mu} V^{\rm xc}_{\mu\gamma,\gamma\mu}(t)G_{\gamma\gamma}(t) - \sum_{\gamma\neq\delta} V^{\rm xc}_{\mu\gamma,\delta\mu}(t)G_{\gamma\delta}(t) = 0. \quad (3.5)$$

Here, Greek subscripts μ,ν,γ,δ are the bonding basis labels taking values from the four states A, B, C, D. The Green's function $G_{\mu\mu}$ maps to $G(k)$ for the periodic case. As shown in Fig. 3.4, the real part of the four-site Vxc oscillates periodically in time. Moreover, with high-energy excitation ignored, the Vxc can be written as

$$\begin{aligned} V^{\rm xc}_{BB,BB}(t>0) &\propto -J \\ V^{\rm xc}_{BC,CB}(t>0) &\propto -J\exp[\frac{iJt}{\sqrt{2}}], \end{aligned} \quad (3.6)$$

whereas $V^{\rm xc}_{BD,DB}(t>0)\approx 0, V^{\rm xc}_{BA,AB}(t>0)\approx 0$. Consequently, $V^{\rm xc}_{BB,BB}$ simplifies to a constant whereas $V^{\rm xc}_{BC,CB}$ oscillates with a single frequency and a constant magnitude, and all other components are negligible.

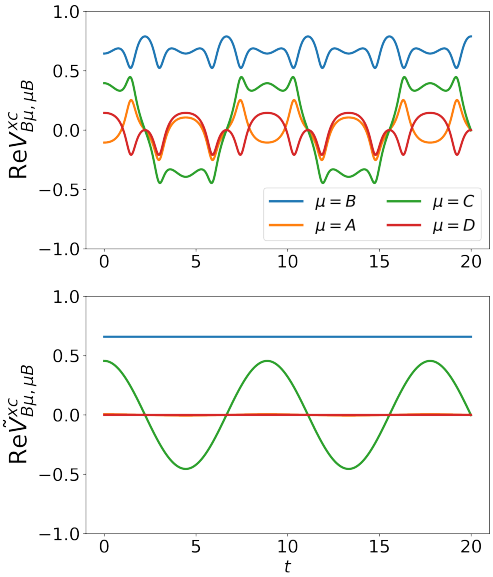

Figure 3.4: Adapted from Paper II. Real part of Vxc of four-site spin-$\frac{1}{2}$ AFM Heisenberg chain, in the unit of $|J|$. Top: exact result. Bottom: only low-energy excitation considered.

Next, we perform ED calculations on eight- and twelve-site rings. The equation of motion of the Green's function can be written in the Bloch basis

$$i\partial_t G(k,t>0)=\sum_{k'} V^{\rm xc}(k-k',t>0)G(k',t>0). \tag{3.7}$$

Here, we consider two facts: i) The spin Vxc contains a static part as shown in chapter 2; ii) The elementary excitation in the 1D AFM system are related to the two-spinon excitation process [125]: for a given k, only ω in the range $\left[(-J)\frac{\pi}{2}|\sin k|, (-J)\pi|\sin\frac{k}{2}|\right]$ gives nonzero dynamical structure factor $S(k,\omega)$. Accordingly, we separate the Vxc into a k-dependent static part and a dynamical part,

$$\sum_{k'} V^{\rm xc}(k-k',t)G(k',t)=V^{\rm s}(k)G(k,t)+Z^{\rm sp}(k,t)G(k,t), \tag{3.8}$$

with which the Green's function can be written as

$$G(k,t)=G(k,0^+)e^{-iV^{\rm s}(k)t}e^{-i\int_0^t Z^{\rm sp}(k,t')dt}. \tag{3.9}$$

In this expression, the k-dependent static term V^{s} determines the main peak of the dynamical structure factor $S(k,\omega)$, and the dynamical term $Z^{\mathrm{sp}}(k,t)$ produces the satellite structure. The separation of the Vxc is in principal arbitrary, thus we choose

$$V^{\mathrm{s}} = (-J)\pi|\sin k|/2, \tag{3.10}$$

such that we have a reference solution (with $Z^{\mathrm{sp}}(k,t)$ set to zero) containing the lower boundary of the two-spinon energy dispersion [125]

$$G^{\mathrm{ref}}(k,\omega) = \frac{-i}{\omega - (-J)\pi|\sin k|/2}. \tag{3.11}$$

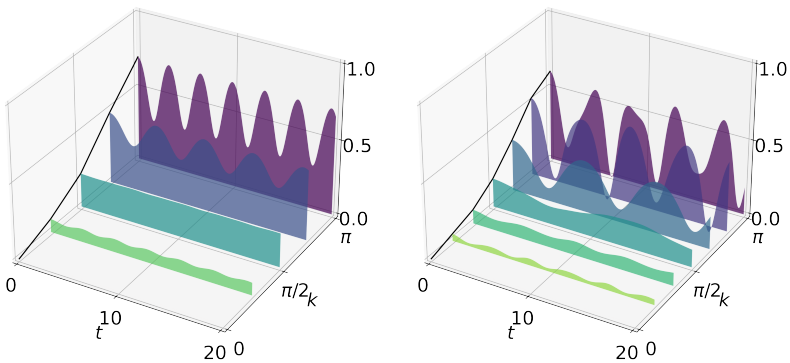

Figure 3.5: Adapted from Paper II. Real part of Z^{sp} from a spin-$\frac{1}{2}$ AFM Heisenberg ring. Left (right) panel: results for a ring with 8 (12) sites.

The dynamical part $Z^{\mathrm{sp}}(k,t)$ contains the information determining the details of the dynamical structure factor, including the position of the satellite peaks and the relative weight between the satellite peak and the main peak. We show $\mathrm{Re}Z^{\mathrm{sp}}(k,t)$ calculated from eight- and twelve-site rings in Fig. 3.5. For each k, $\mathrm{Re}Z^{\mathrm{sp}}(k,t)$ oscillates in time, and the oscillation is nearly periodic which can be described by a cosine function. This behavior, similar to that of the four-site case, can be understood as due to a single quasiparticle-like main excitation.

2.2 Determining the dynamical structure factor with an ansatz for the Vxc

Building on the results in last section, we propose the following ansatz for Z^{sp} in the infinite-chain case:

$$\boxed{Z^{\mathrm{sp}}(k,t) = \mathcal{A}(k)e^{-i\omega^{\mathrm{sp}}(k)t} + \mathcal{B}(k),} \tag{3.12}$$

where the amplitude $\mathcal{A}$, the excitation energy $\omega^{\rm sp}$, and the shift term $\mathcal{B}$ all increase monotonically as k increases from 0 to π. We can have an approximate expression of the Green's function

$$\boxed{G(k,\omega) = G(k,0^+)\Big[\frac{1-\frac{\mathcal{A}(k)}{\omega^{\rm sp}(k)}}{\omega-[V^{\rm s}(k)+\mathcal{B}(k)]}+\frac{\frac{\mathcal{A}(k)}{\omega^{\rm sp}(k)}}{\omega-[V^{\rm s}(k)+\mathcal{B}(k)+\omega^{\rm sp}(k)]}\Big].} \tag{3.13}$$

From Eq. (3.13), it can be seen that the main peak position of the dynamical structure factor is given by $V^{\rm s}+\mathcal{B}$. The excitation energy $\omega^{\rm sp}$ transfers weight from the main peak to higher-energy region resulting in satellite peaks at $V^{\rm s}+\mathcal{B}+\omega^{\rm sp}$. The relative weight between the main peak and the satellite is determined by the amplitude term $\mathcal{A}$ and the excitation energy $\omega^{\rm sp}$.

Next, we introduce the extrapolation procedure of the Vxc. The twelve-site cluster ED result provides $Z^{\rm sp}(K,t)$ and $G(K,0^+)$ for $K=\frac{2\pi}{12}\times 0,1,2,\cdots,6$ (we only need to consider $0\le K\le\pi$). For each K, we extract $\mathcal{A}(K)$ as half the difference between the maximum and minimum of ${\rm Re}Z^{\rm sp}(K,t)$. We approximate $\omega^{\rm sp}(K)=2\pi/\bar{T}$, where $\bar{T}$ is the average time difference between neighbouring peaks of ${\rm Re}Z^{\rm sp}(K,t)$. To reduce the gap-opening due to the finite size, we set $\mathcal{B}(\pi)=0.2$ to be comparable with the broadening factor. For other k values, we estimate $\mathcal{A}(k),\mathcal{B}(k)$ and $G(k,0^+)$ by linear interpolation, and estimate the excitation energy by fitting to the two-spinon spectrum boundary,

$$\omega^{\rm sp}\to(-J)\pi\big[\sin\frac{k}{2}-\frac{1}{2}|\sin k|\big]. \tag{3.14}$$

We show the dynamical structure factor in Fig. 3.6 and compare with a TEBD result with a 100-site chain. Both the peak locations and the relative weights provided by the Vxc approach are qualitatively good. On the other hand, some limitations are present. The main peak frequency $\omega=V^{\rm s}(k)+\mathcal{B}$ is slightly overestimated, compared with the two-spinon spectrum, which we attribute to the finite size effects due to a parameter $\mathcal{B}(\pi)$ originating from a twelve-site cluster. Although the extrapolation procedure is not perfect, we stress that the Vxc approach captures most of the qualitative features of the 1D AFM Heisenberg model with a very low computational load. Moreover, the formalism applies in any dimensions and for any range of interactions. Thus, we expect that the method can be applied in more challenging situations, where e.g. rigorous references like the Bethe ansatz are not available.

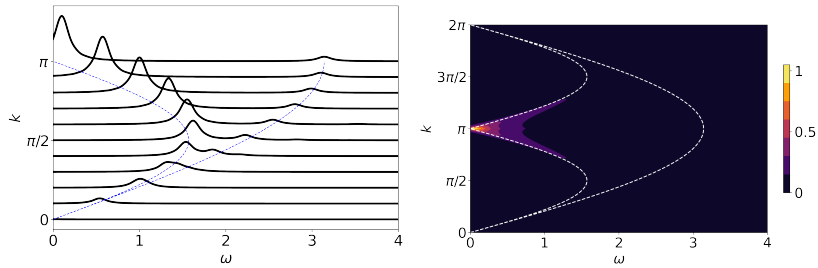

Figure 3.6: Adapted from Paper II. Dynamical structure factor of 1D spin-$\frac{1}{2}$ AFM Heisenberg lattice, with broadening 0.1. Left: calculated with the Vxc approach. The blue dashed curves are the boundaries for two-spinon processes. Right: Calculated with TEBD on a 100-site AFM Heisenberg chain with $J = -1$. The weights are renormalized to be in the range zero to one.

2.3 Comparing the ground state energy of the Heisenberg model and the Hubbard model

It is well known that the 1D spin$-\frac{1}{2}$ AFM Heisenberg model becomes equivalent to the 1D half-filled Hubbard model in the large U regime [126, 27]. Here, we compare the lattice ground state energies for the two models. In the large U limit [27],

$$\lim_{U\to\infty} \frac{E_0^{\mathrm{Hub}}}{N} = \frac{1}{U}(4\frac{E_0^{\mathrm{Heis}}}{N} - 1) \tag{3.15}$$

where E_0^{Hub} is the ground state energy of a N-site Hubbard ring with hopping parameter $t_h = 1$, and E_0^{Heis} is the ground state energy of a N-site AFM Heisenberg ring with $J = -1$. Both energies can be calculated from the corresponding Green's function. To perform a comparison, we compute the ground state energy of the Hubbard lattice in two ways: i) by directly using the electron Vxc at different U values, and ii) by calculating E_0^{Heis} for a $J = -1$ Heisenberg lattice with the spinon Vxc, to be then used in the effective E_0^{Hub} of Eq. (3.15). The differences between the results from these two prescriptions and the exact Bethe ansatz solution are shown in Fig. 3.7. The E_0 results from ED for a six-site ring are also shown as a reference.

We notice that the effective Vxc-based Heisenberg result is rather accurate, with absolute error less than 10^{-4} for $U > 30$: this can be understood as a result of using the two-spinon upper and lower boundaries in the extrapolation, and adjusting the $\mathcal{B}$ parameter from the cluster within the zero spin gap picture. In contrast, the Vxc-based Hubbard result is extrapolated without a good reference (see the detailed treatment in Paper II). Thus, the difference with the Bethe ansatz result is larger. It may suggest that the Vxc for the AFM Heisenberg

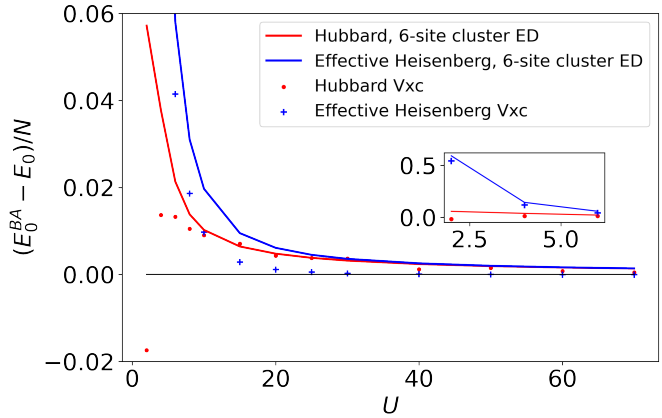

Figure 3.7: Adapted from Paper II. The ground state energies calculated with different methods, with the exact Bethe ansatz result for the 1D Hubbard model, E_0^{BA}, as a reference. The Vxc-based results for the 1D Hubbard model and the 1D AFM Heisenberg model are indicated with red dots and blue crosses, respectively. The ED results for a six-site Hubbard cluster and a six-site Heisenberg cluster are indicated by red and blue curve, respectively. For both models, Vxc is extrapolated from a six-site kernel. For the Heisenberg model results, Eq. (3.15) is used. The inset shows that for $U < 4$, there is an obvious discrepancy between the ground state energy from the two models. For $U > 30$, the results for the two models converge, meaning that the large repulsion limit is reached

model as an effective model with no charge flow is simpler than that for the Hubbard model.

We finally summarize the Vxc approach applied to the 1D AFM Heisenberg lattice. The Vxc formalism produces the dynamical structure factor in favourable agreement with TEBD and with experimental results and captures the equivalence of the Heisenberg model and the Hubbard model in the large U limit. *A single-energy quasiparticle picture* can be used to explain the dynamics of the spin Vxc for the 1D AFM Heisenberg model. Overall, the Vxc formalism provides a good trade-off between accuracy and computation cost in calculating the Green's function. In practice, the extrapolation strategy can affect the accuracy. Therefore, it is important to stress that good-reference constraints such as the two-spinon spectrum for the 1D AFM model, or the sum rule of the spin xc hole, can essentially improve the performance of the Vxc approach.

Chapter 4

Local spins and itinerant electrons: Skyrmions and Kondo systems

The models in chapter 3 are based on the local moment picture, where the interatomic hopping of electrons in unfilled d- or f-shells is neglected; that is, such electrons are essentially treated as localized on the atoms. This is often a reasonable zeroth-order approximation. Yet, in many real materials such as the magnetic transition metals or heavy-fermion systems, f- (and especially d-) electrons actually contribute to electric conduction and are not fully localized. Therefore, to improve the level of description, the itinerant behavior of electrons must be considered. In this chapter, the itinerant character of the electrons is considered as follows: we start from high-level models, such as the Hubbard model, where electrons carrying spin degrees of freedom can move between sites. The Hamiltonian of s- and d-orbital electrons is given by

$$\begin{aligned} H &= -t_s \sum_{<ij>,\sigma} \left[\hat{c}^{\dagger}_{s,i\sigma}\hat{c}_{s,j\sigma} + \text{H.c.}\right] + U_s \sum_i \hat{n}_{s,i\uparrow}\hat{n}_{s,i\downarrow} \\ &\quad -t_d \sum_{<ij>,\sigma} \left[\hat{c}^{\dagger}_{d,i\sigma}\hat{c}_{d,j\sigma} + \text{H.c.}\right] + U_d \sum_i \hat{n}_{d,i\uparrow}\hat{n}_{d,i\downarrow} \\ &\quad t_{s-d} \sum_{i\sigma} \left[\hat{c}^{\dagger}_{d,i\sigma}\hat{c}_{s,i\sigma} + \text{H.c.}\right] + U_{s-d} \sum_{i,\sigma\sigma'} \hat{n}_{s,i\sigma}\hat{n}_{d,i\sigma'}, \end{aligned} \tag{4.1}$$

where $\hat{c}^{\dagger}_{\alpha,i\sigma}$ creates an electron of orbital $\alpha = s, d$ at site i with spin σ. Here, t_α denotes the hopping strength between neighboring sites $< ij >$ and U_α represents the local Coulomb interaction, t_{s-d} is the hybridization strength and

U_{s-d} is the interaction strength between s- and d-electrons. We then make further assumptions: the s-electrons exhibit more itinerant behavior, implying $U_s \sim 0$; the d-electrons are strongly correlated, characterized by a large U_d; and both s- and d-orbitals are half-filled. Under these assumptions, a Schrieffer-Wolff transformation [127] can be applied to project the system into a low-energy subspace (a similar treatment has been applied in Refs. [128, 41])) such that:

- The d-electrons are accounted for via local spin moments.
- The itinerant-electron contribution is only from noninteracting s-electrons.
- The interaction between s- and d-electrons is via the Kondo exchange.

In the following, we employ this *localized spins + itinerant free electrons* modelisation to address very different physical properties in two rather dissimilar systems. Specifically, we consider i) the dynamics of quantum skyrmion textures in the presence of electron currents, and ii) the contribution of thermal fluctuations to the shape of the spectral function of the single impurity Anderson model. For the former situation, we combine the Tensor Networks method and NEGF, and our scope is to study within a novel approach a physical setup which currently is of basic and technological interest. For the second case, we focus on a long-established and well characterised topic (namely, the spectral function of the Anderson model at either zero or finite temperatures), and we provide a novel perspective on the subject, based on a description in terms of the dynamical xc field. We highlight key equations in boxes.

1 Quantum skyrmions on a Kondo lattice

As motivated in chapter 1, skyrmions have attracted significant research interest due their topological properties and potential applications in areas such as data storage and spintronics. Early theoretical treatments of skyrmions are based on models where each atom is regarded as a localized classical spin with a finite magnitude S. When the size of skyrmions is large (hundreds of nanometers) and the spin magnitude is substantial ($S \gtrsim 2$), quantum fluctuations can be neglected, which justifies the classical treatment. However, for skyrmions with sizes on the order of tens of nanometers and a spin magnitude of $S = \frac{1}{2}$ at low temperatures, a quantum treatment is more appropriate. Moreover, the inclusion of itinerant electrons is crucial, as they play an important role in manipulating the skyrmions [40, 41, 42]. Itinerant electrons, which can be tuned by an external bias, interact with the localized spins, influencing the stability,

dynamics, and control of skyrmions. To investigate quantum skyrmions with itinerant electrons at half-filling, we consider the Hamiltonian

$$\hat{H} = \hat{H}^s + \hat{H}^d + \hat{H}^{s-d}, \tag{4.2}$$

with

$$\begin{aligned} \hat{H}^s &= -t_h \sum_{\langle ij\rangle \in L_E;\sigma} \left(\hat{c}^\dagger_{i\sigma}\hat{c}_{j\sigma} + \text{H.c.}\right), \quad \hat{H}^{s-d} = -g\sum_{i\in C} \hat{\mathbf{s}}_i \cdot \hat{\mathbf{S}}_i \\ \hat{H}^d &= \sum_{\langle ij\rangle \in C} \left[\mathbf{D}_{ij}\cdot \hat{\mathbf{S}}_i \times \hat{\mathbf{S}}_j - J_{ij}\hat{\mathbf{S}}_i \cdot \hat{\mathbf{S}}_j\right] - \sum_{i\in C} \mathbf{B}_i \cdot \hat{\mathbf{S}}_i. \end{aligned} \tag{4.3}$$

Here, t_h is the (nearest neighbour) hopping strength of itinerant electrons, $\hat{\mathbf{s}}_i = (1/2)\sum_{\tau\tau'} \hat{c}^\dagger_{i\tau}\boldsymbol{\sigma}_{\tau\tau'}\hat{c}_{i\tau'}$ the spin operator of itinerant electrons with $\boldsymbol{\sigma} \equiv (\sigma^x, \sigma^y, \sigma^z)$ the vector of Pauli matrices, $\mathbf{S}_i$ the local spin operators, g the Kondo exchange strength, and J, $\mathbf{B}$ and D respectively denote the Heisenberg exchange, the external magnetic field, and a Dzyaloshinskii–Moriya interaction (DMI) [129, 130] of Neel type, where $\mathbf{D}$ is perpendicular to the position vector $\mathbf{r}_{ij}$ between sites i and j, and C (L_E) is the 2D region where the local spins (itinerant electrons) reside. We consider three setups (see a sketch in Fig. 4.1a):

1. Both local spins and itinerant electrons are in the same finite lattice $C \equiv L_E$. This will be referred to as the isolated case.

2. Local spins are in region C, and itinerant electrons are in an enlarged finite lattice $L_E = L + C + R$, where region L (R) is coupled to C from the left (right). This will be referred to as the enlarged case.

3. Itinerant electron region enlarged $L_E = L + C + R$, but with semi-infinite L and R regions. This will be referred to as the open case.

The quantum spin-electron system consists of a large number of degrees of freedom. In order to study quantum skyrmions with reasonable size, we make one approximation: we treat $\hat{H}^{s-d}$ at the mean-field level. By defining $\hat{V}^s = \sum_{i\in C}\langle\hat{\mathbf{S}}_i\rangle \cdot \hat{\mathbf{s}}_i$ and $\hat{V}^d = \sum_{i\in C}\langle\hat{\mathbf{s}}_i\rangle \cdot \hat{\mathbf{S}}_i$, the Hamiltonian can be separated into two parts, $\hat{H} \to (\hat{H}^s_{MF}, \hat{H}^d_{MF})$, with

$$\boxed{\hat{H}^{s/d}_{MF} = \hat{H}^{s/d} - g\hat{V}^{s/d}.} \tag{4.4}$$

$\hat{H}^s_{MF}$ and $\hat{H}^d_{MF}$ depend on the expectation values from each other. Therefore, by solving s-part and d-part by different approaches, the whole spin-electron system can be treated in a self-consistent way. We first consider setup 1, namely the

isolated case, and calculate the ground state properties. Starting with $\langle \mathbf{s}_i \rangle = 0$, we use a MPS algorithm from the ITensor library [131, 132] to find the ground state of $\hat{H}^d_{MF}$ and update the averages $\langle \mathbf{S}_i \rangle$. These then enter as parameters when solving via ED for $\hat{H}^s_{MF}$, while reproducing $\langle \mathbf{s}_i \rangle$. As the iterations converge, the mean-field ground state is reached.

1.1 Benchmark calculations: Exact vs mean field Kondo exchange, and quantum vs classical spins

Before presenting the ground state profile for a large cluster, we perform benchmark calculations. To see if a quantum treatment of local spins together with itinerant electrons (albeit within a mean-field account of Kondo exchange) is beneficial, we consider a square plaquette with 4 spins and 4 electrons and, via Eq. (4.2) and the Lanczos method, we determine for reference its full quantum ground state. Then, we move around the plaquette while increasing the number n_{cl} of classical local spins from 0 to 4 (Fig. 4.1c). This results in a mean-field, semiclassical (SC) coupling scheme between local spins and s electrons, and between classical and quantum local spins. To characterize the SC treatment, we use

$$\eta_{n_{cl}} = \frac{1}{N} \sum_{i \in C} \frac{|\langle \hat{\mathbf{S}}_i^{\mathrm{Ex.}} \rangle - \langle \hat{\mathbf{S}}_i^{\mathrm{SC}}(n_{cl}) \rangle|}{|\langle \hat{\mathbf{S}}_i^{\mathrm{Ex.}} \rangle|}, \tag{4.5}$$

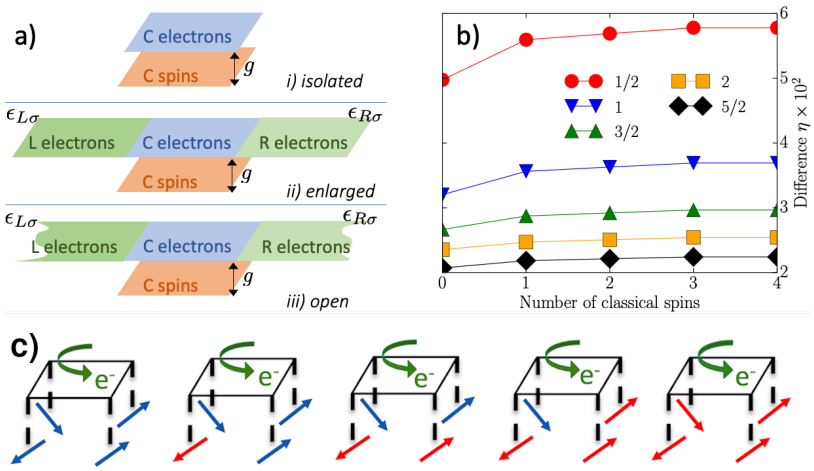

Figure 4.1: Adapted from Paper III. **a)** Sketch of the three setups considered. **b)** Difference between exact and mean-field ground-state expectation values when $D = 0.2$, $J = 0.1$, $B^z = 0.1$, $t_h = 1$, $g = 2$. **c)** The benchmark clusters, from full-quantum to full-classical localized spins.

which depends on the number n_{cl} of local spins treated classically. In Fig. 4.1b, η grows as a function of n_{cl} but gets smaller when the spin value S increases from $\frac{1}{2}$ to $\frac{5}{2}$, a sign that the classical regime is being approached. It can be seen from the benchmark calculation that even with a mean-field treatment of the Kondo exchange, using quantum local spins is beneficial over classical ones when $S = \frac{1}{2}$.

1.2 Ground state of an isolated case

Now we consider the mean-field level ground state of an isolated spin-electron system in a rhombus-shaped 21×21 finite triangular lattice. Besides the spin expectation values $\langle \hat{\mathbf{S}}_i \rangle$ and $\langle \hat{\mathbf{s}}_i \rangle$, we identify the quantum skyrmions with the quantum scalar chirality [38]

$$Q_{\rm sp} = \frac{1}{\pi} \sum_{<ijk>\in C} \langle \hat{\mathbf{S}}_i \cdot [\hat{\mathbf{S}}_j \times \hat{\mathbf{S}}_k] \rangle, \tag{4.6}$$

$$Q_{\rm el} = \frac{1}{\pi} \sum_{<ijk>\in C} \langle \hat{\mathbf{s}}_i \cdot [\hat{\mathbf{s}}_j \times \hat{\mathbf{s}}_k] \rangle, \tag{4.7}$$

where the sum runs over all non overlapping triangles formed by neighboring sites i, j, k. For $S = 1/2$ local spins, $|Q| \sim 1$ signals the presence of a skyrmion.

The ground state profile of such spin+electron system with parameters $D = 0.2, J = 0.1, B^z = 0.1, t_h = 1, g = 2$ is shown in Fig. 4.2a, where the skyrmions exhibit an approximate periodic alignment. Since the local spins are described quantum mechanically, we study the entanglement between spin pairs at sites $i \neq j$ via the concurrence [133, 134, 39] $\mathcal{C}_{ij} = \mathcal{C}[\hat{\rho}_{ij}]$, and where $\hat{\rho}_{ij}$ is the reduced density matrix. As shown in Fig. 4.2a, the concurrence shows a lack of long-range entanglement for the skyrmion (crystal) texture.

To discuss the role of the itinerant electrons, we compare a spin-electron (sp-el) with and a spin-only (sp) system. We define a relative difference

$$\eta' = \frac{1}{N} \sum_{i\in C} \frac{\left| \langle \hat{\mathbf{S}}_i^{\text{sp-el}} \rangle - \langle \hat{\mathbf{S}}_i^{\text{sp}} \rangle \right|}{\left| \langle \hat{\mathbf{S}}_i^{\text{sp}} \rangle \right|}, \tag{4.8}$$

to quantify how much the local spin expectation values will be changed due to the itinerant electrons. For the 21×21 cluster, $\eta'_{21} = 10\%$. Moreover, for an 11×11 rhombus cluster with D=0.2, J=0.15, B^z=0.06, t_h=1, g=2 where both sp-el and sp systems exhibit a single-skyrmion texture, the relative difference

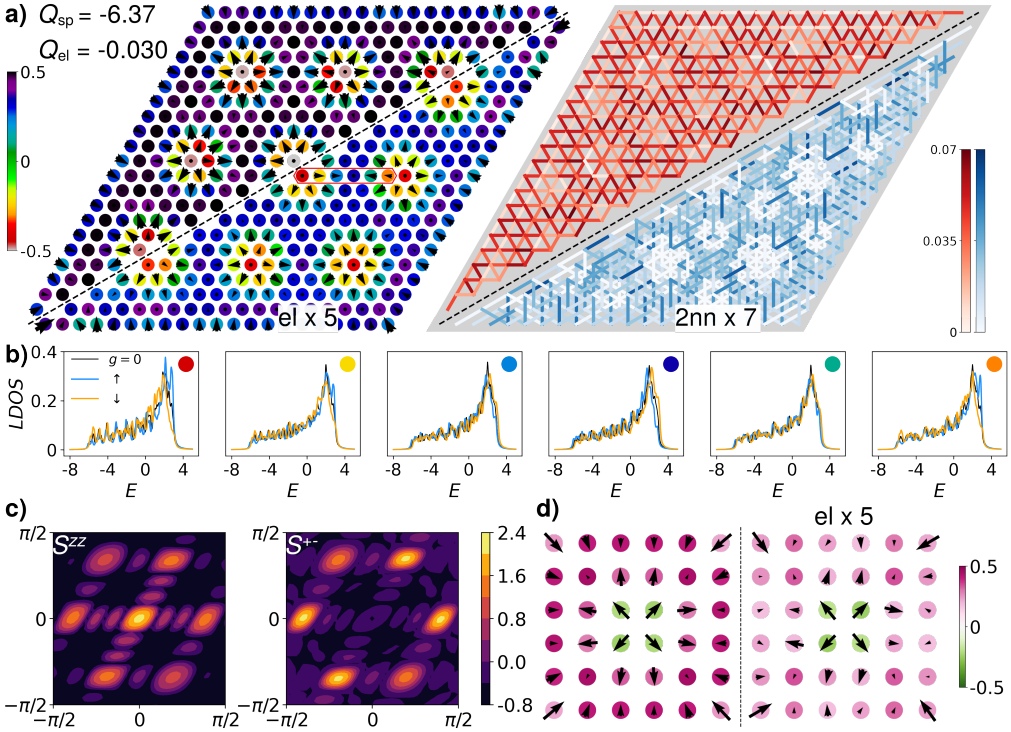

Figure 4.2: Adapted from Paper III. Ground state results for $D = 0.2, J = 0.1, B^z = 0.1, t_h = 1, g = 2$. **a)** Spin expectation-value (left) and concurrences $\mathcal{C}$ (right) heatmaps in a 21×21 isolated rhombus cluster, with localized-spins (itinerant-electrons) chiralities $Q_{sp} = -6.37$ ($Q_{el} = -0.030$). In the spin map, the top (bottom) half shows the expectation value $\langle S^{x,y,z} \rangle$ ($\langle s^{x,y,z} \rangle$) of the localized-spins (the itinerant-electrons). The values of the z- and xy spin-components are indicated by colours and arrows, respectively. In the concurrence map, the value of $\mathcal{C}$ for n.n. (upper half) and next nearest neighbour (2nn, lower half) sites is represented by the bond colour. The missing half of each map is recovered using rhombus symmetry. **b)** LDOS for the electrons at the sites marked in the electron spin heatmap in **a)**. In each of the six panels, the spin resolved LDOS is shown, together with the reference $g = 0$ result. **c)** Logarithm of the static structure factors $\ln S^{zz}$ (left) and $\ln S^{+-}$ (right) of the localized-spins. **d)** $\langle S^{x,y,z} \rangle$ (left half) and $\langle s^{x,y,z} \rangle$ for a 6×6 square cluster connected to leads.

is $\eta'_{11} = 14\%$. The noticeable difference between sp-el and sp ground states confirms that itinerant electrons markedly affect the quantum nanoskyrmion.

In turn, the s-electrons are affected by the skyrmion texture, as shown by the spin-resolved local density of states (LDOS) in Fig. 4.2b. The LDOS is defined as

$$\mathcal{D}_{i\sigma}(E) = \langle \phi_{i\sigma} | \delta(E - \hat{H}^s_{\mathrm{MF}}) | \phi_{i\sigma} \rangle, \tag{4.9}$$

where $\phi_{i\sigma}$ is the s-electron orbital at site i with spin σ. The colored dots in the six LDOS panels match the colors of the sites in the sequence encircled by the red curve in Fig. 4.2a to indicate the correspondence. We see that, along the chosen direction, the imbalance between $\mathcal{D}_{i\uparrow}$ and $\mathcal{D}_{i\downarrow}$ is maximal at the sites of

the skyrmions core (i.e., site 1), but much smaller away from these points. Also, for site 5 with the smallest $|\langle \hat{\mathbf{s}}_i \rangle|$, $\mathcal{D}_{i\sigma}$ becomes almost independent of σ, and is rather similar to the unperturbed ($g = 0$) LDOS.

Furthermore, the spin structure factor $S^{zz}(\mathbf{k})$ and $S^{+-}(\mathbf{k})$ exhibit sixfold intensity patterns, consistent with neutron scattering results (from e.g. the B20 compound MnSi [34]).

To conclude this subsection, we briefly summarize the ground-state calculation for an isolated case. Our approach captured the skyrmion-crystal-like phase and verified the importance of itinerant electrons. The concurrence between local spin sites indicates a lack of long-range entanglement, which explains why the MPS method can work for this 2D system: according to the area law, the computational resources required by the MPS method are related to the amount of entanglement in the system. For the skyrmion phase, entanglement is relatively short-ranged, making the MPS algorithm affordable.

1.3 Ground state of an open case

We obtain the ground state (see the spin expectation values in Fig. 4.2d) of a 6×6 open square cluster as follows. Starting with the mean-field level ground state of the isolated region C, the tunneling matrix elements between C and the leads R, L are switched on in time adiabatically between 0 and t_h with a function

$$s_{T_{\rm sw}}(t) = 1 - \theta(T_{\rm sw} - t) \cos^2 \Big(\frac{\pi t}{2T_{\rm sw}} \Big), \tag{4.10}$$

where θ is the Heaviside step function and $T_{\rm sw}$ is the time when the switch-on is finished. Starting from $t = 0$, the quantum local spins are evolved with time-evolution block-decimation (TEBD). The evolution of the s-electrons in presence of leads is solved with the one-particle NEGF method using the embedding self-energy technique, as introduced in chapter 2. After the switch-on is finished (we choose $T_{\rm sw} = 50$), the time-evolution continues until the central region reaches a steady state, which we define as the ground state of the open system.

With model parameters $D = 1, J = 0.2, B^z = 0.5, t_h = 1, g = 1$, we obtain the open case ground state and compare again with spin-only system. A moderate average influence of the electrons on the spin-texture is exhibited, since $\eta' = 6\%$ in this case. Here, we do not further time-evolve the open case ground state with a bias. The reason is that when the system is time-evolved to reach a steady state, the numerical errors are accumulated by the TEBD method. Further

time-evolution requires more advanced numerical algorithm. We notice the time-dependent variational principle algorithm [135, 136] can be a potential choice.

1.4 Dynamics of an enlarged case

We now discuss the dynamics of the spin-electron system using the enlarged setup. This setup includes a region C consisting of a 4×10 rhombus cluster, and an enlarged electron region $L+C+R$ containing $4 \times (100+10+100)$ sites. Spin-polarized bias can be applied to L and R regions as follows:

$$\hat{H}^s \to \hat{H}^s(t) \equiv \hat{H}^s + \hat{w}_L(t) + \hat{w}_R(t), \tag{4.11}$$

where $\hat{w}_L(t) = \sum_{i\in L} \epsilon_L(t)\hat{c}^\dagger_{i\uparrow}\hat{c}_{i\uparrow}$ and similar for $\hat{w}_R(t)$. The L and R regions are chosen to be much longer than C to delay the reflection of the currents by the boundaries, ensuring that steady, stable currents are established within the time of interest ($t < 125$). We first obtain the ground state with no bias in the electron region. Then, starting from $|\Psi^{\rm el}(0)\rangle$, we introduce for $t > 0$ a bias $\epsilon_L(t) = 0.5[1 - \theta(10-t)\cos^2(\pi t/20)]$ with $\epsilon_R(t) = -\epsilon_L(t)$. Combining TEBD for local spins and ED for s-electrons, we simulate the time-evolution with parameters $D = 0.2, J = 0.05, B^z = 0.06, t_h = 1, g = 2$. In this case, the mean-field level ground state shown in Fig. 4.3a corresponds to a spin texture with multiple meron-like structures. Classical merons have topological charge $|Q| = 1/2$ and are usually found on the material boundaries. To better qualify the existence of individual quantum merons, we consider a modified description of the scalar chirality:

$$Q_i = \frac{1}{\pi} \sum_{<lmn>\in R_i} \langle \hat{\mathbf{S}}_l \cdot [\hat{\mathbf{S}}_m \times \hat{\mathbf{S}}_n] \rangle, \tag{4.12}$$

where the sum in Q is restricted to neighboring site triangles which cover up to the third nearest neighboring sites of i (namely, in region R_i).

In Fig. 4.3b and 4.3c we present four colored semi-hexagonal regions defined by their central sites A, B, A' and B' where the local scalar chirality is calculated. These regions are also referred to as regions A, B, A' and B'. At $t = 0$, the local chiralities are $Q_A = Q_B = -0.164$, consistent with the spatial symmetry of the sp-el system. The values of Q_A and Q_B indicate the nontrivial spin topology in regions A and B, respectively. As a comparison, $Q_{A'} = -0.028$ and $Q_{B'} = -0.016$. In addition, the spin maps (Fig. 4.3a, d) show that sites A and B have negative z-spin components, while all their second and third neighboring sites have positive z-spin components. Accordingly, we regard the ground state

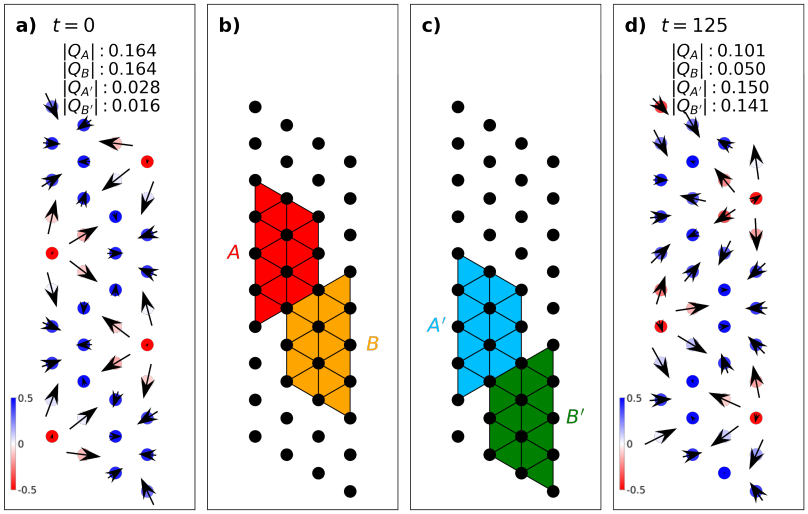

Figure 4.3: Adapted from Paper III. **a), d)** Local spin expectation values $\langle S^{x,y,z}(t)\rangle$ at $t = 0$ and $t = 125$ on a 4×10 C region with an enlarged electron region $L + C + R$ of $4 \times (100 + 10 + 100)$ sites, for parameters $D = 0.2, J = 0.05, B^z = 0.06, t_h = 1, g = 2$. z- and xy-spin components indicated by colors and arrows, respectively. The dynamics is induced by a spin-up polarized bias $\epsilon_L = -\epsilon_R$ in the enlarged region, switched-on at $t = 0$ and ramped to maximum strength 0.5 at $t = 10$. **b), c)** Sketch of four semi-hexagonal regions where the local quantum scalar chirality is calculated. The changes in the values of $Q_{A,B,A',B'}$ and in the spin map indicate the motion of merons.

as with two merons with centers at sites A and B, respectively. At $t = 125$, the local chiralities change to $Q_A = -0.101$ and $Q_B = -0.050$, but $Q_{A'} = -0.150$ and $Q_{B'} = -0.141$, which means the spin texture is driven. $|Q_A|$ ($|Q_B|$) reduces while $|Q_{A'}|$ ($|Q_{B'}|$) increases. Again, site A' (B') has opposite z-component with all its second and third neighboring sites. We can thus conclude that the meron centers are moved from sites A and B to A' and B', respectively. As a conclusive remark, we note that the spin alignment in regions A' and B' at $t = 125$ is not merely a translational shift from the spin alignment in regions A and B at $t = 0$, and $Q_{A'}(t = 125) \neq Q_A(t = 0)$. This is because the merons, due to their small sizes, can be significantly affected by nonequilibrium quantum fluctuations during the time-evolution. Similarly, the non-negligible value of $Q_A = -0.101$ at $t = 125$ is not necessarily indicative of the presence of meron at A. In fact, looking at the spins configuration, such value appears to result from a rather complex interplay of the adjacent spins, and in particular from the change of magnitude and/or sign of the spins close-to or at-the interface between the C and R regions.

It can be instructive to also look at the time-evolution of selected spin-up bond currents $I_{\langle ij\rangle} = -2t_h \mathrm{Im}\langle \hat{c}^\dagger_{j\uparrow} c_{i\uparrow}\rangle$, in Fig. 4.4a, and time snapshots of the spin expectation values $\langle S^{x,y,z}(t)\rangle$ in Fig. 4.4b. After the transient regime ($t \lesssim 10$), the currents at/near the edges ($I_{AF,AE,AB}$) remain relatively stable till $t \approx 80$;

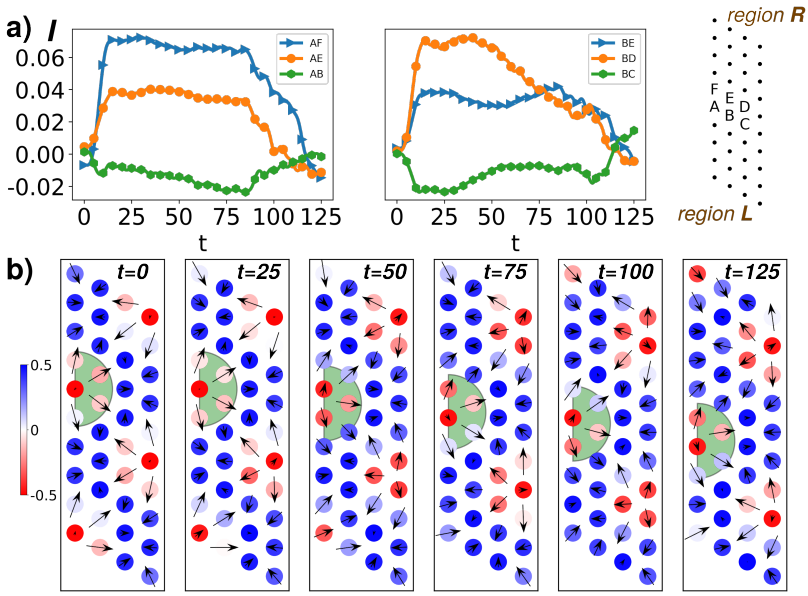

Figure 4.4: Adapted from Paper III. Nonequilibrium dynamics of a rhombus cluster C of 4×10 sites with an enlarged electron region $L + C + R$ of $4 \times (100 + 10 + 100)$ sites, for parameters $D = 0.2$, $J = 0.05$, $B^z = 0.06$, $t_h = 1$, $g = 2$. The dynamics is induced by a spin-up polarized bias $\epsilon_L = -\epsilon_R$ in the enlarged region, switched-on at $t = 0$ and ramped to maximum strength 0.5 at $t = 10$. **a)** Spin-up current $I_{\langle ij \rangle}$ along the bonds $\langle ij \rangle$ labeled by A-F (sketch on the right). **b)** Time snapshots of the spin expectation values $\langle S^{x,y,z}(t) \rangle$ in C, z- and xy-spin components indicated by colours and arrows, respectively. The current-driven motion of one meron is highlighted by the green semicircle.

Beyond this point, they start to be reflected at the outer boundaries of the L, R regions. The merons are driven in a direction opposite (see the shaded area in the time snapshots) to the average flow of the spin-up electrons. We also notice that the merons slightly change their shape in time, which may be due to their small sizes and nonequilibrium quantum fluctuation. The itinerant electrons, in turn, conform their flow to the presence of the moving merons, which results in the observed behavior of the bond spin-up currents.

Lastly, we wish to to provide some general remarks about the dynamics of the spin-electron system as well as about all the other results in this section. The enlarged setup provides a reasonable ground for the simulation of the dynamical behaviors of spin textures. The merons are driven by the spin-polarized current. Again, the itinerant electrons have a significant effect on the motion of the spin textures. Overall, the new MPS + ED/NEGF approach proposed in Paper III is computationally viable to study in- and out-of-equilibrium quantum skyrmions (or merons and other topological magnetic structures as well) with itinerant electrons, with a scope and capabilities beyond those of classical-spin+quantum-electron treatments.

2 The Kondo spectral function of the singe-impurity Anderson model via the Vxc approach

As already mentioned in chapter 1, quantum impurity models have received extended and renewed interest in condensed matter research. Among the quantum impurity models, one of the basic variants, the single-impurity Anderson model (SIAM) [56] is the topic of this section. The SIAM exhibits Kondo physics, and importantly, is used as an auxiliary problem for dynamical mean-field theory (DMFT) [53], which is a tool in first-principles studies of strongly correlated systems in- and out-of equilibrium [137, 54, 55]. To make the first-principles calculations of systems with large size more affordable, we would like to have a theoretical treatment of the SIAM which can capture spectral weights and energy scales of the Kondo peak and the Hubbard bands, and has moderate computational cost.

The dynamical exchange-correlation (xc) field formalism has shown its advantage in calculating the dynamical structure factor of the Heisenberg model (see chapter 3). Using a quasi-particle picture, the spectral weights of the main peak and the satellite structures can well be captured by the static and dynamical parts of the xc field. Hence, we expect that the dynamical xc field formalism can be used to calculate the local spectral function of the SIAM. In chapter 2, we have introduced the general xc field formalism and its application to the symmetric half-filled SIAM at low temperatures. Here, we illustrate how the dynamical xc field can be approximated for the SIAM. The notations, equation of motion, and the tight-binding system used to model the SIAM are the same as in chapter 2. We use a dimer template system ($N_c = 0$, no continuous bath) and a noninteracting case ($U = 0$, only hybridization) to perform analytic calculations, with which we propose an ansatz for the Vxc. The ansatz parameters are determined by comparing to Fermi-liquid theory [48] and finite cluster results. From the ansatz of the Vxc, we calculate the local spectral functions and compare with the numerical renormalization group (NRG) [46] results.

2.1 Dimer case at low temperatures

For the dimer case, the Hamiltonian includes only two parameters U and V. We consider the $T = 0$ case first. In the Kondo regime ($U \gg V$), the particle part of Vxc has an approximate form

$$V^{\mathrm{xc}}_{p,\sigma}(t, T = 0) \approx \omega_p - \lambda\Omega e^{i\Omega t}, \tag{4.13}$$

where $\omega_p = \sqrt{\frac{U^2}{16} + 4V^2} + \sqrt{\frac{U^2}{16} + V^2}$, $\lambda \approx \frac{36V^2}{U^2}$, and $\Omega = \sqrt{\frac{U^2}{4} + 4V^2}$. Eq. (4.13) indicates that the dimer Vxc can be seen as *a sum of a constant term and a quasiparticle-like exponential term*, which is similar to the spin Vxc of the Heisenberg model. Furthermore, the zero-temperature (zero-T) spectral function is

$$\begin{aligned} A_{\text{dimer}}(\omega, T=0) &= \frac{1-\lambda}{2}\delta(\omega+\omega_p) + \frac{\lambda}{2}\delta(\omega+\omega_0) \\ &\quad + \frac{\lambda}{2}\delta(\omega-\omega_0) + \frac{1-\lambda}{2}\delta(\omega-\omega_p). \end{aligned} \tag{4.14}$$

It can be seen from the analytic expression of the dimer Vxc that, for large U, two peaks ($\omega = \pm\omega_p$) of the spectral function are present, which correspond to impurity levels $\epsilon_f, \epsilon_f + U$. The excitation with energy Ω creates two central peaks at $\omega = \pm\omega_0 \approx 0$. However, for the dimer, the spectral weights of the central peaks, $\frac{\lambda}{2} \sim (\frac{V}{U})^2$, vanish as U increases. The lack of Kondo resonance can be naturally understood as the impurity site is coupled to a single site instead of a continuous bath. This is directly reflected by the Vxc: as U increases, the exponential term (with amplitude $\lambda\Omega \sim \frac{V^2}{U}$) becomes negligible.

As shown in chapter 2, the Vxc at low temperatures can be written as its zero-T value plus a temperature-correction (see Eq. (2.150)). For the dimer, that is,

$$\frac{\tilde{V}(t)}{V^{\text{xc}}_{p,\sigma}(t, T=0)} \approx \lambda' e^{i\Omega' t} - \lambda'' e^{i\Omega'' t}, \tag{4.15}$$

where $\lambda', \lambda'' \sim \frac{V^2}{U^2}$, $\Omega' \sim U$ and $\Omega'' \sim \frac{V^2}{U}$ (the full expressions are in the appendix of Paper IV). The Vxc is then

$$V^{\text{xc}}_{p,\sigma}(t, \beta) \approx \omega_p - \lambda\Omega e^{i\Omega t} + e^{-\beta\Delta_0}\omega_p(\lambda' e^{i\Omega' t} - \lambda'' e^{i\Omega'' t}), \tag{4.16}$$

where $\Delta_0 \sim \frac{V^2}{U}$. Note that we require low-temperature condition $e^{-\beta\Delta_0} \ll 1$. The particle part spectral function is

$$\begin{aligned} A_{\text{dimer}}(\omega > 0, \beta) &\cong \frac{1 - \lambda - e^{-\beta\Delta_0}\omega_p(\frac{\lambda''}{\Omega''} - \frac{\lambda'}{\Omega'})}{2}\delta(\omega - \omega_p) + \frac{\lambda}{2}\delta(\omega - \omega_0) \\ &\quad + \frac{e^{-\beta\Delta_0}\omega_p \frac{\lambda''}{\Omega''}}{2}\delta(\omega - \tilde{\omega}_p) - \frac{e^{-\beta\Delta_0}\omega_p \frac{\lambda'}{\Omega'}}{2}\delta(\omega - \tilde{\omega}_0), \end{aligned} \tag{4.17}$$

where $\tilde{\omega}_0 = \omega_p - \Omega'$ and $\tilde{\omega}_p = \omega_p - \Omega''$. The first two terms on the RHS of Eq. (4.17) correspond to the zero-T peaks, while the last two terms, with weights proportional to $e^{-\beta\Delta_0}$, are two small peaks (referred to as thermal peaks in the text below) close to the zero-T peaks, respectively. The mixture of a zero-T peak

and a thermal peak with close frequencies can be seen as a broadening of the zero-T peak. Thus the temperature-induced broadening of the SIAM spectral peaks may be explained in the Vxc picture: *at low-temperatures, thermal fluctuations induce peaks close to the zero-T peaks.* The energy difference between the zero-T peak and the thermal peak effectively leads to a broadening of the spectral peaks at low temperatures.

2.2 Noninteracting case at zero temperature

The contribution of the continuous bath cannot be modeled by the dimer. Hence, we consider a noninteracting case in the limit $N_c \to \infty$ to investigate how the hybridization to the bath affects the Vxc. At zero-T, the impurity Green's function $G_{ff,\sigma}$ can be analytically solved as

$$G^{\text{nonint}}_{ff,\sigma}(\omega) = \frac{1}{\omega - \epsilon_f - \Delta(\omega)}, \tag{4.18}$$

where

$$\Delta(\omega) = \sum_k \frac{|v_k|^2}{\omega^+ - \epsilon_k} \tag{4.19}$$

is the hybridization function [138]. When $|\epsilon_f|, V \ll 2|t_h|$, we approach the so-called wide-band limit (WBL), and the hybridization function can be treated as a constant for $|\omega| \ll 2|t_h|$,

$$\Delta(\omega) = i\Gamma = i\frac{\pi V^2}{4t_h}. \tag{4.20}$$

Accordingly, we can calculate the Vxc (which only contains the hybridization field since $U = 0$):

$$\boxed{V^{\text{xc}}_{\text{nonint,WBL}}(t) = i\Gamma\theta(-t).} \tag{4.21}$$

That is, the Vxc is a purely imaginary constant. The physical picture is as follows: the infinitely wide bath band leads to a broadening of the impurity level ϵ_f, which is represented by a purely imaginary hybridization field. This hybridization effect exists also for non-WBL or interacting cases. Using the evidence gathered from the WBL in the noninteracting case, we assume that, for $U \neq 0$, the SIAM Vxc (with the hybridization effect included) has a complex constant term, whose imaginary part is related to the width of the Hubbard side-band.

2.3 Ansatz of the symmetric SIAM Vxc and the spectral function

Based on the analytic and numerical results above, we propose an ansatz for the particle part Vxc of the symmetric SIAM at low-temperatures (low-T):

$$V^{\rm xc}(t,\beta) = \lambda\omega_p e^{-i\omega_p t} + \mathcal{C}, \tag{4.22}$$

where the parameters are generally temperature-dependent. λ is real, and ω_p and $\mathcal{C}$ are complex. The local Green's function is then approximately (the derivation can be found in the appendix of Paper IV)

$$\boxed{\bar{G}^p_{ff,\sigma}(t,\beta) = -\frac{i}{2}\Big[(1-\lambda)e^{-i\mathcal{C}t} + \lambda e^{-i(\mathcal{C}+\omega_p)t}\Big],} \tag{4.23}$$

and the particle part spectral function is

$$\boxed{\begin{aligned} A(\omega>0,\beta) = \frac{1-\lambda}{2\pi}\frac{\big|{\rm Im}[\mathcal{C}]\big|}{(\omega-{\rm Re}[\mathcal{C}])^2+({\rm Im}[\mathcal{C}])^2} \\ + \frac{\lambda}{2\pi}\frac{\big|{\rm Im}[\mathcal{C}+\omega_p]\big|}{(\omega-{\rm Re}[\mathcal{C}+\omega_p])^2+({\rm Im}[\mathcal{C}+\omega_p])^2}. \end{aligned}} \tag{4.24}$$

Before determining the ansatz parameters numerically, we use the ansatz to interpret the Kondo spectral function. The two peaks in the spectral function can be recognized as a Hubbard side-band located at $\omega = {\rm Re}[\mathcal{C}]$ with broadening ${\rm Im}[\mathcal{C}]$, and a Kondo peak located at $\omega = {\rm Re}[\mathcal{C}+\omega_p]$ with width ${\rm Im}[\mathcal{C}+\omega_p]$. The spectral weights of the two peaks are determined by λ. The two peaks have distinct origins. The peak location and the width of the Hubbard side-band are controlled by the constant term of the Vxc, which accounts for the fact that the impurity level is affected by the interaction and broadened by the continuous bath. On the other hand, at low-T, quasiparticle-like energy ω_p creates a sharp resonance peak close to $\omega = 0$, whose width and height can be described by the Fermi-liquid treatment [48].

Keeping in mind the physical meaning of the parameters, we discuss the extrapolation procedure, which involves calculating the ansatz quantities $(\lambda, \omega_p, \mathcal{C})$ for a given symmetric SIAM with model parameters (U, V, t_h, β). Here, to compare with NRG results in the literature (e.g., from Refs. [139] and [45]), we also apply the WBL. We begin with the $T = 0$ limit, and assume that the first (second) term on the RHS of Eq. (4.24) contributes to the Hubbard (Kondo) peak. In this case, λ can be determined from the height of the Kondo peak:

$$\frac{\lambda}{\pi T_{\rm K}} = \frac{1}{\pi\Gamma}. \tag{4.25}$$

The peak location of the Hubbard side-band can be directly calculated, which means

$$\mathrm{Re}[\mathcal{C}] \approx \frac{U}{2}. \tag{4.26}$$

The Kondo resonance peak is at $\omega = 0$ and its width is given by the Kondo temperature (T_{K}) [45]. Thus,

$$\mathcal{C} + \omega_p \approx -iT_{\mathrm{K}} = -i\sqrt{\frac{U\Gamma}{2}}e^{-\frac{\pi U}{8\Gamma}+\frac{\pi\Gamma}{2U}}. \tag{4.27}$$

The last unknown parameter is the imaginary part of $\mathcal{C}$, which corresponds to the width of the Hubbard side-band. We use the Anderson-type finite-size chain (using open boundary conditions in the tight-bonding model, see Fig. 2.5) spectral function to estimate $\mathrm{Im}[\mathcal{C}]$. Note that a finite chain cannot reproduce the proper broadening caused by an infinitely wide band. However, the relative weight between the Hubbard peak and the Kondo peak,

$$R = \frac{1-\lambda}{2\lambda}\frac{T_k}{\left|\mathrm{Im}[\mathcal{C}]\right|}, \tag{4.28}$$

can provide information of $\mathrm{Im}[\mathcal{C}]$. We extrapolate the value of R by increasing the number of sites in the chain (see Paper IV for more details of the extrapolation procedure).

In Fig. 4.5, we show the local spectral function of a symmetric SIAM in the WBL with $U = 3, t_h = 50, T = 0$. We choose the parameters ($\Gamma = 0.2, 0.5$, and 0.9) to compare with NRG results in the WBL (see Fig. 3 in Ref. [139]). The spectral function shows satisfactory agreements to the NRG results. A complex excitation ω_p dominates the temporal behavior of the Vxc. Specifically, $\mathrm{Re}[\omega_p] = -\frac{U}{2}$ creates the Kondo resonance peak which requires no energy transfer, and $\mathrm{Im}[\omega_p]$ contains the Kondo temperature. At zero-T and in the WBL, most of the ansatz parameters can naturally be determined based on some well-known results of the SIAM. Only one parameter requires a numerical extrapolation. Moreover, the cluster spectral function used in the extrapolation is actually distinct from the SIAM spectral function: for the cluster results, the Kondo peak position is not at $\omega = 0$, and the Hubbard band is too sharp. This discrepancy can be attributed to the essential differences between a finite cluster with tens of sites and a continuous bath. However, the Vxc scheme produces favourable spectral functions using these finite cluster results. This indicates that the Vxc formalism, originating from very fundamental physics and using established knowledge of the target system as a reference, is able to capture the key features of the impurity problem.

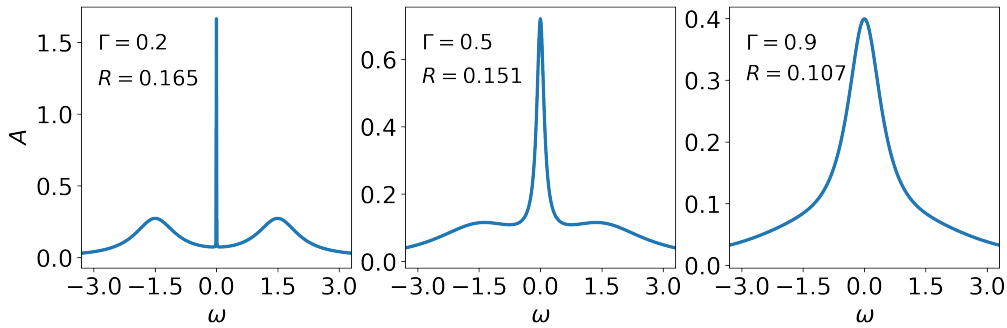

Figure 4.5: Adapted from Paper IV. The zero-T spectral function of a symmetric SIAM. We use $U = 3, t_h = 50$ to approach the WBL, and different V values to realize desired Γ values. From the extrapolation, we get $\mathrm{Im}[\mathcal{C}] = -0.6, -1.3$ and -1.7, respectively, for $\Gamma = 0.2, 0.5$ and 0.9.

Lastly, we discuss the spectral function at low temperatures and below the Kondo temperature. In the Vxc formalism, as observed from the dimer result, thermal excitation leads to the broadening of both the Kondo peak and the Hubbard side-band peak. In the WBL, this thermal broadening can be effectively described by the temperature-dependence of the imaginary part of the excitation energy ω_p, while other parameters remain temperature-independent:

$$\omega_p(T) = \omega_p(T = 0) + i\Omega_T, \tag{4.29}$$

where Ω_T is much smaller than $\mathrm{Im}[\mathcal{C}]$. Effectively, the Hubbard side-band stays almost unchanged with the increasing temperature. We perform ED on an eight-site cluster with $t_h = 500, U = 1$ and $\Gamma = 0.04$ to calculate the spectral function at $T/T_\mathrm{K} = 0.01, 0.1, 1$. The value of Ω_T is estimated using the position of the thermal peak nearest to the Kondo peak. Other parameters are estimated using the zero-T approach. The low-temperature spectral function results are shown in Fig 4.6. Compared with NRG results (see page 3.15 of Ref. [45]), the Vxc result captures the correct trend of the Kondo peak width: at $T \ll T_\mathrm{K}$, the contribution of Ω_T is negligible, leading to a width dominated by the Kondo temperature. As T approaches T_K, $|\Omega_T|$ increases.

3 Summary of this section and the general Vxc formalism

In this section, we presented the result of applying the dynamical xc field formalism to the SIAM at low temperatures. The formalism introduces a dynamical xc field (Vxc), which can be interpreted as the Coulomb potential of the xc hole.

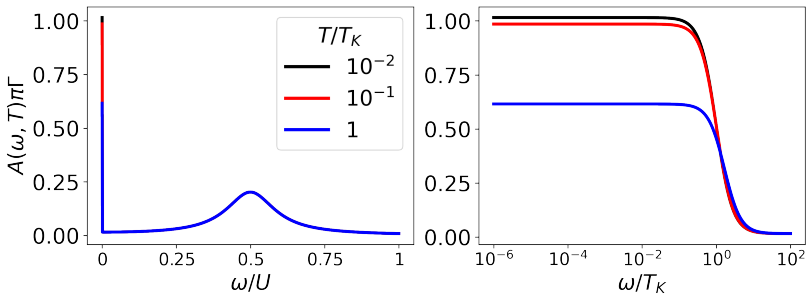

Figure 4.6: Adapted from Paper IV. The spectral function of a symmetric SIAM with $t_h = 500, U = 2$ and $\Gamma = 0.04$, at $T = 0.01T_\mathrm{K}, 0.1T_\mathrm{K}$ and T_K. Left: The frequency is in unit of U. Right: The frequency is in unit of T_K and in logarithmic scale to highlight the width of the Kondo resonance peak.

For the SIAM, the Vxc also incorporates the hybridization effect between the impurity and the bath. We proposed an ansatz for the SIAM Vxc, which includes a complex constant term, $\mathcal{C}$, and a complex quasiparticle-like excitation, ω_p. The real and imaginary parts of $\mathcal{C}$ correspond to the peak location and the width of the Hubbard side-band, respectively. More importantly, $\mathrm{Im}[\omega_p]$ accounts for the Kondo temperature. At zero-T in the WBL, most parameters of the ansatz can be calculated from the model parameters using Fermi-liquid theory. The only unknown parameter can be estimated by an extrapolation procedure. For low temperatures, the temperature-dependence of the ansatz parameters is primarily through $\mathrm{Im}[\omega_p]$, which again needs to be approximated numerically, guided by the insights from the auxiliary analytically dimer Vxc. Overall, the spectral function calculated from the Vxc shows satisfactory agreement with the NRG results. The extrapolation procedures involved are of low computational cost. We understand the favourable performance of the xc field formalism as follows: the screening effect underlying the SIAM is essential for the Kondo effect, and the xc field provides a suitable description for quasiparticle-like excitations. Hence, the parameters in the ansatz have clear physical meaning and can be related in a novel perspective to key well-understood features of the spectral function. The fact that only a few parameters require numerical treatment leads to a good trade-off between accuracy and computational effort.

Finally, we stress a significant feature of the xc field formalism: it manages to reduce a complicated many-body problem to an extrapolation procedure. The extrapolation is usually done with a (numerically) solvable finite cluster or a homogeneous system as a reference. When the target system and the reference system exhibit explicit similarities, the extrapolation can be done straightforwardly (as the Heisenberg model in chapter 3). In practice, the connection between the reference system and the complex target is often less obvious. An example is the SIAM, where the finite cluster spectral function differs qualitat-

ively from the SIAM. Despite this, the xc field formalism successfully captures the implicit correspondence, specifically the relative weight between the Hubbard peak and the Kondo peak at $T = 0$. Hence, we believe that the xc field formalism, based on the quasiparticle picture, is a viable and powerful approach for modeling correlated many-body system and holds great potential for first-principles calculations.

Chapter 5

Summary and outlook

In this thesis, we introduced several newly developed theoretical approaches and presented the results of applying them, in combination with other numerical methods, to low-dimensional magnetic systems. We hope that by listing key equations and highlighting results from the papers, this thesis provides the theoretical background for the papers and serves as a condensed summary of our research outcomes.

In Paper I, we applied the magnon self-energy approach to 2D Heisenberg models. The ground-state properties, including spin expectation values and spin correlations, were calculated in good accuracy using this approach. However, the results were less satisfactory for dynamical properties (such as the spectral functions) and when anti-symmetric spin couplings (e.g. Dzyaloshinskii-Moriya interaction) were included. These systems were then studied using different methods in the following papers.

In Paper II and IV, the spectral functions of a 1D Heisenberg model and the single-impurity Anderson model were calculated using the dynamical exchange-correlation (xc) field formalism. The results showed a good trade-off between accuracy and computational cost. A common feature in these papers is that the xc field can be seen as the sum of a constant term and a quasiparticle-like excitation term, which can be determined from reference systems via analytical theory or numerical extrapolation. Also, by working in real time domain, the formalism avoids the analytical continuation issues.

In Paper III, we proposed a MPS+NEGF/ED framework to study a magnetic skyrmion system involving itinerant electrons. The interaction between local spins and itinerant electrons was described as the Kondo exchange coupling and

was treated at the mean-field level. The results showed that the itinerant electrons significantly affect the local quantum spins. Hence, our approach provides a different scope compared with quantum/classical spin-only and classical-spin + quantum-electron treatments.

Overall, by working with localized spin models and spin+electron models, we expect that our frameworks can improve the treatments to low-dimensional magnetic systems. A long-term goal is to make first-principles calculations more feasible, as mentioned in chapters 1 and 2. Below, we conclude this thesis by proposing several future research directions:

- Investigate impurity models with higher complexity, such as the Kondo lattice or the nonsymmetric SIAM (e.g., not at half-filling or under an external magnetic field). For the Kondo lattice where the Coulomb interaction is not only on a single site, we can study the spatial features of the xc hole and the xc field. For the nonsymmetric SIAM, we want to see how symmetry breaking can be reflected by the xc field.

- Incorporate time-dependent electromagnetic fields. One advantage of the dynamical xc field formalism is its natural extension to nonequilibrium systems. The sum rule and the exact constraint fulfilled by the dynamic xc hole take the same form as in the equilibrium case. Additionally, the NEGF can be directly calculated from the nonequilibrium xc field, without using contour notations. In practice, however, the xc field may have a more complicated form. We should start with systems where exact benchmarks are available and compare our results with conventional NEGF methods.

- Include bosonic contributions using models such as the Hubbard-Holstein model and the Jaynes-Cummings model. The system will then be described by both fermionic and bosonic Green's functions. We are interested in developing a scheme for such mixed-type Green's functions. Furthermore, we can explore a quantum skyrmion system which interacts with photons. Recent literature on light-induced skyrmions [41] and quantum skyrmion operators [140] has provided preliminary valuable insights in this respect.

1 References

[1] J. M. D. Coey. Magnetism and Magnetic Materials. Cambridge Univ. Press, 2010.

[2] C. Gong, L. Li, Z. Li, et al. Discovery of intrinsic ferromagnetism in two-dimensional van der Waals crystals. Nature, 546:265–269, 2017.

[3] B. Huang, G. Clark, E. Navarro-Moratalla, et al. Layer-dependent ferromagnetism in a van der Waals crystal down to the monolayer limit. Nature, 546:270–273, 2017.

[4] E. Dagotto. Correlated electrons in high-temperature superconductors. Rev. Mod. Phys., 66:763–840, Jul 1994.

[5] U. Schollwöck, J. Richter, D. J. J. Farnell, and R. F. Bishop. Quantum Magnetism. Springer Berlin, Heidelberg, 2004.

[6] N. D. Mermin and H. Wagner. Absence of Ferromagnetism or Antiferromagnetism in One- or Two-Dimensional Isotropic Heisenberg Models. Phys. Rev. Lett., 17:1133–1136, Nov 1966.

[7] J. H. Van Vleck. Quantum mechanics-The key to understanding magnetism. Rev. Mod. Phys., 50:181–189, Apr 1978.

[8] R. O. Jones and O. Gunnarsson. The density functional formalism, its applications and prospects. Rev. Mod. Phys., 61:689–746, Jul 1989.

[9] R. O. Jones. Density functional theory: Its origins, rise to prominence, and future. Rev. Mod. Phys., 87:897–923, Aug 2015.

[10] S. Kirchner, S. Paschen, Q.-Y. Chen, S. Wirth, D.-L. Feng, J. D. Thompson, and Q.-M. Si. Colloquium: Heavy-electron quantum criticality and single-particle spectroscopy. Rev. Mod. Phys., 92:011002, Mar 2020.

[11] P. Hohenberg and W. Kohn. Inhomogeneous Electron Gas. Phys. Rev., 136:B864–B871, Nov 1964.

[12] W. Kohn and L. J. Sham. Self-Consistent Equations Including Exchange and Correlation Effects. Phys. Rev., 140:A1133–A1138, Nov 1965.

[13] O. Gunnarsson and B. I. Lundqvist. Exchange and correlation in atoms, molecules, and solids by the spin-density-functional formalism. Phys. Rev. B, 13:4274–4298, May 1976.

[14] V. I. Anisimov, F. Aryasetiawan, and A. I. Lichtenstein. First-principles calculations of the electronic structure and spectra of strongly correlated systems: the lda+ u method. J. Phys.: Condens. Matter, 9(4):767, jan 1997.

[15] U. von Barth and L. Hedin. A local exchange-correlation potential for the spin polarized case. i. J. Phys. C: Solid State Phys., 5(13):1629, jul 1972.

[16] M.A.L. Marques and E.K.U. Gross. Time-dependent density functional theory. Ann. Rev. of Phys. Chem., 55(Volume 55, 2004):427–455, 2004.

[17] F. Aryasetiawan and O. Gunnarsson. Exchange-correlation kernel in time-dependent density functional theory. Phys. Rev. B, 66:165119, Oct 2002.

[18] C. Verdozzi. Time-dependent density-functional theory and strongly correlated systems: Insight from numerical studies. Phys. Rev. Lett., 101:166401, Oct 2008.

[19] S. Kurth, G. Stefanucci, E. Khosravi, C. Verdozzi, and E. K. U. Gross. Dynamical Coulomb Blockade and the Derivative Discontinuity of Time-Dependent Density Functional Theory. Phys. Rev. Lett., 104:236801, Jun 2010.

[20] E. Runge and E. K. U. Gross. Density-Functional Theory for Time-Dependent Systems. Phys. Rev. Lett., 52:997–1000, Mar 1984.

[21] F. Aryasetiawan. Time-dependent exchange-correlation potential in lieu of self-energy. Phys. Rev. B, 105:075106, Feb 2022.

[22] G. Shirane, S. M. Shapiro, and J. M. Tranquada. Neutron Scattering with a Triple-Axis Spectrometer: Basic Techniques. Cambridge University Press, 2002.

[23] Andrea Damascelli. Probing the Electronic Structure of Complex Systems by ARPES. Physica Scripta, 2004(T109):61, jan 2004.

[24] K.H. Andersen et al. The instrument suite of the European Spallation Source. Nuclear Instruments and Methods in Physics Research Section A: Accelerators, Spectrometers, Detectors and Associated Equipment, 957:163402, 2020.

[25] P. Wölfle. Quasiparticles in condensed matter systems. Rep. Prog. Phys., 81(3):032501, jan 2018.

[26] E. Kaxiras. Atomic and Electronic Structure of Solids. Cambridge University Press, 2003.

[27] W. Nolting and A. Ramakanth. Quantum theory of magnetism. Springer Berlin, Heidelberg, 2009.

[28] C. Friedrich, E. Şaşıoğlu, M. Müller, A. Schindlmayr, and S. Blügel. Spin Excitations in Solids from Many-Body Perturbation Theory, pages 259–301. Springer Berlin Heidelberg, Berlin, Heidelberg, 2014.

[29] L.D. Faddeev and L.A. Takhtajan. What is the spin of a spin wave? Phys. Lett., 85A(6):375–377, 1981.

[30] Wikipedia contributors. Magnetic skyrmion — Wikipedia, the free encyclopedia, 2024. [Online; accessed 10-July-2024].

[31] T. H. R. Skyrme. A unified field theory of mesons and baryons. Nucl. Phys., 31:556–569, 1962.

[32] A. Bogdanov and A. Hubert. Thermodynamically stable magnetic vortex states in magnetic crystals. J. Magn. Magn. Mater., 138(3):255–269, 1994.

[33] U. K. Rößler, A. N. Bogdanov, and C. Pfleiderer. Spontaneous skyrmion ground states in magnetic metals. Nature, 442:797–801, 2006.

[34] S. Mühlbauer, B. Binz, F. Jonietz, C. Pfleiderer, A. Rosch, A. Neubauer, R. Georgii, and P. Böni. Skyrmion lattice in a chiral magnet. Science, 323(5916):915–919, 2009.

[35] X. Z. Yu, Y. Onose, N. Kanazawa, J. H. Park, J. H. Han, Y. Matsui, N. Nagaosa, and Y. Tokura. Real-space observation of a two-dimensional skyrmion crystal. Nature, 465(7300):901–904, 2010.

[36] S. Heinze, K. von Bergmann, M. Menzel, J. Brede, A. Kubetzka, R. Wiesendanger, G. Bihlmayer, and S. Blügel. Spontaneous atomic-scale magnetic skyrmion lattice in two dimensions. Nat. Phys., 7:713, 2011.

[37] V. Lohani, C. Hickey, J. Masell, and A. Rosch. Quantum skyrmions in frustrated ferromagnets. Phys. Rev. X, 9:041063, Dec 2019.

[38] O. M. Sotnikov, V. V. Mazurenko, J. Colbois, F. Mila, M. I. Katsnelson, and E. A. Stepanov. Probing the topology of the quantum analog of a classical skyrmion. Phys. Rev. B, 103:L060404, Feb 2021.

[39] A. Haller, S. Groenendijk, A. Habibi, A. Michels, and T. L. Schmidt. Quantum skyrmion lattices in heisenberg ferromagnets. Phys. Rev. Res., 4:043113, Nov 2022.

[40] E. V. Boström and C. Verdozzi. Steering magnetic skyrmions with currents: A nonequilibrium green's functions approach. Physica Status Solidi (b), 256(7):1800590, 2019.

[41] E. V. Boström, A. Rubio, and C. Verdozzi. Microscopic theory of light-induced ultrafast skyrmion excitation in transition metal films. npj Computational Materials, 8(1):62, 2022.

[42] E. Östberg, E. V. Boström, and C. Verdozzi. Microscopic theory of current-induced skyrmion transport and its application in disordered spin textures. Frontiers in Physics, 11, 2023.

[43] J. Kondo. Resistance Minimum in Dilute Magnetic Alloys. Prog. Theor. Phys., 32(1):37–49, 07 1964.

[44] P. B. Wiegmann and A. M. Tsvelick. Exact solution of the Anderson model: I. J. Phys. C: Solid State Phys., 16(12):2281, apr 1983.

[45] E. Pavarini, E. Koch, A. Lichtenstein, and D. Vollhardt, editors. Dynamical Mean-Field Theory of Correlated Electrons: Modeling and Simulation. Verlag des Forschungszentrum Jülich, 2022.

[46] K. G. Wilson. The renormalization group: Critical phenomena and the Kondo problem. Rev. Mod. Phys., 47:773–840, Oct 1975.

[47] A. C. Hewson. The Kondo Problem to Heavy Fermions. Cambridge Studies in Magnetism. Cambridge University Press, 1993.

[48] P. Nozières. A "fermi-liquid" description of the Kondo problem at low temperatures. J. Low Temp. Phys., 17, 1974.

[49] Y. Meir, N. S. Wingreen, and P. A. Lee. Low-temperature transport through a quantum dot: The anderson model out of equilibrium. Phys. Rev. Lett., 70:2601–2604, Apr 1993.

[50] D. Goldhaber-Gordon, Hadas Shtrikman, D. Mahalu, David Abusch-Magder, U. Meirav, and M. A. Kastner. Kondo effect in a single-electron transistor. Nature, 391:156, 1998.

[51] Sara M. C., Tjerk H. O., and Leo P. K. A tunable kondo effect in quantum dots. Science, 281(5376):540–544, 1998.

[52] P. Samuelsson and C. Verdozzi. Two-particle spin entanglement in magnetic anderson nanoclusters. Phys. Rev. B, 75:132405, Apr 2007.

[53] A. Georges, G. Kotliar, W. Krauth, and M. J. Rozenberg. Dynamical mean-field theory of strongly correlated fermion systems and the limit of infinite dimensions. Rev. Mod. Phys., 68:13–125, Jan 1996.

[54] G. Kotliar, S. Y. Savrasov, K. Haule, V. S. Oudovenko, O. Parcollet, and C. A. Marianetti. Electronic structure calculations with dynamical mean-field theory. Rev. Mod. Phys., 78:865–951, Aug 2006.

[55] H. Aoki, N. Tsuji, M. Eckstein, M. Kollar, T. Oka, and P. Werner. Nonequilibrium dynamical mean-field theory and its applications. Rev. Mod. Phys., 86:779–837, Jun 2014.

[56] P. W. Anderson. Localized Magnetic States in Metals. Phys. Rev., 124:41–53, Oct 1961.

[57] C. Verdozzi. Exact diagonalization studies of strongly correlated clusters, 2005.

[58] E. Pavarini, E. Koch, and P. Coleman (eds.). Many-Body Physics: From Kondo to Hubbard: Modeling and Simulation. Verlag des Forschungszentrum Jülich, 2015.

[59] W. Kohn. Nobel Lecture: Electronic structure of matter—wave functions and density functionals. Rev. Mod. Phys., 71:1253–1266, Oct 1999.

[60] C. Lanczos. An iteration method for the solution of the eigenvalue problem of linear differential and integral operators. J. Res. Nat. Bur. Stand, 49:255, 1950.

[61] A. N. Krylov. On the numerical solution of the equation by which in technical questions frequencies of small oscillations of material systems are determined. Izv. Akad. Nauk SSSR, 7, 1931.

[62] J. I. Cirac, D. Pérez-García, N. Schuch, and F. Verstraete. Matrix product states and projected entangled pair states: Concepts, symmetries, theorems. Rev. Mod. Phys., 93:045003, Dec 2021.

[63] M. C. Bañuls. Tensor Network Algorithms: A Route Map. Ann. Rev. Condens. Matter Phys., 14(1):173–191, 2023.

[64] R. Orús. Tensor networks for complex quantum systems. 1:538–550, 2019.

[65] R. Orús. A practical introduction to tensor networks: Matrix product states and projected entangled pair states. Ann. Phys., 349:117–158, 2014.

[66] S. R. White. Density matrix formulation for quantum renormalization groups. Phys. Rev. Lett., 69:2863–2866, Nov 1992.

[67] S. Östlund and S. Rommer. Thermodynamic Limit of Density Matrix Renormalization. Phys. Rev. Lett., 75:3537–3540, Nov 1995.

[68] J. Dukelsky, M. A. Martín-Delgado, T. Nishino, and G. Sierra. Equivalence of the variational matrix product method and the density matrix renormalization group applied to spin chains. Europhys. Lett., 43(4):457, aug 1998.

[69] U. Schollwöck. The density-matrix renormalization group. Rev. Mod. Phys., 77:259–315, Apr 2005.

[70] U. Schollwöck. The density-matrix renormalization group in the age of matrix product states. Ann. Phys., 326(1):96–192, 2011. January 2011 Special Issue.

[71] J. Eisert, M. Cramer, and M. B. Plenio. Colloquium: Area laws for the entanglement entropy. Rev. Mod. Phys., 82:277–306, Feb 2010.

[72] M. Srednicki. Entropy and area. Phys. Rev. Lett., 71:666–669, Aug 1993.

[73] M. B. Plenio, J. Eisert, J. Dreißig, and M. Cramer. Entropy, Entanglement, and Area: Analytical Results for Harmonic Lattice Systems. Phys. Rev. Lett., 94:060503, Feb 2005.

[74] M. M. Wolf. Violation of the Entropic Area Law for Fermions. Phys. Rev. Lett., 96:010404, Jan 2006.

[75] M. M. Wolf, F. Verstraete, M. B. Hastings, and J. I. Cirac. Area Laws in Quantum Systems: Mutual Information and Correlations. Phys. Rev. Lett., 100:070502, Feb 2008.

[76] M. B. Hastings. An area law for one-dimensional quantum systems. J. Stat. Mech., 2007(08):P08024, aug 2007.

[77] G. Vidal. Efficient simulation of one-dimensional quantum many-body systems. Phys. Rev. Lett., 93:040502, Jul 2004.

[78] D. Poulin, A. Qarry, R. Somma, and F. Verstraete. Quantum Simulation of Time-Dependent Hamiltonians and the Convenient Illusion of Hilbert Space. Phys. Rev. Lett., 106:170501, Apr 2011.

[79] H. F. Trotter. On the product of semi-groups of operators. Proc. Amer. Math. Soc., 10:545–551, 1959.

[80] M. Suzuki. Generalized Trotter's formula and systematic approximants of exponential operators and inner derivations with applications to many-body problems. Comm. Math. Phys., 51:183–190, 1976.

[81] P. Calabrese and J. Cardy. Evolution of entanglement entropy in one-dimensional systems. J. Stat. Mech.: Theor. Exp., 2005(04):P04010, apr 2005.

[82] T. J. Osborne. Efficient approximation of the dynamics of one-dimensional quantum spin systems. Phys. Rev. Lett., 97:157202, Oct 2006.

[83] G. Vidal. Classical Simulation of Infinite-Size Quantum Lattice Systems in One Spatial Dimension. Phys. Rev. Lett., 98:070201, Feb 2007.

[84] I. P. McCulloch. Infinite size density matrix renormalization group, revisited, 2008.

[85] G. M. Crosswhite, A. C. Doherty, and G. Vidal. Applying matrix product operators to model systems with long-range interactions. Phys. Rev. B, 78:035116, Jul 2008.

[86] F. Verstraete and J. I. Cirac. Continuous Matrix Product States for Quantum Fields. Phys. Rev. Lett., 104:190405, May 2010.

[87] S. Dutta, A. Buyskikh, A. J. Daley, and E. J. Mueller. Density Matrix Renormalization Group for Continuous Quantum Systems. Phys. Rev. Lett., 128:230401, Jun 2022.

[88] A. L. Fetter and J. D. Walecka. Quantum Theory of Many-Particle Systems. Courier Corporation, 2012.

[89] G. C. Wick. The Evaluation of the Collision Matrix. Phys. Rev., 80:268–272, Oct 1950.

[90] J. Schwinger. On the Green's Functions of Quantized Fields: I. Proc. Nat. Acad. Sci., USA, 37, 1951.

[91] P. C. Martin and J. Schwinger. Theory of Many-Particle Systems. I. Phys. Rev., 115:1342–1373, Sep 1959.

[92] L. Hedin. New Method for Calculating the One-Particle Green's Function with Application to the Electron-Gas Problem. Phys. Rev., 139:A796–A823, Aug 1965.

[93] F. Aryasetiawan and S. Biermann. Generalized Hedin's Equations for Quantum Many-Body Systems with Spin-Dependent Interactions. Phys. Rev. Lett., 100:116402, Mar 2008.

[94] F. Aryasetiawan and O. Gunnarsson. The GW method. Rep. Progr. Phys., 61(3):237, mar 1998.

[95] F. Aryasetiawan and O. Gunnarsson. Electronic structure of NiO in the GW approximation. Phys. Rev. Lett., 74:3221–3224, Apr 1995.

[96] L. Reining. The GW approximation: content, successes and limitations. WIREs Comput. Mol. Sci., 8(3):e1344, 2018.

[97] G. Strinati. Application of the Green's functions method to the study of the optical properties of semiconductors. Riv. Nuovo Cim., 11:1–86, 1988.

[98] K. Karlsson and F. Aryasetiawan. Time-dependent exchange-correlation hole and potential of the electron gas. Phys. Rev. B, 107:115172, Mar 2023.

[99] K. Balzer and M. Bonitz. Nonequilibrium Green's Functions Approach to Inhomogeneous Systems. Lecture Notes in Physics. Springer Berlin, Heidelberg, 2013.

[100] G. Stefanucci and R. van Leeuwen. Nonequilibrium Many-Body Theory of Quantum Systems: A Modern Introduction. Cambridge University Press, 2013.

[101] M. Hopjan and C. Verdozzi. Probing Strongly Correlated Materials in Non-equilibrium: Basic Concepts and Possible Future Trends in First Principle Approaches, pages 347–384. Springer Berlin Heidelberg, Berlin, Heidelberg, 2014.

[102] D. Karlsson, R. van Leeuwen, Y. Pavlyukh, E. Perfetto, and G. Stefanucci. Fast Green's Function Method for Ultrafast Electron-Boson Dynamics. Phys. Rev. Lett., 127:036402, Jul 2021.

[103] Y. Pavlyukh, E. Perfetto, Daniel Karlsson, Robert van Leeuwen, and G. Stefanucci. Time-linear scaling nonequilibrium green's function methods for real-time simulations of interacting electrons and bosons. i. formalism. Phys. Rev. B, 105:125134, Mar 2022.

[104] Y. Pavlyukh, E. Perfetto, and G. Stefanucci. Interacting electrons and bosons in the doubly screened $G\tilde{W}$ approximation: A time-linear scaling

method for first-principles simulations. Phys. Rev. B, 106:L201408, Nov 2022.

[105] M. Gopalakrishna, Y. Pavlyukh, and C. Verdozzi. Time-Resolved Optical Response of the Dicke's Model via the Nonequilibrium Green's Function Approach. Physica Status Solidi (b), page 2300576, 2024.

[106] J. Schwinger. Brownian Motion of a Quantum Oscillator. J. Math. Phys., 2(3):407–432, 05 1961.

[107] L. V. Keldysh. Diagram Technique for Nonequilibrium Processes. Sov. Phys. JETP, 20:1018, 1965.

[108] D. C. Langreth. Linear and Nonlinear Response Theory with Applications. Springer New York, NY, 2013.

[109] L.P. Kadanoff and G. Baym. Quantum Statistical Mechanics. Benjamin, New York, 1962.

[110] S. Latini, E. Perfetto, A.-M. Uimonen, R. van Leeuwen, and G. Stefanucci. Charge dynamics in molecular junctions: Nonequilibrium Green's function approach made fast. Phys. Rev. B, 89:075306, Feb 2014.

[111] P. Lipavský, V. Špička, and B. Velický. Generalized Kadanoff-Baym ansatz for deriving quantum transport equations. Phys. Rev. B, 34:6933–6942, Nov 1986.

[112] R. Tuovinen, Y. Pavlyukh, E. Perfetto, and G. Stefanucci. Time-Linear Quantum Transport Simulations with Correlated Nonequilibrium Green's Functions. Phys. Rev. Lett., 130:246301, Jun 2023.

[113] G. Stefanucci, R. van Leeuwen, and E. Perfetto. In and Out-of-Equilibrium Ab Initio Theory of Electrons and Phonons. Phys. Rev. X, 13:031026, Sep 2023.

[114] M. Ridley, N. W. Talarico, D. Karlsson, N. L. Gullo, and R. Tuovinen. A many-body approach to transport in quantum systems: from the transient regime to the stationary state. J. Phys. A, 55, 2022.

[115] W. Heisenberg. Zur Theorie des Ferromagnetismus. Z. Phys., 49:619–636, Sep 1928.

[116] T. Moriya. Spin fluctuations in itinerant electron magnetism, volume 56. Springer Berlin, Heidelberg, 2012.

[117] A. P. Ramirez. Strongly geometrically frustrated magnets. Annu. Rev. Mater. Sci., 24(1):453–480, 1994.

[118] R. Moessner and J. T. Chalker. Properties of a classical spin liquid: the heisenberg pyrochlore antiferromagnet. Phys. Rev. Lett., 80(13):2929, 1998.

[119] L. Balents. Spin liquids in frustrated magnets. Nature, 464(7286):199–208, 2010.

[120] S. V. Tyablikov. Retarded and advanced Green functions in the theory of ferromagnetism. Ukr. Mat. Zh., 11:287, 1959.

[121] J. Kondo and K. Yamaji. Green's-function formalism of the one-dimensional Heisenberg spin system. Prog. Theor. Phys., 47(3):807–818, 1972.

[122] J. Hubbard. Electron Correlations in Narrow Energy Bands. Proc. R. Soc. (London), A276:238, 1963.

[123] M. C. Gutzwiller. Effect of Correlation on the Ferromagnetism of Transition Metals. Phys. Rev. Lett., 10:159–162, Mar 1963.

[124] J. Kanamori. Electron Correlation and Ferromagnetism of Transition Metals. Progr. Theor. Phys., 30(3):275–289, 09 1963.

[125] J. des Cloizeaux and J. J. Pearson. Spin-Wave Spectrum of the Antiferromagnetic Linear Chain. Phys. Rev., 128:2131–2135, Dec 1962.

[126] P. Fazekas. Lecture Notes on Electron Correlation and Magnetism. World Scientific, 1999.

[127] J. R. Schrieffer and P. A. Wolff. Relation between the anderson and kondo hamiltonians. Phys. Rev., 149:491–492, Sep 1966.

[128] M. A. Sentef, J.-J. Li, F. Künzel, and M. Eckstein. Quantum to classical crossover of floquet engineering in correlated quantum systems. Phys. Rev. Res., 2:033033, Jul 2020.

[129] I. Dzyaloshinsky. A thermodynamic theory of "weak" ferromagnetism of antiferromagnetics. J. Phys. Chem. Solids, 4(4):241–255, 1958.

[130] T. Moriya. Anisotropic superexchange interaction and weak ferromagnetism. Phys. Rev., 120(1):91, 1960.

[131] Matthew Fishman, Steven R. White, and E. Miles Stoudenmire. The ITensor Software Library for Tensor Network Calculations. SciPost Phys. Codebases, page 4, 2022.

[132] Matthew Fishman, Steven R. White, and E. Miles Stoudenmire. Codebase release 0.3 for ITensor. SciPost Phys. Codebases, pages 4–r0.3, 2022.

[133] W. K. Wootters. Entanglement of Formation of an Arbitrary State of Two Qubits. Phys. Rev. Lett., 80:2245–2248, Mar 1998.

[134] R. Horodecki, P. Horodecki, M. Horodecki, and K. Horodecki. Quantum entanglement. Rev. Mod. Phys., 81:865–942, Jun 2009.

[135] J. Haegeman, J. I. Cirac, T. J. Osborne, I. Pižorn, H. Verschelde, and F. Verstraete. Time-Dependent Variational Principle for Quantum Lattices. Phys. Rev. Lett., 107:070601, Aug 2011.

[136] M.-R. Yang and S. R. White. Time-dependent variational principle with ancillary Krylov subspace. Phys. Rev. B, 102:094315, Sep 2020.

[137] S. Biermann, F. Aryasetiawan, and A. Georges. First-Principles Approach to the Electronic Structure of Strongly Correlated Systems: Combining the *GW* Approximation and Dynamical Mean-Field Theory. Phys. Rev. Lett., 90:086402, Feb 2003.

[138] F. Aryasetiawan and F. Nilsson. Downfolding Methods in Many-Electron Theory. AIP Publishing LLC, 2022.

[139] S. Motahari, R. Requist, and D. Jacob. Kondo physics of the Anderson impurity model by distributional exact diagonalization. Phys. Rev. B, 94:235133, Dec 2016.

[140] A. Haller, S. A. Díaz, W. Belzig, and T. L. Schmidt. Quantum magnetic skyrmion operator, 2024.

Printed by Media-Tryck, Lund 2024 NORDIC SWAN ECOLABEL 3041 0903

Faculty of Science,
Department of Physics

ISBN 978-91-8104-139-2